RIPARIAN VEGETATION IN FLUVIAL ENVIRONMENTS: LINKING TIMESCALES THROUGH VEGETATION UPROOTING

Dissertation

submitted to and approved by the

Faculty of Architecture, Civil Engineering and Environmental Sciences
University of Braunschweig – Institute of Technology

and the

Department of Civil and Environmental Engineering
University of Florence

in candidacy for the degree of a
Doktor-Ingenieur (Dr.-Ing.) /
Dottore di Ricerca in Civil and Environmental Engineering[*)]

by
Giulio Calvani
born 26/10/1984
from Empoli, Italy

Submitted on	11 February, 2019
Oral examination on	07 May, 2019
Professorial advisors	Prof. Luca Solari Prof. Hans Matthias Schöniger

2019

*) Either the German or the Italian form of the title may be used.

UNIVERSITY OF FLORENCE

Abstract

School of Engineering

Department of Civil and Environmental Engineering

Doctor of Philosophy

Riparian vegetation in fluvial environments: linking timescales through flow uprooting

by Giulio CALVANI

In the last decades, the presence of riparian vegetation on riverbanks and floodplains along rivers was acknowledged not only to improve water quality and heal biological diversity but also to contribute to river evolution processes. When water flow runs over vegetated areas, averaged velocity profile is affected by the presence of stem, branches and leaves, sediment transport changes according to modified turbulence and bed shear stresses and soil shear strength is altered by root binding. As a result, bed scour, bank erosion and accretion, bar migration and width adjustment processes lead to different river morphology evolution. Conversely, flow and sedimentary patterns influence vegetation dynamics, by shaping barebed deposits available for colonisation and by affecting mortality rate, through burying and uprooting processes.

However, whereas recruitment, establishment and growth represent the transitional dynamics from barebed to vegetated conditions and are mainly related to species properties, plant removal is intrinsically related to species growth stage, flow magnitude and soil properties. Although vegetation uprooting only recently gathered attention from scientific community, there is a rising awareness that vegetation removal is crucial for species selection and location on exposed deposits and floodplains and carbon production and sequestration, at different spatial and temporal scales.

This PhD work examines the uprooting process of both pioneer seedlings and established vegetation driven by flow and bed erosion, whose role is to reduce root anchorage, at various spatial scales ranging from a single plant to a river reach. The main purpose of this research is to illustrate the links between temporal scales regarding the hydro-morphological evolution of fluvial systems, such as bed scour development, flood duration and return period, and those proper of biological components with regards to both growth and decay rates of riparian vegetation.

For this aim, various methodologies and approaches are followed.
Firstly, an intensive analysis of the state of knowledge is presented and discussed.
Secondly, the existence of links between growth rate and hydrological return period of flood events and between decay rate and flood duration are proved and investigated by means of an already available eco-morphodynamic equation, and illustrated according to different vegetation cover. Promising results are obtained when relationships are applied to the case studies of the Maggia River (CH) and the Tagliamento River (IT).
Thirdly, the uprooting process of juvenile flexible riparian vegetation is investigated by means of flume experiments, field measurements of root resistance and numerical modelling. A new physical relationship able to predict critical conditions of bed shear stress and bed erosion is derived, validated and applied to the case study of the Ombrone Pistoiese River (IT) with good agreement.
Lastly, the proposed relationship is combined to a very recent probabilistic model and a stochastic approach to flood events. A new relationship for uprooting process randomness is proposed and the correlation between vegetation removal and flood return period is evaluated, discussed and applied to the case study of the Santa Maria River, Arizona (USA) with very good results.

The results of this PhD research show the existence of cross-related temporal scales between riparian vegetation and river morphodynamics and demonstrate their relationships with flood return period and event duration. The adapted comprehensive approach to study the uprooting process of riparian vegetation highlights that multidisciplinary methodology is essential to understand the mechanisms, correctly model the process and formulate the equations. The application to laboratory experiments and to various case studies proves the validity of the relationships as well as the applicability both to small and large spatial scales. As a final result, this research hints the capability for river to select species and cover according to hydrological regime and biological properties. This is crucial in fluvial environments altered by climate change, where alien species may replace native ones. It also underlines the importance of taking into account riparian vegetation dynamics, effects and interactions to guarantee the reliability of long-term river morphodynamics modelling and the success of river maintenance and restoration strategies.

UNIVERSITY OF FLORENCE

Zusammenfassung

School of Engineering

Department of Civil and Environmental Engineering

Doctor of Philosophy

Riparian vegetation in fluvial environments: linking timescales through flow uprooting

von Giulio CALVANI

Den, in den letzten Jahrzehnten gesammelten Erkenntnissen zu Folge, trägt das Vorkommen von Ufervegetation an Flussufern und Überschwemmungsgebieten nicht nur zur Verbesserung der Wasserqualität und Heilung der biologischen Vielfalt, sondern auch auch zu Flussentwicklungsprozessen bei. Wenn der Wasserfluss durch bewachsene Gebiete verläuft, wird das durchschnittliche Geschwindigkeitsprofil durch das Vorhandensein von Stämmen, Ästen und Blättern beeinflusst und dementsprechend der Sedimenttransport, Turbulenzen, Bettscherspannungen und Bodenscherfestigkeit, letztere durch Wurzelbindung, modifiziert. Deshalb führen Bettgeißeln, Ufererosion und Akkretion, Balkenmigration und Breitenanpassungsprozesse zu einer unterschiedlichen Flussmorphologieentwicklung.
Im Gegenzug bedingen Strömungs- und Sedimentmuster die Vegetationsdynamik, indem lockere Sedimente am Flussbett agglomeriert werden und die Neuansiedlung von Vegetation zur Folge haben. Auf der anderen Seite können diese Prozesse aber auch zum Begraben und Entwurzeln von Pflanzen führen, was in einer höheren Sterblichkeitsrate resultiert.

Während jedoch Wachstum, Festigung und Wachstum die Übergangsdynamik von unbewachsenen zu vegetierten Bedingungen darstellen und hauptsächlich mit Arteneigenschaften zusammenhängen, so korreliert die Pflanzenentfernung im trüben Gewässern mit der Wachstumsphase der Arten, der Fließgröße und der Bodeneigenschaften. Obwohl die Vegetationsentwurzelung erst vor kurzem die Aufmerksamkeit der wissenschaftlichen Gemeinschaft erregte, wächst das Bewusstsein, dass die Entfernung von Vegetation für die Artenauswahl und -lage auf exponierten Ablagerungen und Auen, sowie die Kohlenstoffproduktion und Sequestration, auf unterschiedlichen räumlichen und zeitlichen Maßstäben, von entscheidender Bedeutung sind.

Diese Doktorarbeit untersucht den Entwurzelungsprozess sowohl von Pioniersämlingen als auch von etablierter Vegetation, die durch Strömungs- und Betterosion angetrieben wird. Deren Aufgabe es ist, die Wurzelverankerung in verschiedenen räumlichen Maßstäben von einer einzigen Pflanze bis zu einer Flussreichweite zu reduzieren.

Der Hauptzweck dieser Forschung besteht darin, die Zusammenhänge zwischen zeitlichen Skalen in Bezug auf die hydromorphologische Entwicklung von Flusssystemen, wie z. B. Bettscheuerentwicklung, Hochwasserdauer und Rückgabezeit, und den eigentlichen biologischen Komponenten mit sowohl die Wachstumsraten als auch die Verfallsraten der Anrainervegetation zu ergründen.

Zu diesem Ziel werden verschiedene Methoden und Ansätze verfolgt.
Zuerst wird eine intensive Analyse des Wissensstandes vorgestellt und diskutiert.
Zweitens wird das Vorhandensein von Zusammenhängen zwischen Wachstumsrate und hydrologischer Rückkehrperiode von Hochwasserereignissen sowie zwischen Zerfallsrate und Hochwasserdauer anhand einer bereits verfügbaren ökomorphodynamischen Gleichung nachgewiesen und unterschiedliche Vegetationsdecke. Vielversprechende Ergebnisse werden erzielt, wenn Beziehungen auf die Fallstudien des Maggia River (CH) und des Tagliamento River (IT) angewendet werden.
Drittens wird der Entwurzelungsprozess der jugendlichen flexiblen Anrainervegetation mittels Flume-Experimenten, Feldmessungen des Wurzelwiderstands und numerischer Modellierung untersucht. Eine neue physikalische Theorie, die in der Lage ist, kritische Bedingungen von Bettscherstress und Betterosion vorherzusagen, wird formuliert, validiert und auf die Fallstudie des Ombrone Pistoiese River (IT) mit guter Zustimmung angewendet.
Schließlich wird den vorgeschlagenen Prozessen zu einem neuen Wahrscheinlichkeitsmodell und einem stochastischen Ansatz für Hochwasserereignisse kombiniert. Die gefundene Beziehung zur Entwurzelung von vorgeschlagene Prozesszufälligkeit und die Korrelation zwischen Vegetationsentfernung und Hochwasserrücklaufzeit wird bewertet, diskutiert und auf die Fallstudie des Santa Maria River, Arizona (USA) mit sehr gutem Ergebnis angewendet.

Diese Doktorarbeit zeigt die Existenz von querverwandten zeitlichen Skalen zwischen Ufervegetation und Flussmorphodynamik und erklärt deren Beziehungen zur Hochwasserrücklaufzeit und Ereignisdauer. Der angepasste umfassende Ansatz zur Untersuchung des Entwurzelungsprozesses der Anrainervegetation zeigt, dass multidisziplinäre Methoden unerlässlich sind, um die Mechanismen zu verstehen, den Prozess richtig zu modellieren und die Gleichungen zu formulieren. Die Anwendung auf Laborexperimente und verschiedene Fallstudien belegt die Gültigkeit der Zusammenhänge sowie die Anwendbarkeit sowohl auf kleine als auch auf große räumliche Maßstäbe. Als Endergebnis deutet diese Forschung auf die Fähigkeit des Flusses hin, Arten auszuwählen und nach hydrologischem Regime und biologischen Eigenschaften abzudecken. Dies ist von entscheidender Bedeutung in flussverändernden Umgebungen, die durch den Klimawandel verändert werden, wo gebietsfremde Arten einheimische Arten ersetzen können. Dieser unterstreicht auch, wie wichtig es ist, die Dynamik, die Auswirkungen und Wechselwirkungen der Ufervegetation zu berücksichtigen, um die Zuverlässigkeit der langfristigen Flussmorphodynamikmodellierung und den Erfolg von Flusserhaltungs- und -restaurationsstrategien zu gewährleisten.

Contents

List of Figures

List of Tables

List of Symbols

$\overline{a}$	average stem area per unit volume	m^{-1}
a_{ST}	parameter for type of sediment transport	[-]
b	exponent in sediment transport formula	[-]
$b_{0,i}$	coefficient related to the i-th plant family	[-]
$b_{1,i}$	exponent coefficient related to the i-th plant family	[-]
c'	soil cohesion	Pa
c_a	reference concentration of suspended sediment	[-]
c_i	i-th coefficient in polynomial equation of variable X	$[X]^{-i}$
f	soil-wood friction coefficient	[-]
g	acceleration due to gravity	$\mathrm{m\,s}^{-2}$
g_t	erosion process noise	$\mathrm{m}^3\,\mathrm{s}^{-1}$
j	dummy variable	[-]
k	coefficient for dimensionless sediment transport q_s	[-]
k_g	coefficient for sediment layer thickness	[-]
l_m	Prandtl mixing length	m
l_s	sediment mixing length	m
m	number of shot events	[-]
n	Manning coefficient for bed roughness	$\mathrm{s\,m}^{-1/3}$
${}_pF_q[\,\cdot\,;\,\cdot\,;\,\cdot\,]$	generalised hypergeometric function	[-]
$p_\tau(t)$	probability distribution function of time at uprooting	d^{-1}
$p(q)$	probability distribution function of flow discharge q	$\mathrm{s\,m}^{-3}$
q	flow discharge	$\mathrm{m}^3\,\mathrm{s}^{-1}$
q_s	dimensionless sediment transport per unit width	[-]
q_{SL}	suspended load per unit width	$\mathrm{m}^3\,\mathrm{s}^{-1}$
t	time	s
t_d	decay duration	d
t_g	growth duration	d
t_l	leaf thickness	m
u	longitudinal velocity	$\mathrm{m\,s}^{-1}$
u_*	shear velocity	$\mathrm{m\,s}^{-1}$
u_w	pore water pressure	Pa
x	longitudinal coordinate	m
y	vertical coordinate	m
w	dummy variable for integration	[-]

z	transversal coordinate	m
A_f	frontal area of plant	m^2
A'_f	frontal area of plant after reconfiguration	m^2
A_i	catchment area of i-th sub-basin	m^2
A_l	foliage area	m^2
A_{tot}	total catchment area	m^2
A_{vr}	length scale in Van Rijn's model for suspended load	m
B	river width	m
B_f	river width at the vegetation front	m
C_D	drag coefficient for vegetation	[-]
C_i	surface cover of i-th species	[-]
C_u	sediment coefficient of uniformity	[-]
D_i	i-th quantile in grain size distribution	m
$D_{m,i}$	stem diameter of the i-th species at maturity age	m
D_p	stem diameter	m
D_r	mean root diameter	m
$D_{r,i}$	diameter of i-th root	m
D_G	adjusted D_{50}	m
F_r	Froude number	[-]
F_B	buoyancy force	N
F_D	destabilising force	N
F_R	root resisting force	N
F_R^b	root resisting force against breakage	N
F_R^I	root resisting force for Type I uprooting	N
F_R^s	root resisting force against sliding	N
G	time integral of bed erosion randomness g_t	m^3
H_p	stem height	m
H'_p	stem height after reconfiguration	m
I_1	first Einstein's integral function	[-]
I_2	second Einstein's integral function	[-]
$I(q, D_{50})$	integral function for suspended load	[-]
$\dot{L}_d$	deterministic exposing rate of root	$m\,s^{-1}$
L_e	critical erosion for Type II uprooting	m
L_r	mean root length	m
$L_{r,i}$	length of i-th root	m
LAI	Leaf Area Index	[-]
N_R	number of resisting roots	[-]
N_T	total number of roots	[-]
P_ξ^+	above-threshold probability	[-]
P_ξ^-	below-threshold probability	[-]
P_τ	uprooting probability	[-]
P_ξ	Peak Over Threshold probability	[-]

Q	steady state flow discharge	$m^3\,s^{-1}$
$Q_0(\xi)$	initial peak value in reference mean event	$m^3\,s^{-1}$
$Q_\xi(t)$	reference mean event	$m^3\,s^{-1}$
Q_{cr}	critical flow discharge for incipient erosion	$m^3\,s^{-1}$
Q_d	reference flow discharge	$m^3\,s^{-1}$
Q_i	flow discharge for the i-th catchment basin	$m^3\,s^{-1}$
$\overline{Q}_{q>\xi}$	average flow discharge above threshold ξ	$m^3\,s^{-1}$
Q_s	sediment transport	$m^3\,s^{-1}$
Q_{tot}	flow discharge for the total catchment basin	$m^3\,s^{-1}$
R^2	determination coefficient	[-]
R_e	Reynolds number	[-]
R_{ep}	particle Reynolds number	[-]
R_i	hydraulic radius	m
S	bed slope	[-]
$\hat{T}_\xi$	total duration of reference mean event $Q_\xi(t)$	d
$\tilde{T}$	dimensionless time at uprooting	[-]
$T(\xi)$	return period	year
T_ξ^+	mean time above threshold ξ	d
$T_{\xi\to Q_{cr}}^+$	mean time from threshold ξ to Q_{cr}	d
T_ξ^-	mean time below threshold ξ	d
$T_{m,i}$	maturity age of i-th species	y
U	cross-section averaged flow velocity	$m\,s^{-1}$
U_v	mean flow velocity in the vegetated layer	$m\,s^{-1}$
V	time integral of bed erosion rate $\dot{\eta}$	m
W	error function in $p(\tau)$	[??]
$W_a[\,\cdot\,]$	a-limb Lambert function	[-]
Y	water depth	m
Y_{cr}	water depth for incipient motion of sediment	m
Z	Rouse number for suspended sediment	[-]
α_{BL}	coefficient in bedload transport formula	[-]
α_d	specific decay rate of vegetation	$h\,km^{-3}$
$\overline{\alpha}_d$	average decay rate of vegetation	$h\,km^{-3}$
α_g	specific growth rate of vegetation	$cm^2\,y^{-1}$
$\overline{\alpha}_g$	average growth rate of vegetation	$cm^2\,y^{-1}$
α_{SL}	coefficient in suspended load transport formula	[-]
β	ratio between decay α_d and growth α_g rates	$s^2\,m^{-3}$
β_P	parameter in the Compound Poisson Process	[-]
γ_P	average jump height in q Poisson process	$m^3\,s^{-1}$
γ_{sat}	saturated soil unit weight	$N\,m^{-3}$
γ_v	vegetation unit weight	$N\,m^{-3}$
γ_w	water unit weight	$N\,m^{-3}$
δ_a	reference level for suspended load	m

δ_e	thickness of *exchange layer*	m
ϵ	absolute roughness of the channel bed	m
λ_P	mean interval between pulses in Poisson process	d
λ'_P	adjusted mean interval between above-threshold pulses in Poisson process	d
λ_s	sediment porosity	[-]
$\zeta(t)$	white shot noise in flow discharge dynamics	$\mathrm{m^3\,s^{-1}}$
η	bed elevation	m
$\overline{\eta}$	mean bed elevation	m
$\dot{\eta}$	bed erosion rate	$\mathrm{m\,s^{-1}}$
$\dot{\eta}_d$	deterministic erosion rate	$\mathrm{m\,s^{-1}}$
μ_P	average flow discharge in Poisson process	$\mathrm{m^3\,s^{-1}}$
ν_t	eddy viscosity	$\mathrm{m^2\,s^{-1}}$
ξ	threshold flow discharge	$\mathrm{m^3\,s^{-1}}$
ρ	water density	$\mathrm{kg\,m^{-3}}$
ρ_s	sediment density	$\mathrm{kg\,m^{-3}}$
$\tilde{\sigma}^2$	dimensionless time-at-uprooting process variance	[-]
σ^2	time-at-uprooting process variance	$\mathrm{m^2\,s^{-1}}$
σ_r	root tensile strength	Pa
σ_{soil}	soil normal stress	Pa
τ	dummy time variable for integration	d
τ_1	adjusted τ_P for the first part of the reference mean event	d
τ_2	adjusted τ_P for the second part of the reference mean event	d
τ_{bed}	bed shear stress	Pa
τ^*	Shields parameter	[-]
τ^*_{cr}	critical Shields parameter	[-]
τ^*_{SL}	critical Shields parameter for suspended load	[-]
τ^I_{bed}	critical bed shear stress for Type I uprooting	Pa
τ_P	integral temporal scale in Poisson process	d
τ_{soil}	soil shear strength	Pa
τ_v	shear stress due to vegetation drag	Pa
ϕ	ratio between threshold ξ and mean jump height γ_P	[-]
ϕ'	soil shear strength angle	rad
ϕ_{cr}	ratio between critical flow discharge Q_{cr} and mean jump height γ_P	[-]
ϕ_m	maximum carrying capacity	
ϕ_v	vegetation density	
ψ_1	coefficient for bed erosion	$\mathrm{m}^{\frac{5-18b}{10}}\ \mathrm{d}^{\frac{3b-5}{5}}$
ψ_2	coefficient for bed erosion	$\mathrm{m}^{\frac{1}{2}}\left(\mathrm{m}^{-\frac{9}{10}}\mathrm{d}^{\frac{3}{10}}\right)^{a_{ST}}$

$\Gamma[\,\cdot\,]$	complete Gamma function	[-]
$\Gamma[\,\cdot\,,\,\cdot\,]$	upper incomplete Gamma function	[-]
Δ_a	dimensionless reference level for suspended load	[-]
Δs	average space between plants	m
Δx	longitudinal length scale	m

List of Abbreviations

CPP	**C**ompound **P**oisson **P**rocess
i.i.d.	**i**ndependent and **i**dentically **d**istributed
PDF	**P**robability **D**ensity **F**unction
POT	**P**eak **O**ver **T**hreshold

Chapter 1

Introduction

FIGURE 1.1: Downstream view of the Snake River near the Oxbow bend, Wyoming (USA), showing juvenile riparian vegetation near the main channel (source: https://en.wikipedia.org/wiki/Snake_River).

This chapter explains background, aims and methods of the Doctoral thesis and highlights the structure of the whole manuscript.

1.1 Background

The water channel and the surrounding areas form a compact environment within which the aquatic and the terrestrial elements mutually interact at different spatial and temporal scales (Naiman et al., 2010). In this scene, the part of a fundamental character is acted by the established vegetation, both inside the main channel by the aquatic species and in the emerged areas by the terrestrial ones. As in a well organised orchestra, different plant species find their own position along the cross section according to their above- and below- ground properties and the directives given by the hydrological regime. Indeed, fluvial species adjusted their life strategy to frequency and magnitude of flow events (Karrenberg et al., 2002). More specifically, aquatic species adapted to endless inundated environment, under either fully or partially submerged conditions, thus becoming more sensible to water quality conditions and low water depth (Gurnell, 2014). Conversely, terrestrial species adapted to live in a more complex and drier environment (Mahoney and Rood, 1998), stressed and inundated by flow only during periodical high stage events (Mitsch and Gosselink, 2000; Camporeale et al., 2013). This part of the riverine habitat, namely *riparian zone*, mostly adjacent to the main water channel, is described as *"that part of the biosphere supported by, and including, recent fluvial landforms and inundated or saturated by the bankfull discharge"* (Hupp and Osterkamp, 1996).

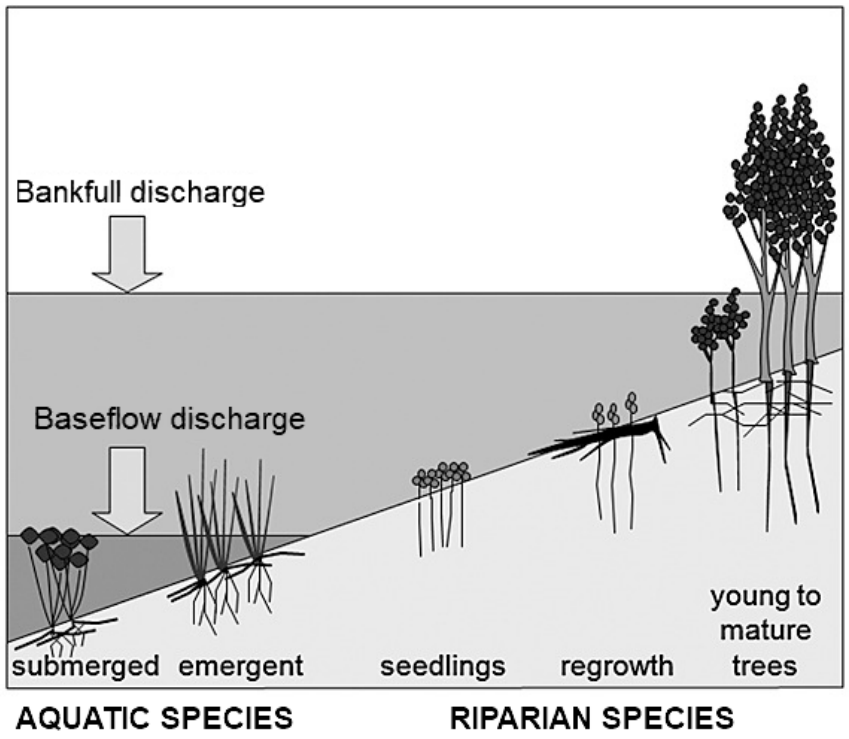

FIGURE 1.2: Sketch of a river cross section. Growth stage and position of aquatic and riparian plants are defined in agreement with their ability to adapt to different flow conditions (modified from Gurnell (2014)).

The water fluxes on the riparian zones are responsible for the longitudinal,

lateral and even vertical hydrological connectivity of the river (Ward et al., 2002). Moreover, they support the connection between channel and floodplain needed for the reproduction of plants and organisms (e.g., Mahoney and Rood, 1998; Carter Johnson, 2000) and influence soil material processes (e.g., Edwards et al., 1999). At the same time, riparian vegetation controls water quality by biological filtering (e.g., Schnauder and Moggridge, 2009), affects flow field and sediment transport by damping turbulence near the bed (e.g., De Langre et al., 2012) and inducing vortices at a lower depth (e.g., Nezu and Sanjou, 2008; Luhar and Nepf, 2011; Okamoto and Nezu, 2009). Additionally, riparian species increase soil strength against erosion trough the action of roots (e.g., Thorne, 1990; Pasquale et al., 2011). As a result, such interactions and feedbacks between river processes and riparian vegetation are the key points to understand the state and the evolution of riverine habitats (Corenblit et al., 2007). Particularly, a key aspect in these interactions is represented by the flow-induced uprooting process of juvenile vegetation, which constitutes the pioneer growth stage leading to more mature and established plants.

Assessing the long-term evolution of river channels is related to both natural (e.g., alterations of magnitude and frequency of flood events and colonisation of invasive alien species due to climate change) and human interventions (e.g., water withdrawals, damming and sediment dredging). Even river restoration projects induces changes in the morphological and biomass patterns (Montgomery, 1997; Wohl et al., 2015). The improved knowledge of the spatio-temporal scales at which vegetation and rivers interact is a key aspect to design successful solutions of river restoration (Montgomery, 1997; Wohl et al., 2015). It further improves the capability of numerical models and their reliability in carrying out long-term simulations (Vargas Luna, 2016).

1.2 Objectives

The knowledge of spatio-temporal scales at which vegetation interacts with fluvial processes is crucial to predict the long-term morphodynamic evolution of rivers and successfully design river restoration projects. With specific focus on the process of vegetation removal by flow and bed erosion, the objectives of this research are:

- Identification of species-dependent relations linking fluvial to biological processes both in terms of growth and decay rates.
- Development of a model able to predict the conditions of flow and bed erosion for which plants are likely to be uprooted in riverine environments.
- Prediction of the long-term dynamics of riparian vegetation with particular regard to the resilience to flood events.

1.3 Research questions

Concerning the presence of vegetation in fluvial environments and its role in the riparian zone, the research questions are:

- **What are the growth and mortality timescales of riparian vegetation when dynamics is altered by flood events?**

Plant species sprout, recruit and grow on the riparian zone according to biological parameters and species characteristics, but the growth and mortality due to flow uprooting are periodically influenced by flood events driven by hydrological timescales. Linking the two processes is necessary to better understand the interactions at the reach scale and to improve the knowledge of the whole system dynamics.

- **What are the most important factors affecting vegetation mortality due to flow uprooting?**

Flow uprooting is a complex process and its occurrence depends on both above- and below- ground plant size, flow velocity, sediment properties and stochastic components in the interactions amongst them all. Understanding the key factors in the removal process is necessary to develop a reliable model able to predict conditions for which plant uprooting occurs.

- **What is the role of huge flood events (e.g., with return period higher than decades) on the dynamics of riparian vegetation?**

Under climate scenarios, high magnitude flood events, associated to low frequency and high return period, are more likely to occur. Despite the innate interest in risk management and flood defence solutions, their effects on river morphodynamics were seldom investigated. However, the comprehension of the alteration induced on floodplains, riparian habitats and local species is a key aspect to design river restoration projects and maintenance strategies of fluvial ecosystems.

1.4 Methodology

The work is carried out by combining analytical approach, experimental setups, field measurements and observations and numerical simulations. The combination of all the different approaches and methods is essential for the successful completion of the work.

Literature review is carried out at the beginning of the work to analyse the state of knowledge about riparian vegetation and its effects on river morphodynamics. Mutual interactions between vegetation and fluvial processes and their modelling are examined as well. Consequently, literature review allows identifying the key processes driving vegetation removal in rivers. It determines the spatial scales and selects the most appropriate methods to investigate such processes. As a result, it paves the way to develop the model for the uprooting of juvenile flexible vegetation.

The analytical approach is fundamental to formulate the problem, to understand the role of the main factors, to include stochastic terms in the equations and to derive relatively simple relationships for their solution.

Laboratory experiments under controlled conditions are key to explore different setups and collect data of several variables and parameters in a reasonable amount of time. In this work, flume experiments are used to test the developed model for vegetation uprooting.

Field measurements and observations provide the links between laboratory setups and real cases of uprooting. Data collection from previous studies on vegetation in rivers is crucial to link biomorphological temporal scales at the reach scale. However, data of documented uprooting events in rivers are lacking. Proving the correspondence between modelled and measured values of flow uprooting after a flood event is a key point to validate the model and upscale its validity.

Numerical simulations provide the tools to replicate past events and to forecast system evolution at spatial and temporal scales impossible to reproduce in laboratory experiments. The BASEMENT tool (http://www.basement.ethz.ch) is one of the most appropriate for the aims of this research.

1.5 Structure of the thesis

The thesis is organised in six main chapters.

Chapter 1 introduces the problem, lists the research questions and objectives and briefly describes the methodology of the work.

Chapter 2 includes a literature review about effects of vegetation on river hydraulics and morphodynamics, their interactions and modelling at different spatial and temporal scales. Specific attention is paid to the process of vegetation removal driven by flow and bed erosion (*uprooting*) and the properties of root systems.

Chapter 3 discusses the problem of interactions between vegetation and rivers with converging banks, leading to the formation of a vegetation front inside the channel.

Chapter 4 describes the proposed conceptual model and equations to predict the critical conditions of flow and bed erosion leading to plant uprooting. Laboratory setups, field measurements and numerical simulations are described. Chapter 4 includes the results of the analysis, as well.

Chapter 5 introduces a stochastic approach to flow uprooting and combine the proposed equations with a probabilistic model. An extreme value analysis of flow discharges is performed to link the uprooting probability to flow return period.

Lastly, Chapter 6 summarises the main findings of the work and proposes outlooks and recommendations for future studies. Suggestions for long-term numerical modelling and for river restoration projects are proposed as well.

Chapter 2

Vegetation in riverine environments: current state of knowledge

FIGURE 2.1: Juvenile riparian vegetation on a gravel bar in the Tagliamento River. Photo taken near San Daniele del Friuli (IT).

This chapter describes the key points of interactions between vegetation and river morphodynamics and examines the current state of knowledge.

2.1 Outline

Riparian vegetation influences river evolution at different spatial and temporal scales, according to its growth stage, age, foliage area and root architecture and resistance. Particularly, vegetation may increase drag and reduces velocity and, consequently, promotes water depth increasing and sediment transport dumping. Even below-ground biomass (i.e., root system) contributes to reduce sediment transport by binding soil particles and to increase threshold for sediment motion. As a result, all the factors governing river morphodynamic evolution are altered.

In this chapter, the state-of-the-art about interactions between vegetation and hydro-morphology of riverine environments is examined. Firstly, average velocity profile (section 2.2) and associated roughness modelling in vegetated channels (section 2.3) are illustrated. Secondly, sediment transport under presence of vegetation (section 2.4) and root architectures (section 2.5) are presented. Then, the recent discoveries on vegetation uprooting are introduced (section 2.6). Lastly, a general excursion on modelling river morphodynamics and the presence of vegetation is shown (section 2.7).

2.2 Average velocity profile in vegetated channels

The most commonly acknowledged effect of vegetation on hydraulics is the alteration of mean velocity profile and the reduction of flow velocity near the bed, leadinig to a reduction of the bed shear stresses and, accordingly, of the sediment transport rate (Tsujimoto, 1999; Bennett et al., 2008). Changes in flow velocity occur across several spatial scales, ranging from individual branches and blades on a single plant to a community of plants in a meadow or patch (Nepf, 2012b). In literature, effects of vegetation on flow velocities are modelled according to the ratio between water depth, Y, and plant height, H_p, namely the degree of submergence, the spatially averaged density of plants, ϕ_v, and their flexibility.

When plants are emerging (i.e., $Y/H_p < 1$), the time-averaged velocity profile along the vertical coordinate y is independent of the degree of submergence and, for a given spatial density of plants ϕ_v, it becomes mainly related to their flexibility (Baptist et al., 2007; Nepf, 2012b). Aberle and Järvelä (2013) further suggested that velocity profile can change according to the vertical distribution of foliage. The average velocity is generally assumed constant along the vertical coordinate, with the largest variations confined near the channel bed (figure 2.2-a)), if vegetation is rigid (Choi and Kang, 2004; Kubrak et al., 2008, among others). Stoesser et al. (2010) highlighted the presence of small variation from the uniform velocity profile, when flexibility of plants is not negligible (figure 2.2-b)).

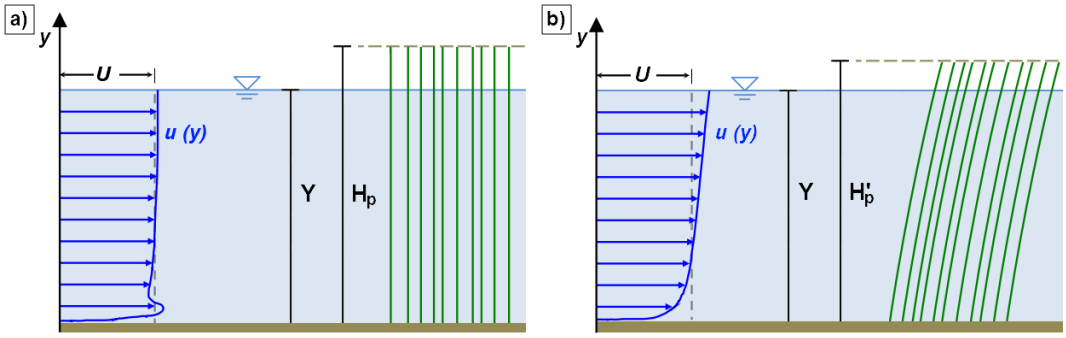

FIGURE 2.2: Time-averaged velocity profile in case of emergent vegetation (both the stem height H_p and the stem height after reconfiguration H'_p are higher than the flow depth Y). a) Almost uniform profile for rigid vegetation: maximum velocity near the bed depends on the position of first branches on the plants; b) Nearly logarithmic profile for flexible vegetation (adapted from: Vargas Luna (2016)).

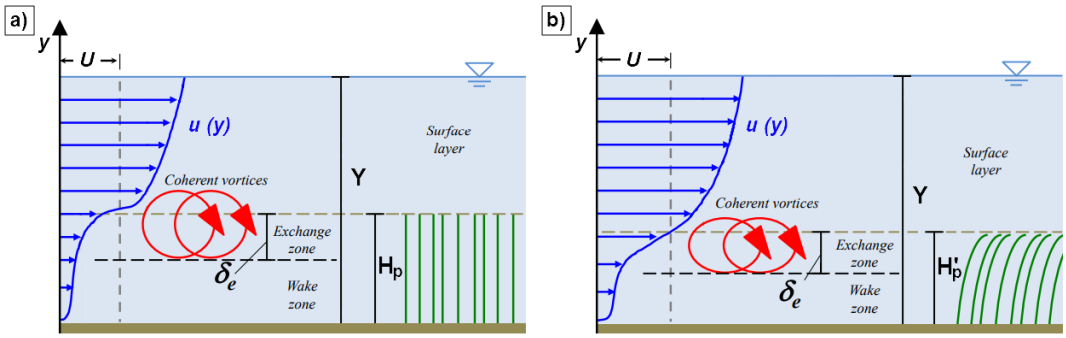

FIGURE 2.3: Time-averaged velocity profile in case of submerged vegetation. δ_e is the thickness of the *upper vegetation zone*. a) Rigid vegetation; b) Flexible vegetation (adapted from: Vargas Luna (2016)).

On the contrary, in case of submerged vegetation (i.e., $Y/H_p > 1$), the flow profile becomes more complex. Due to this complexity, flow velocity is generally studied by dividing the water depth in three different layers: the lower vegetation region (*wake zone*), the upper vegetation region near the interface at the top of plants (*exchange zone*) and the non-vegetated region (*surface layer*) (Ghisalberti and Nepf, 2006). In the surface layer, the flow profile follows a turbulent boundary-layer profile (Nepf, 2012b; Vargas Luna, 2016). The exchange zone is an intensively active region in terms of turbulence production and presence of coherent structures. The thickness of exchange layer, δ_e, depends mainly on spatial density and flexibility of vegetation (Ghisalberti and Nepf, 2006; Nepf, 2012b). The flow profile here presents an inflection point, as testifying the intense activity of Reynolds stresses, for $\phi_v D_p H_p \geq 0.1$ (with D_p the stem diameter). Conversely, the wake zone is characterised by low flow velocity. As a consequence, turbulence is damped and reduced to small-scale (i.e., stem) vortices leading to almost negligible Reynolds shear stresses (Hu et al., 2013). These considerations are valid in the case of both rigid and flexible vegetation (figure 2.3). However, in case of flexible plants, the interactions between flow and waving plants promote the formation of additional vortices (Okamoto and Nezu, 2009). When flexibility is low, these vortices are larger than the original coherent structures in the exchange zone but cannot penetrate deeper in the wave region.

On the contrary, for highly flexible plants or under high flow rates, additional vortices are smaller but can penetrate the wave region, thus increasing the flow velocity (Nezu and Sanjou, 2008; Luhar and Nepf, 2011) and momentum absorption near the bed surface (De Langre et al., 2012).

2.3 Roughness modelling in vegetated channels

Well-known relations to estimate hydraulic roughness in open channels (e.g., Manning, Chézy) take into account bed material, presence of bed-forms (such as ripples, pools, dunes and bars), regular shape of cross sections along the river, channel sinuosity and the presence and type of vegetation (Arcement and Schneider, 1989). However, when present, in-channel and riparian vegetation on the floodplains represents the most important factor in affecting flow roughness.

To explicitly account for roughness induced by the presence of vegetation, Schlichting (1937) proposed to split the total shear stress into bed shear stress, τ_{bed}, mainly related to bed material, and vegetation drag, τ_v. The total momentum balance reads:

$$\rho\, g\, R_i\, S = \tau_{bed} + \tau_v \tag{2.1}$$

where ρ is the water density; g is the acceleration due to gravity; R_i is the hydraulic radius; S is the bed slope. Whereas the bed shear stress τ_{bed} governs the motion of sediment, the vegetation drag τ_v is responsible for momentum absorption (section 2.2), according to the drag force approach (Eq. (2.2)) (Hygelund and Manga, 2003).

$$\tau_v = \frac{1}{2}\rho\, C_D\, \overline{a}\, H_p\, U_v^2 \tag{2.2}$$

Therein, C_D is the drag coefficient; $\overline{a} = \phi_v D_p$ is the average stem area per unit volume; H_p' is the stem height after reconfiguration, eventually equal to H_p in case of rigid vegetation; U_v is the mean flow velocity in the vegetated layer. The fraction of total shear stress allocated to each of the right-hand side terms in Eq. (2.1) depends on flow conditions and vegetation properties. For instance, Shimizu (1994) found that an increasing vegetation density leads to an increasing total shear stress and, on the contrary, a decreasing bed shear stress. This suggests that bed shear stress in vegetated channels represents only a small amount of total shear stress, and, therefore, vegetation drag contributes most to flow resistance. Eventually, bed shear stress can be neglected for high vegetation density (Fathi-Maghadam and Kouwen, 1997).

Although the approach is widely accepted in the scientific community, the use of global flow roughness estimators still remains a valid approach, even in numerical modelling (e.g., Bertoldi et al., 2014; Bywater-Reyes et al., 2015; Caponi and Siviglia, 2018). However, when more refined calculations are required (for instance, in long-term morphodynamic simulations), a more precise modelling of vegetation

is necessary. In this case, roughness estimators should take into account specific properties and characteristics of plants (Vargas-Luna et al., 2016).

Vegetation in open channels is characterised by species, growth stages and size and its properties vary in time according to season and environmental conditions. Additionally, it can be either flexible (grasses and shrubs) or rigid (woody species), and either emergent or submerged with respect to the water depth (Wu and He, 2009). Moreover, each plant has an almost unique combination of height, stem diameter and stiffness, foliage density, roots architecture and other properties (Vargas-Luna et al., 2015; Vargas-Luna et al., 2016). Nevertheless, plants properties (i.e., spatial density, foliage area, height and diameter, etc.) are generally assumed constant in time and space (Nepf and Vivoni, 2000; Ghisalberti and Nepf, 2002; Nepf and Ghisalberti, 2008; Nepf, 2012a). In addition, it is widely accepted to represent plants as a collection of uniform and uniformly distributed rigid cylinders (Dijkstra and Uittenbogaard, 2010; Vargas-Luna et al., 2016) (figure 2.4). Under this simplifying hypothesis, roughness in vegetated channels is generally described by empirical equations or physics-based models (Galema, 2009).

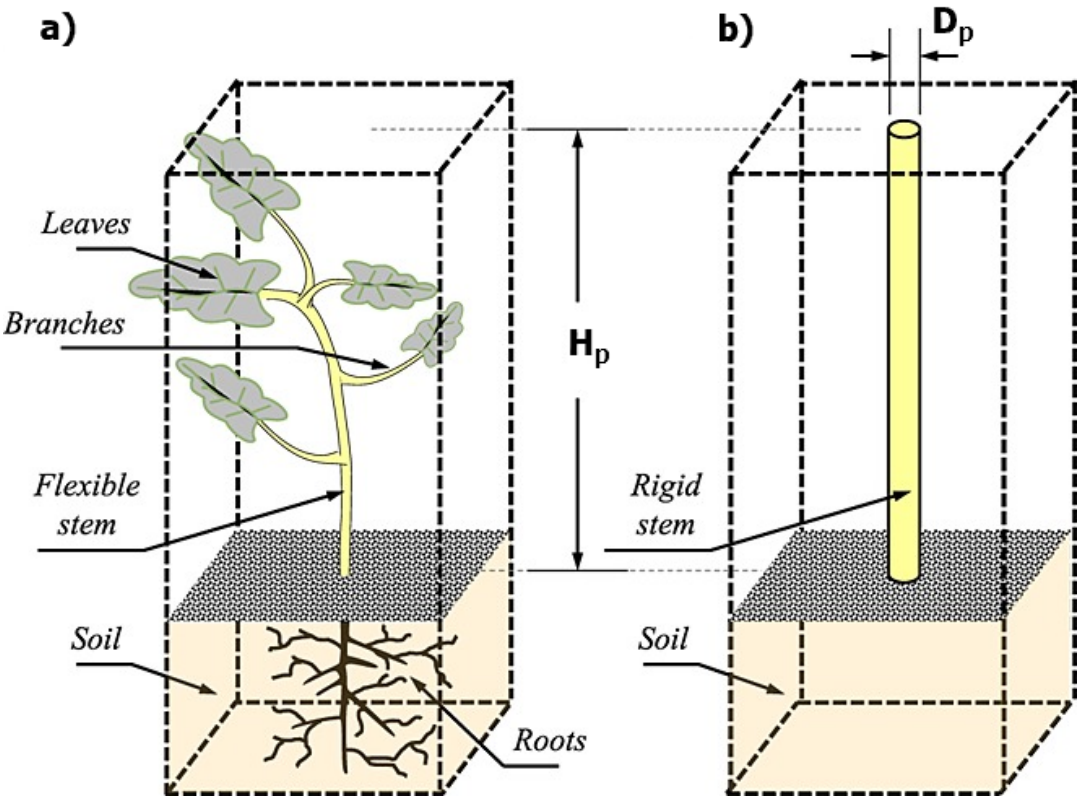

FIGURE 2.4: Scheme of riparian vegetation. a) real plant; b) rigid-cylinder analogy (modified from Vargas-Luna et al. (2016)).

To account properly for the presence of vegetation and its effects on flow velocity, many alternative relations were proposed, generally referring to different degree of submergence (i.e., emergent vs. submerged) and the stiffness of plant stem (i.e., rigid vs. flexible). For rigid vegetation, most of the relations present in literature

are based on the rigid cylinder analogy. Some of them can be used only in emergent conditions (Petryk and Bosmajian III, 1975; Ishikawa et al., 2003; Kothyari et al., 2009), some others only in submerged conditions (Klopstra et al., 1996; Huthoff et al., 2007; Yang and Choi, 2010), whereas methods of Barfield et al. (1979), Stone and Shen (2002) and Baptist et al. (2007) can be used in both conditions. Conversely, for real flexible vegetation, the rigid cylinder analogy becomes very weak. Due to the presence of leaves and under the action exerted by flow, flexible plants modify their shape, frontal area and size, a process called *reconfiguration* (Vogel, 1996). Reconfiguration occurs until balance between the drag force and the restoring force due to body stiffness is achieved.

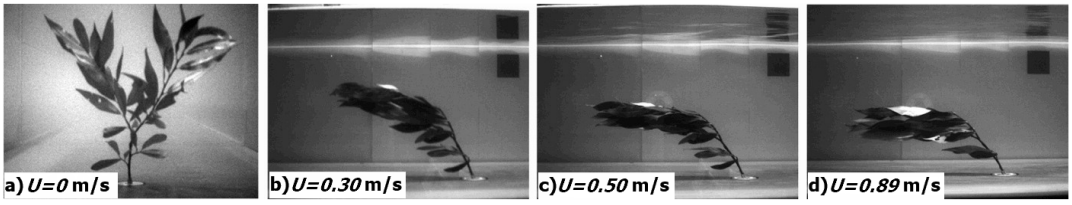

FIGURE 2.5: Plant reconfiguration process induced by different flow velocities in flume experiments (flow is from right to left) on a submerged willow. a) initial configuration $A'_f = A_f$; b) $U = 0.30\,\mathrm{m\,s^{-1}}$, $A'_f = 0.38\ A_f$; c) $U = 0.50\,\mathrm{m\,s^{-1}}$, $A'_f = 0.23\ A_f$; d) $U = 0.89\,\mathrm{m\,s^{-1}}$, $A'_f = 0.18\ A_f$; (modified from Aberle and Järvelä (2013)).

With respect to the flow velocity, reconfiguration can produce different equilibrium configurations in very flexible species (e.g., herbaceous plants) (figure 2.5), ranging from a roughly vertical for very low flow discharge, to moderately bended, for intermediate velocities, to even completely prone position for higher values (Dijkstra and Uittenbogaard, 2010; De Langre et al., 2012). Alteration in flow roughness follows accordingly. To give an example, by means of laboratory experiments with grass, Morgan and Rickson (2003) found out that Manning's coefficient reduced more than an order of magnitude when vegetation was prone. Due to uncertainty in characterising plant properties and reconfiguration, many more relations for flow roughness of flexible vegetation under emergent or submerged conditions were developed (e.g., Kouwen, 1992; Freeman et al., 2000; Järvelä, 2004; Aberle and Järvelä, 2013; Västilä et al., 2013). Among such relations, Vargas-Luna et al. (2015) demonstrated that the model proposed by Baptist et al. (2007) reasonably reproduces the flow roughness of flexible vegetation, provided that the reconfigured height of the plant, H'_p, is accounted for.

2.4 Sediment transport in vegetated channel

The influence of vegetation on both suspended and bedload sediment transport was typically investigated by means of laboratory observations (Solari et al., 2016). It is generally acknowledged that the presence of vegetation locally decreases sediment transport and enhances deposition, due to flow velocity reduction and turbulence

damping. Nevertheless, few studies showed that vegetation may promote erosion, at the spatial scale of the vegetated patch, according to channel morphology (e.g., Dittrich et al., 2005; Rominger et al., 2010), shape and density of plants (Bennett et al., 2002; Bennett et al., 2008) and stem arrangement (e.g., parallel vs. staggered pattern) (Li and Shen, 1973). The local pattern of erosion/deposition near a circular patch of vegetation was investigated by Follett and Nepf (2012) by means of flume experiments with rigid emergent cylinders (figure 2.6). They found that the region behind the patch is influenced by the presence of the patch itself and has a finite length, depending on the stem diameter and plant density (Zong and Nepf, 2012). For such length they also proposed an empirical formulation.

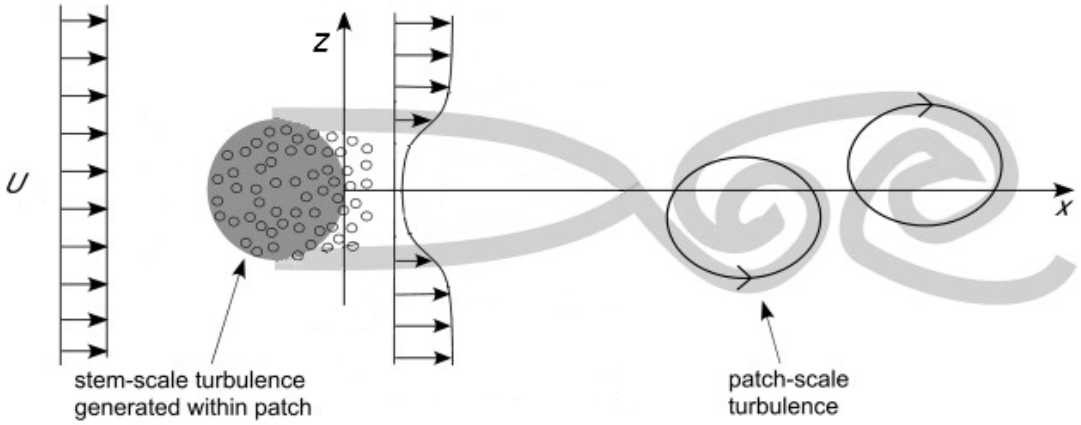

FIGURE 2.6: Pla view of the flow pattern and wake behind a circular patch of emergent rigid cylinders (modified from Follett and Nepf (2012)). Flow is from left to right.

Currently available sediment transport models incorporating the effect of vegetation are quite scarse and can be applied only under the particular conditions which they were developed or adapted for (e.g., Ishikawa et al., 2003; Jordanova and James, 2003; Kothyari et al., 2009; Armanini et al., 2015). Indeed, their use outside the range of validity yields to either different or even opposite results. For instance, Watanabe et al. (2002) showed that the critical shear stress for incipient motion of sediment (depending on vegetation density and stem-to-sediment ratio) is higher than that in bare bed condition, whereas Hongwu et al. (2013) discovered that in some situations sediments start moving at a lower critical flow velocity, due to the presence of secondary flows within, horse-shoe vortices around and wake vortices downstream the vegetated patch, inducing sediment motion, in agreement with observations of Dargahi (1990).

However, the estimation of sediment transport in vegetated channels is generally based on a simplified approach. Standard bedload and suspended load relations are involved and their validity is extended by accounting for the proper bed shear stress and drag coefficient C_D of the vegetation (Eqs (2.1) and (2.2)) (Okabe et al., 1997; Jordanova and James, 2003; Kothyari et al., 2009). Following this approach, Specht (2002) derived a reductive coefficient to take into account the effects

of vegetation in bedload transport formulations. Similarly, such considerations can be extended to suspended load (Sharpe and James, 2006; Zong and Nepf, 2010).

2.5 Root architecture

Below-ground biomass is a complex structure responsible in vegetation for the uptake of nutrients and water from soil (e.g., Fitter, 1987; Dupuy et al., 2005) and for providing stability to the above-ground plant (e.g., Wu et al., 1988; Stokes et al., 1996; Reubens et al., 2007). Plants roots bind soil particle, thus increasing soil resistance to erosion (Gray and Sotir, 1996). Additionally, roots can add tension resistance to the soil material which is typically strong only in compression. As a result, the presence of roots into the soil produces a reinforced matrix, through a complex 3-D mechanism acting at the soil–root interface (Fan and Chen, 2010), similarly to steel or fiberglass in concrete structures (Coppin and Richards, 1990; Thorne, 1990).

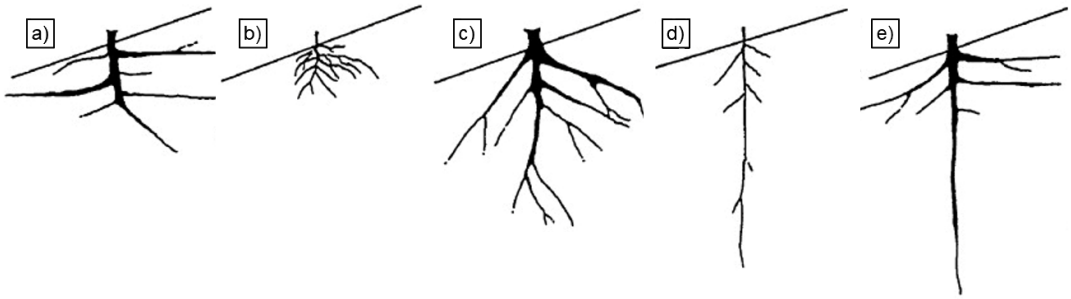

FIGURE 2.7: Plant root system classification by Yen (1987). a) H-type; b) M-type; c) R-type; d) V-type; e) VH-type (modified from Fan and Chen (2010)).

The increase in soil shear strength and the extent of soil reinforcement depend on how stresses are transferred at the root-soil interface. In this regard, the shape and branching characteristics of the root system, namely root architecture, plays a fundamental role (Gregory, 2008; Schwarz et al., 2010a). Due to variability among species, several attempts were made to characterise their root architecture, according to the growth stage. Taxonomy of juvenile seedlings is rather hard, as roots can change in shape, length and size quite fast at this growth stage (Cannon, 1949; Reubens et al., 2007). For more mature plants (i.e., shrubs), Yen (1987) distinguished root systems into five branching patterns (figure 2.7) and found beneficial VH-type for slope stabilisation and wind resistance, H-type for soil reinforcement and slope stabilisation, M-type for soil reinforcement, and V-type for wind resistance. Reubens et al. (2007) reviewed the previous classification to include size characteristics and root density. For very mature plants (i.e., trees), (Cannon, 1949) classified root according to the presence of primary and secondary, eventually adventitious, roots (figure 2.8). A more simple classification was made by Klopstra et al. (1996) with respect to the shape and direction of the main and secondary axes of root branches.

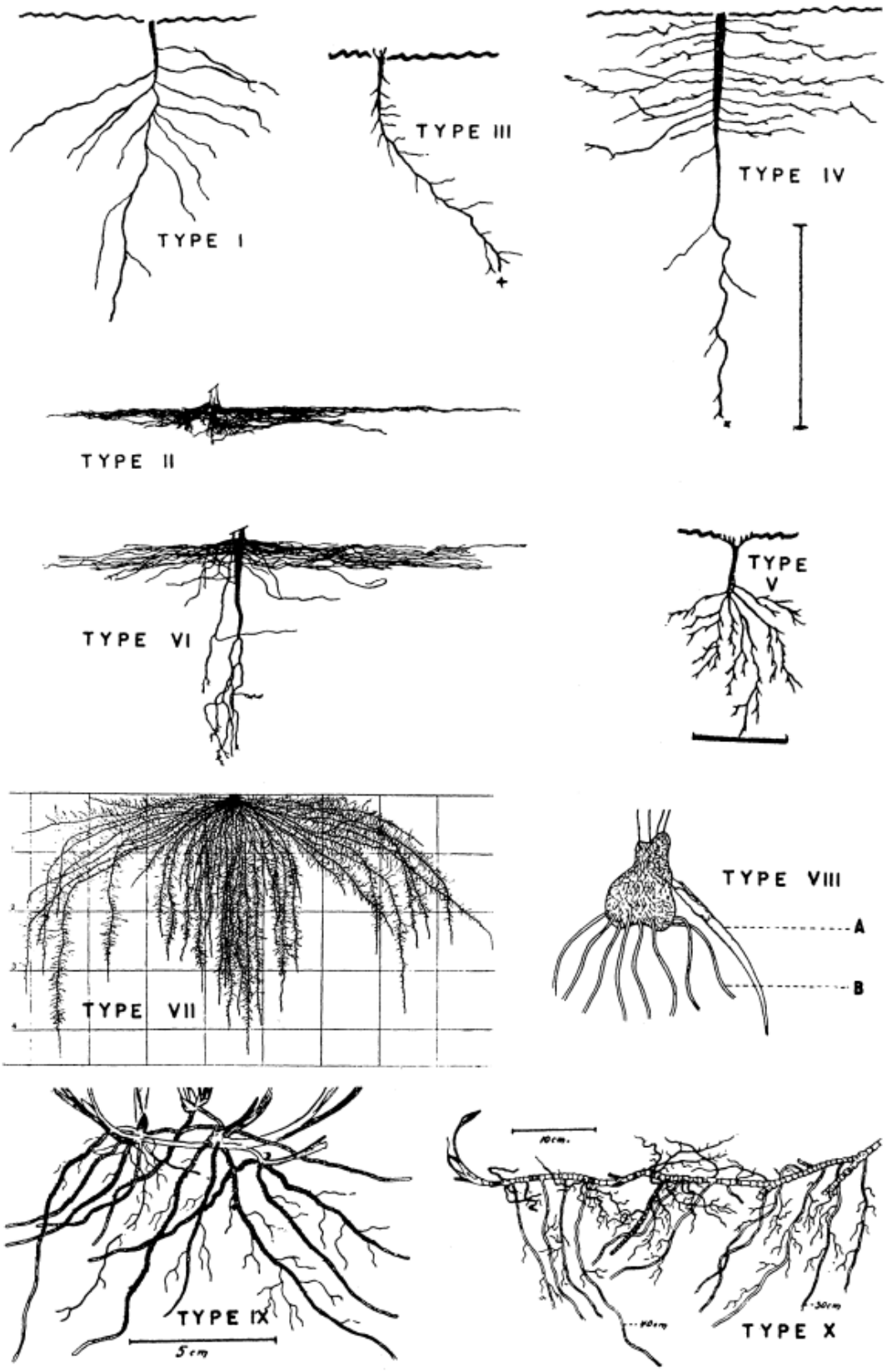

FIGURE 2.8: Plant root system classification by Cannon (1949). I - VI primary root systems; VII - X adventitious root systems (adapted from Cannon (1949)).

2.6 Root resistance to uprooting

Flooding events can cause young vegetation mortality by burying it with sediment (Carter Johnson, 2000) or by uprooting (Tanaka and Yagisawa, 2009). Although plant removal can occur even during windfall events (Schaetzl et al., 1989; Ulanova, 2000), hereafter we refer to *uprooting* as vegetation decay induced by water flow. River evolution in the presence of vegetation depends on establishment of pioneer woody riparian seedlings on bars, and consequently on either their survival or death (Mahoney and Rood, 1998; Karrenberg et al., 2002; Corenblit et al., 2007).

FIGURE 2.9: Uprooted tree along the Feshie River. Photo taken near the *Ruigh Aiteachain* bothy, Scotland (UK).

Plant resistance to uprooting (i.e., anchorage) is a complex mechanism depending on both root (length, diameter, architecture), soil (grain size distribution, shear strength, moisture content) and root-soil interface properties (Dupuy et al., 2005; Pollen, 2007; Schwarz et al., 2010c, among others). As a consequence, plant uprooting occurs due to the failure of the weakest link among them. Following Ennos (1990), in the hypothesis of vertical cylindrical roots with constant diameter, root

anchorage can be modelled as:

$$F_R = \min \begin{cases} N_T \, \frac{\pi}{4} \, D_r^2 \, \sigma_r & \text{for root breakage} \\ 2 \, \pi \, L_r^2 \, \sigma_{soil} & \text{for soil tensile failure} \\ N_T \, \pi \, D_r \, L_r \, \tau_{soil} & \text{for root-soil slipping} \end{cases} \tag{2.3}$$

where F_R is the resisting force due to root anchorage; N_T is the total number of roots; L_r and D_r are the mean length and diameter of roots, respectively; σ_r is the root tensile strength; σ_{soil} is the soil normal stress; τ_{soil} is the soil shear strength. Accordingly, the optimal strategy for plant anchorage is to grow roots in such a way to make failure mechanisms equally resistant (Ennos, 1993). By comparing relations in Eq. (2.3), Pollen (2007) concluded that juvenile seedlings with smaller diameter roots are more likely to be pulled out of the soil (root-soil slipping), whereas mature plants with larger and longer roots are more likely to be uprooted due to root breakage. Additionally, Tanaka and Yagisawa (2009) showed that soil tensile failure can occur in well developed root systems, such as that of mature trees.

Measurements of root resistance to uprooting are typically carried out by means of static pull-out tests along the vertical direction, although this method was proved to provide overestimation (Coutts, 1983). Indeed, drag load by wind or water acts more along the horizontal than the vertical direction (Coutts, 1983; Stone et al., 2013). Consequently, only upstream side of root system is subjected to tension, whereas the downstream one has to withstand compression. This mechanism leads to an unequal distribution of load among the different root branches, and thus to reduction of global root resistance (Coutts, 1983). Nevertheless, vertical pull-out measurements

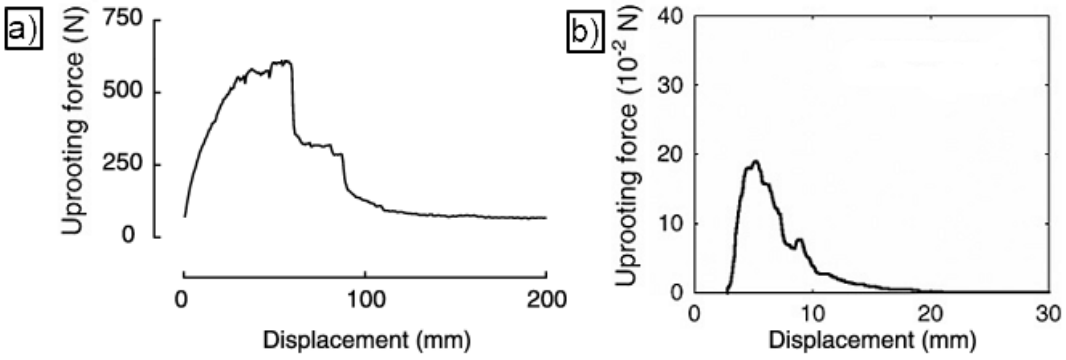

FIGURE 2.10: Typical force–displacement curves of vertical pull-out tests for different plants. a) 86 cm tall *Populus nigra* sapling; b) 26 cm long root *Avena sativa* seedling. Notice the different magnitude of uprooting force (modified from Karrenberg et al. (2003) and Edmaier et al. (2014b)).

(figure 2.10) were carried out both in laboratory setup mainly regarding crop species or hillsides vegetation (e.g., Ennos, 1989; Bailey et al., 2002; Mickovski et al., 2005; Edmaier et al., 2015) or artificial root systems (e.g., Dupuy et al., 2005; Mickovski et al., 2007; Mickovski et al., 2009; Schwarz et al., 2011) and in field campaigns considering hillsides vegetation (e.g., Pollen, 2007; Burylo et al., 2009; Schwarz et al., 2010b;

Burylo et al., 2012) or riparian vegetation on river bars and islands (e.g., Karrenberg et al., 2003; Tanaka and Yagisawa, 2009; Liu et al., 2011; Bankhead et al., 2017). All the studies agree upon root resistance increasing with root length (Yoshioka et al., 1998; Mickovski and Ennos, 2002; Edmaier et al., 2014b, among others). Accordingly, results were commonly presented with respect to main root length (e.g., Ennos, 1993; Pasquale et al., 2012; Perona et al., 2012a).

However, other studies presented results in respect of other factors and geometric dimensions. For instance, Karrenberg et al. (2003) and Liu et al. (2011), among others, considered the plant height, whereas, more recently, Bywater-Reyes et al. (2015) and Bankhead et al. (2017), among others, took into account plant frontal area as a reference for root resistance. It follows that such measurements are rather difficult to compare each other, even for similar species. Additionally and in contrast to previous studies, Bywater-Reyes et al. (2015) introduced lateral pull-out tests to measure root resistance of riparian species, as suggested by Stone et al. (2013), to simulate seedlings reconfiguration (section 2.3) during flood events (Manners et al., 2015). They also simulated different scouring conditions around stem and demonstrated reduction of root resistance due to soil erosion, as Edmaier et al. (2015) did in flume experiments under controlled conditions. Typical results of pull-out measurements are shown in figure 2.10, where failure of secondary roots are highlighted by jumps in the falling limb.

The presence of multiple roots is assumed to increase uprooting resistance. In case of perfectly cooperating roots, the global resistance is assumed equal to the sum of individual root strength (Ennos, 1990; Ennos, 1993; Bailey et al., 2002). However, this was found important only for juvenile seedlings at the early growth stage (Coutts, 1983), whereas assuming perfect cooperation in more mature root systems provides overestimation of root resistance (Pollen and Simon, 2005). Similar results were found by means of laboratory experiments by Giadrossich et al. (2013) using real plants and by Stokes et al. (1996) using copper cylinders to investigate the role of secondary branches. Conversely, the presence of root hairs was found rather irrelevant in increasing root resistance (Ennos, 1989; Ennos, 1993; Bailey et al., 2002).

In riverine ecosystems, vegetation uprooting occurs as a result of disequilibrium between drag force, F_D, due to water flow, buoyancy, F_B, and root anchoring, F_R (see figure 2.11). Edmaier et al. (2011) proposed a conceptual model to describe the occurrence of plant uprooting in non-cohesive soils, by distinguishing two different mechanisms. The first one, namely "Type I", occurs as an almost instantaneous plant pull-out due to root breaking or root-soil slipping when the resultant of buoyancy and drag forces acting on the plant (i.e., $\vec{F_B} + \vec{F_D}$) exceeds its anchoring resistance, $\vec{F_R}$. Type-I uprooting was found to be relevant only in very young vegetation, with relative short and simple root architecture (Edmaier et al., 2015; Bywater-Reyes et al., 2015). On the contrary, more mature vegetation with a deeper and stronger root

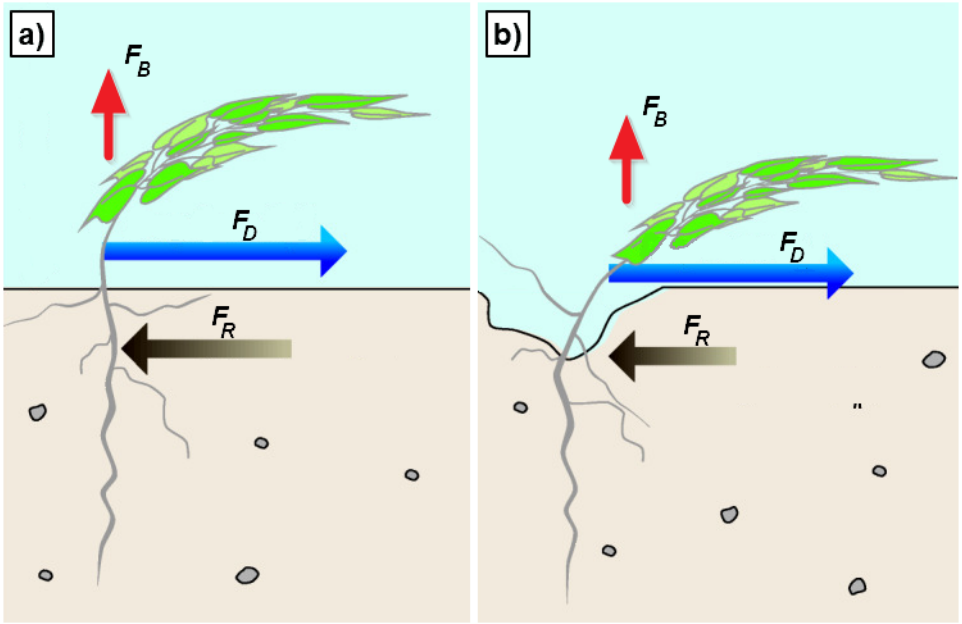

FIGURE 2.11: Conceptual model explaining the two mechanisms of flow uprooting proposed by Edmaier et al. (2011). a) Instantaneous "Type I" uprooting without bed scouring; b) Delayed "Type II" uprooting due to required erosion (modified from Bywater-Reyes et al. (2015)).

apparatus requires root resistance to be reduced before uprooting occurs. Such resistance lowering is mainly driven by soil erosion around plant stem, causing a partial exposure of the root system and, thus, decreasing the root anchorage. The second mechanism, namely "Type II", differs from Type I in the time delay introduced by the erosion process (figure 2.11), as scouring requires a certain time frame to develop (Edmaier et al., 2011). As a result, both the flow conditions and the factors controlling root anchorage, which are particularly species- and situ- dependent, contributes to vegetation uprooting (Edmaier et al., 2011; Edmaier et al., 2014a).

Bywater-Reyes et al. (2015) further distinguished the Type II mechanism according to the different source of erosion around the plant stem. Therefore, Type IIa accounts for self-induced scouring due to fluid-obstacle interactions. This leads to the formation of a horseshoe vortex upstream and around the plant stem, which in turn, promotes erosion (Dargahi, 1990; Crouzy and Perona, 2012). On the contrary, the erosion in Type IIb uprooting is mainly driven by larger length-scale processes, scaling with bar length or river width. Due to the small size of self-induced scour, whose depth scales with stem diameter and depends on stem-to-grain ratio (Melville and Sutherland, 1988), Bywater-Reyes et al. (2015) concluded that the uprooting of established vegetation (older than 2 years) in river bars mainly occurs for Type IIb mechanism. Conversely, the definition of the main uprooting mechanism for juvenile pioneer species still remains an open problem. This is particularly of interest as the position of plant species on a river bars was found to be correlated to their uprooting resistance (Ennos and Pellerin, 2000; Karrenberg et al., 2002) as a consequence of their growth stage (figure 2.12) (Hortobágyi et al., 2018; Serlet et al., 2018).

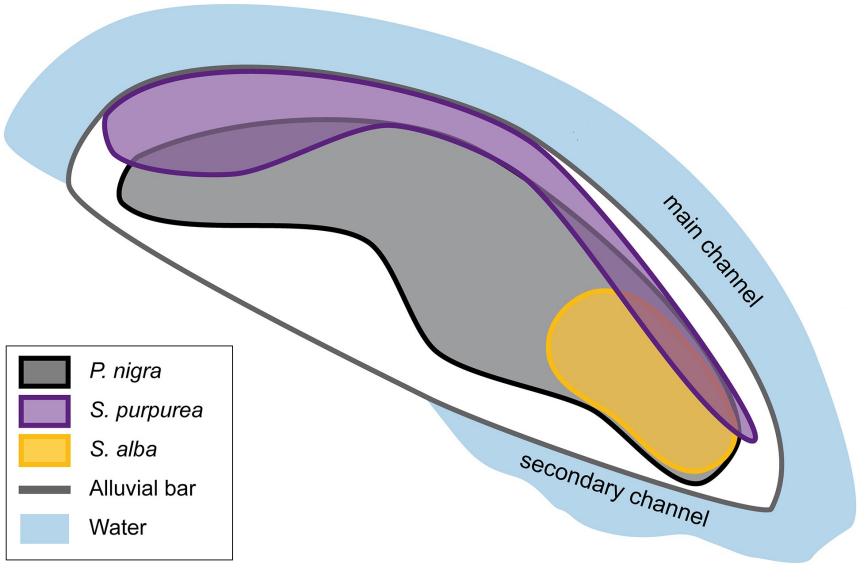

FIGURE 2.12: The average establishment area of different Salicaceae species on alluvial bars of the Allier River (FR). Colonised area is the result of interactions between species properties and flood magnitude and frequency (modified from Hortobágyi et al. (2018)).

More recently, Perona and Crouzy (2018) proposed a stochastic model to calculate the uprooting probability of riparian vegetation, by accounting for the time evolution of scour induced by superposition of deterministic large-scale (Type IIb) and randomly fluctuating small-scale (Type IIa) erosion, until a critical erosion length, L_e, is achieved. Caponi and Siviglia (2018) proposed a fixed quantification of such critical erosion length L_e based on the statistical root density distribution model by Tron et al. (2015), regardless of the above-ground biomass.

2.7 Eco-morphodynamic modelling

Fluvial morphodynamics influences vegetation according to its growth stage and affects its biological processes, from seed dispersal to wood transport, including recruitment, colonisation, succession and mortality (see Solari et al., 2016, for a review). As a result, riparian vegetation adapted to withstand periods of flooding, scour and burial (Karrenberg et al., 2002). Consequently, plant characteristics influence how morphodynamics affects vegetation itself (van Oorschot et al., 2016). Therefore, linking vegetation and fluvial processes acting at different spatial and temporal scales is essential to properly understand riverine state and evolution (e.g., Camporeale et al., 2013). Vegetation density dynamics $d\phi_v/dt$ is generally modelled as a balance between a positive growing term, proportional to the density itself and to the available space, and a negative decay term, proportional to water stress induced by flow depth and squared flow velocity (similarly to Eq. (2.2), in case of submerged vegetation). The so called *logistic law* (e.g., Levins, 1969; Corenblit et al.,

2009; Gurnell, 2014) reads:

$$\frac{d\phi_v}{dt} = \alpha_g \phi_v \left(\phi_m - \phi_v\right) - \alpha_d \phi_v Y U^2 \tag{2.4}$$

where ϕ_v is the vegetation density; t is time; α_g and α_g are the growth and decay rates of vegetation, respectively and ϕ_m is the maximum carrying capacity; U and Y are the average flow velocity and the water depth, respectively. Ye (2012) and Kim et al. (2014), among others, added further terms to account for diffusion and Brownian random dispersal, respectively.

From a mathematical point of view, coupling relations of vegetation dynamics to river morphodynamic Exner-Shallow water equations is rather complicated. Therefore, the problem can be approached only either by introducing simplifying hypotheses or by consider particular geometrical situations. For instance, Marani et al. (2010) modified Eq. (2.4) in terms of biomass to study the 0-D (point model) morphodynamic evolution of a tidal platform. The resultant equation was later used by Marani et al. (2013) and implemented in numerical modelling on river morphodynamics by Bertoldi et al. (2014). Perona et al. (2014) used a mono-dimensional approach to derive a closed-form relation for the vegetation front (cross-section width downstream which in-channel vegetation is likely to be removed) in spatially narrowing rivers. Furthermore, Bärenbold et al. (2016) and Bertagni et al. (2018) focused on 2-D alternate bars instability, accounting for the presence of vegetation. Additionally, Bertagni et al. (2018) included flow variability due to sudden jumps in flow discharge, followed by exponential decreases (i.e., Compound Poisson Process), to study the occurrence of transitions between vegetated and bare bars (figure 2.13).

FIGURE 2.13: Bare and vegetated alternate bars in straight rivers, as case study in Bertagni et al. (2018). Flow is from left to right. a) Bare bars in the Alpine Rhine, near Vaduz (LI); b) Vegetated bars in the Isére River near Arbin (FR).

However, when the problem becomes more complicated and no simplifications can be introduced, a different approach is required. In this sense, various attempts were made to model such interactions by means of laboratory setups (e.g., Braudrick et al., 2009; Tal and Paola, 2010; Dijk et al., 2013; Vargas-Luna et al., 2016), field investigations (e.g., Corenblit et al., 2007; Gurnell and Petts, 2006; Bertoldi et al., 2011; Hortobágyi et al., 2018) and numerical tools using cellular automata (e.g., Murray and Paola, 2003; Coulthard et al., 2006; Coulthard et al., 2007) or physics-based models (e.g., Perucca et al., 2007; Crosato and Saleh, 2011; Nicholas, 2013; Zen et al., 2016). As a common result, laboratory experiments and numerical models

agree upon vegetation promoting single-thread channel from multi-thread braiding systems. Physics-based numerical models included very specific relations for morphodynamic processes but most of them did not account for proper vegetation dynamics description (Solari et al., 2016). In this sense, models by Bertoldi et al. (2014) and van Oorschot et al. (2016) represented a breakthrough in numerical tools, as they included a more detailed description of vegetation dynamics, including, although in a simple manner, conditions for vegetation decay due to uprooting.

2.8 Discussion

In the last decades, riparian vegetation was recognised as a fundamental part of the complex riverine environement and the interactions between vegetation and fluvial morphodynamics gathered attention from researchers of different study fields (hydraulic engineering, geomorphology, biology, etc.). Sediment processes (i.e., erosion, transport and deposition) and vegetation dynamics (i.e., seed dispersal, recruitment, establishment, growth and decay) exhibit similar temporal scales, therefore their mutual interactions cannot be modelled separately. As a result, the quantification of spatiotemporal scales at which biotic and abiotic processes interact needs more attention.

Although these interactions were identified to act at various scales, only recently the mutual effects and feedbacks were simultaneously included in morphodynamic simulations. Modelling such feedbacks is still in its infancy due to oversimplification of either the morphodynamics or the vegetation dynamics. Accordingly, more efforts are required to fully integrate relationships for vegetation dynamics in river morphodynamic models considering the two-way coupled interactions at various flow conditions and spatial and temporal scales. Particularly, the threshold conditions of tangential stresses and scour that plants withstand before being uprooted require research attention to gain deeper understanding of the removal process.

The interdisciplinary approach is necessary to tackle the problem by means of different methods (laboratory setup, field investigations, numerical simulations, ecc.). Furthermore, the direct mathematical approach remains a fundamental tool to provide comprehension and insights of vegetation-fluvial system interactions, although the required simplifications. Improving knowledge of vegetation dynamics and its effects in fluvial systems is a basic requirement to increase modelling accuracy and reduce risk and uncertainties in morphodynamic evolution prediction, driven by alien species invasions under climate change scenarios and human interventions.

Chapter 3

Growth and decay rates of riparian vegetation in narrowing channels

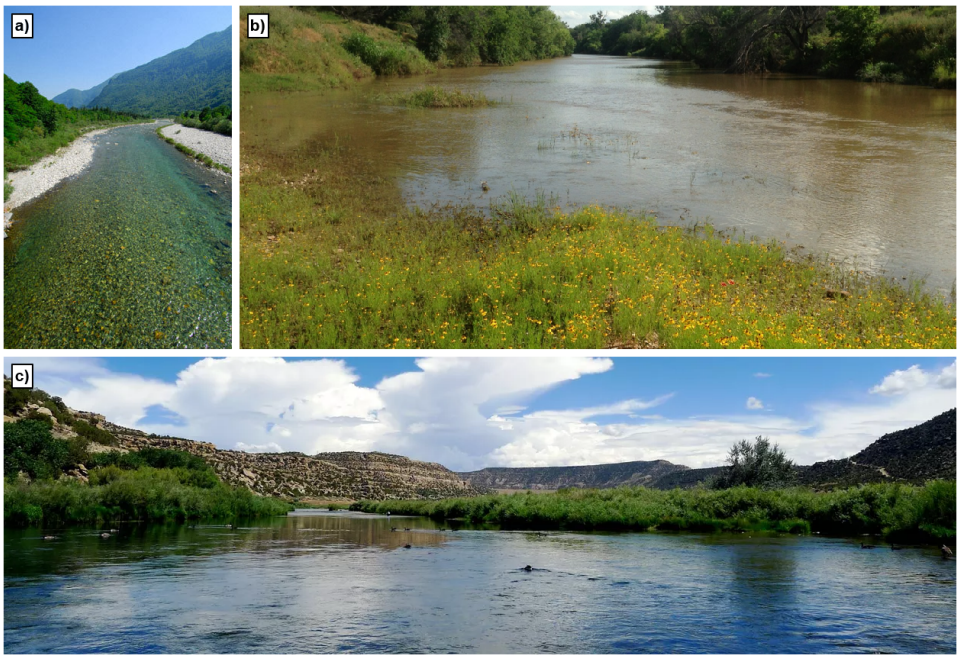

FIGURE 3.1: Different patterns and species of riparian vegetation in rivers. a) Downstream view of the Maggia River near Locado (CH) with pioneer seedlings at the edge of the lateral deposit on the right (source: https://www.alamy.com/stock-photo/river-maggia.html); b) Downstream view of the Colorado River near Elm Grove, Texas (USA) with herbaceous plants close to the main channel and mature vegetation on the riverbanks (source: https://www.txsportingproperties.com); c) Upstream view of the San Juan River after the Navajo Dam, New Mexico (USA) with cottonwood shrubs along the riverbanks (source: https://duranglers.com).

The interactions between vegetation and hydro-morphology at the reach scale is here examined in rivers with downstream converging banks.

The work included in this Chapter was conceived and performed while the candidate was visiting the School of Engineering of The University of Edinburgh (UK).
This chapter has been published by the author in *Earth Surface Processes and Landforms*: doi:10.1002/esp.4735 (Calvani et al., 2019b). Minor changes have been done for formatting purposes.

3.1 Introduction

Riparian and in-channel vegetation must be considered not only as either a source of additional drag to fluvial stream (e.g., Baptist et al., 2007; Nepf, 2012b; Vargas-Luna et al., 2015, among others) or an agent passively affecting sediment transport and morphological processes (e.g., Zong and Nepf, 2010; Vargas-Luna et al., 2016, among others), but also to play an active role within the riverine habitat (Gurnell, 2014). Therefore, it is fundamental to take into account the positive and negative feedbacks between hydro-morpho-dynamics and vegetation establishment, growth and decay (Edmaier et al., 2011; Perona et al., 2012a), in order to correctly model river evolution, particularly when referring to long-term predictions. Such mutual interactions gathered attention from scientific community only recently (e.g., see the review by Camporeale et al., 2013). Specifically, the attention to rivers with converging banks begun with the preliminary conceptual model on island formation proposed by Gurnell and Petts (2006) whereas Edmaier et al. (2015) and Bywater-Reyes et al. (2015) pioneered some studies on the removal conditions of vegetation due to flow in laboratory experiments and field campaigns, respectively. The resulting empirical relationships can be used only when referring to the specific vegetation types involved in their studies. Moreover, results of such predictions are affected by errors mainly originated by the lack of knowledge about the dynamical interactions between vegetation and river morphodynamics (Solari et al., 2016). Additionally, the temporal and spatial scales at which reciprocal feedbacks between river morphodynamics and riparian vegetation occur still remains an open question (Manners et al., 2015). Recently developed river eco-morphodynamic models attempt to bridge this gap, by taking into account specific equations for vegetation dynamics (i.e., growth and decay): particularly, the growing term is mainly related to plant-species properties (i.e., by neglecting dependence on nutrient availability and water table level, as usually occurs in river corridors (e.g., Pasquale et al., 2014)), whereas coefficients for decay and mortality due to flow uprooting is intrinsically related to both hydraulic conditions and plant root resistance (Edmaier et al., 2011).

To our knowledge, the first analytical approach to describe eco-morphodynamic interactions has been done by Perona et al. (2014), who derived a simple 1-D formulation for the river width where vegetation front is expected to occur in channels with converging banks. Results were validated using previously collected data from laboratory experiments (Perona et al., 2012a) but never applied to real case studies. As a matter of fact, in straight channels with parallel riverbanks, vegetation development is mainly imposed on already settled sedimentary emergent patterns, such as bars and islands, (Corenblit et al., 2007; Gurnell, 2014), whereas vegetated rivers with converging boundaries show the distinguishable pattern of a vegetated area inside the main channel downstream which plants are likely to be more easily removed (e.g., figure 3.2). In this planform configuration, due to the intrinsic

and dynamically active flow-biomass interaction, a distinctive sediment-plant pattern can be commonly found inside the main channel, particularly, a barebed area where pioneer vegetation is *on average* precluded to colonize and establish (Perona et al., 2014). Because of the narrowing longitudinal width, the stream is convectively forced to accelerate, resulting in increasing velocity and shear stresses which essentially affect local morphodynamics and promote plant uprooting (Perona et al., 2014), thus limiting the longitudinal establishment and growth of vegetation. Here we stress the term "*on average*" to highlight that the position of the vegetation front changes according to flow regime, but its averaged location is set on the long-term period (i.e., years). Indeed, such location depends on the inter-time between flood events and their magnitude. As a matter of fact, vegetation can colonise the area downstream such position during long low-flow or drought period but it is likely to be uprooted during following high floods, whereas upstream region still remains vegetated (e.g., figure 3.2). Therefore, vegetation front is the result of the mutual interactions between plant and river characteristics, which, at the front, depend on both biological and hydrological time scales.

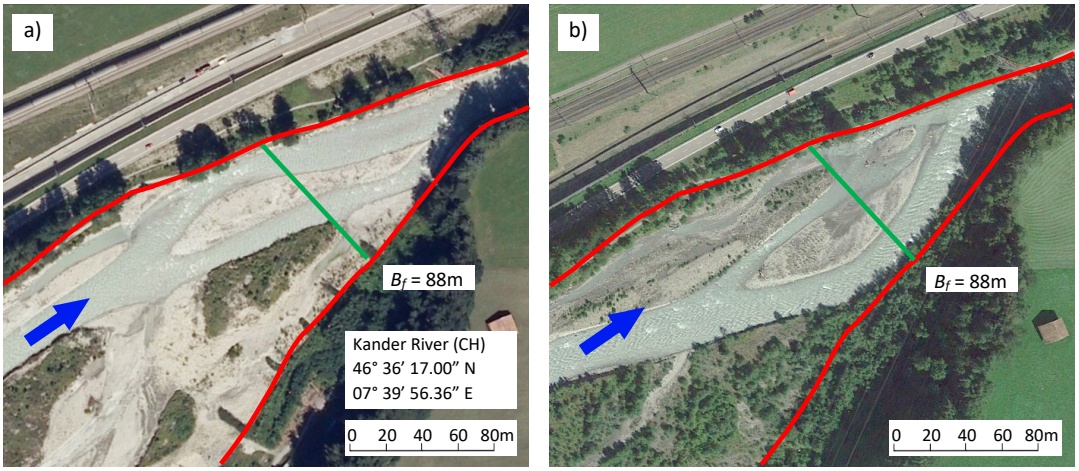

FIGURE 3.2: A river reach of the Kander River near Wengi bei Frutigen (CH) showing convergent banks highlighted by red lines (images from Google Earth). Flow is from left to right (blue arrow). Position (green line) and river width at the vegetation front, B_f, are shown. Although changes in the riverbed morphology, the vegetation front is stable. a) picture taken in October 2009; b) picture taken in August 2016.

In this work, we studied the interactions between riverbed vegetation and river morphodynamics at the reach scale by following the approach of Perona et al. (2014) for rivers with converging banks. We first validated the formula for the river width where vegetation front is expected by using already collected data about flow discharge, grain size curve, sediment transport and riparian vegetation size and growth rate from natural worldwide rivers. Then, we used the validated formula to calculate the flow discharge return period and the flow decay coefficients characterizing the vegetation pattern. Lastly, we could correlate biological parameters of growth and decay to hydrological time scales, and, as a result, prove that vegetation plays a fundamental role in defining the equilibrium conditions of a river reach according

to the different species.

3.2 Materials and Methods

Most of the river reaches with converging banks show the existence of a specific cross-section beyond which vegetation is on average precluded to establish, i.e., there exists a front where vegetation vanishes. Perona et al. (2014) experimentally showed that this results from the intensifying capacity of flow to uproot vegetation due to increasing velocity in the convergent reach. They theoretically derived a formula to calculate the river width where vegetation front is located by taking into account biomass dynamics, the steady state of the system from a one-dimensional approach, the approximation of rectangular cross section, the equation of Baptist et al. (2007) for the bed roughness with non-submerged vegetation and a modified version of Meyer-Peter-Müller relation for bedload transport which accounts for the additional critical Shields stress due to the presence of roots (Pasquale et al., 2011). The proposed equation reads:

$$B_f = n^{-3/4}\, D_G^{3/8} \left(\tau_c^* + q_s^{2/3}\right)^{3/8} \left(\frac{\beta}{\phi_m}\right)^{7/8} Q \tag{3.1}$$

where B_f is the river width where the vegetation front is located; n is the Manning's coefficient; $D_G = D_{50}\left(\frac{\rho_s}{\rho} - 1\right)$ is a parameter combining median grain size D_{50}, sediment density ρ_s and water density ρ; τ_c^* is the critical dimensionless Shield stress for the initiation of sediment movement; $q_s = \frac{Q_s}{k\,B}$ is the dimensionless sediment transport per unit width with $k = 8\,D_{50}\,\sqrt{D_G\,g}$ and B is the river width; β is a parameter representing the ratio between vegetation decay rate α_d and growth rate α_g; ϕ_m is the maximum carrying capacity; Q is the average flow discharge at the steady state.

While the critical dimensionless Shield stress for the incipient sediment transport τ_c^* should take into account the presence of plants in the vegetated areas (Pasquale et al., 2011), the value for barebed conditions (e.g., Chiew and Parker, 1994) can be assumed when dealing with the area near the vegetation front, where vegetation density is negligible ($\phi_v \approx 0$). Additionally, it is important to highlight that, while hydraulic coefficients, sediment transport parameters, biomass carrying capacity ϕ_m and growth rate α_g can be easily calculated or retrieved from literature, the decay rate α_d, thus β, and the average flow discharge Q are in general difficult to estimate, and therefore often unknown.

The logistic law for the dynamics of vegetation density ϕ_v can be expressed as (Camporeale and Ridolfi, 2006):

$$\frac{d\phi_v}{dt} = \alpha_g \, \phi_v \, (\phi_m - \phi_v) \, - \alpha_d \, \phi_v \, Y \, U^2 \tag{3.2}$$

Therein, α_g is the growth rate, α_d is the decay rate due to flow uprooting, Y is the flow depth and U is the mean flow velocity. We recall that the growth rate α_g depends on species characteristics only (i.e., when water and nutrients are continually available, as expected in riverine habitats), whereas the decay rate α_d is related to both hydraulics and vegetation properties (Edmaier et al., 2011). If we assume that

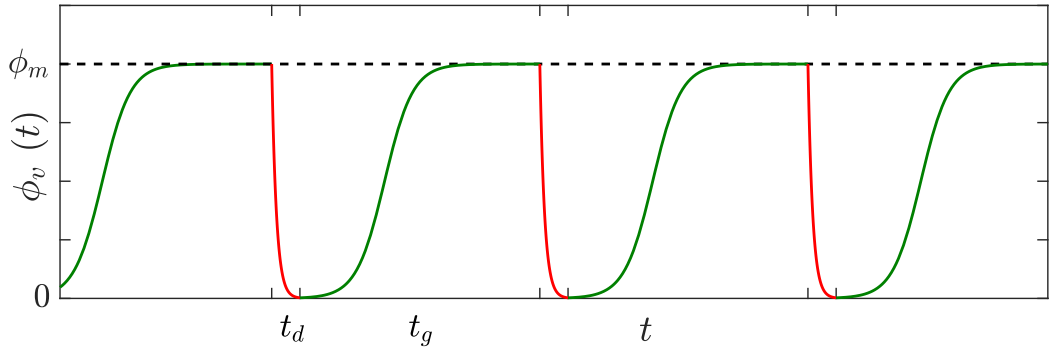

FIGURE 3.3: A possible solution to the logistic law for vegetation dynamics (Eq. (3.2)) when growth and decay terms are separately active. Green line represents the solution considering the growing term governed by α_g and t_g is its duration. Red line is the solution considering the decay rate α_d only and t_d is the decay duration.

growth and decay due to flow are separately active, a possible solution to the logistic law (Eq. (3.2)) is given in figure 3.3. Accordingly, we hypothesise that, over a total period $t_d + t_g$, the growth and decay terms are active for fractions $\frac{t_g}{t_d+t_g}$ and $\frac{t_d}{t_d+t_g}$, respectively (Bärenbold et al., 2016; Crouzy et al., 2016). By accounting for the negligible vegetation density at the front (i.e., $\phi_v \ll \phi_m$) and the steady state of the solution (i.e., $\frac{d}{dt} = 0$), as hypothesised by Perona et al. (2014), we modify the logistic law and obtain:

$$\alpha_g \, \phi_m \, \frac{t_g}{t_g + t_d} - \alpha_d \, Y \, U^2 \, \frac{t_d}{t_g + t_d} = 0 \tag{3.3}$$

where t_g is the time for which vegetation grows and t_d is the time for which vegetation is removed due to uprooting. Without entirely reporting the mathematical derivation, for which we address the reader to Perona et al. (2014), here below we propose to use Eq. (3.3) in order to rewrite Eq. (3.1) as

$$B_f = n^{-3/4} \, D_G^{3/8} \, \left(\tau_c^* + q_s^{2/3}\right)^{3/8} \, \left(\frac{\beta}{\phi_m}\right)^{7/8} \, Q_d \, \left(\frac{t_d}{t_g}\right)^{7/8} \tag{3.4}$$

where Q_d is the *reference* flow discharge governing bio-morphological changes at the reach scale, a sort of formative discharge controlling vegetation establishment, growth and decay. Again, hydro-morphological (i.e., mean grain size and critical Shields number) and biological (i.e., carrying capacity and growth rate) parameters

can be easily obtained from literature or quick field campaigns. On the contrary, quantities related to vegetation decay (i.e., α_d) and temporal durations (e.g., t_d and Q) can be obtained by intensive field investigations over long monitoring periods only.

Here we propose a procedure to calculate the vegetation dynamics parameters and overcome the issue. Firstly, we assume that the equilibrium at the reach scale is achieved over a yearly time scale, that is $t_g + t_d = 365$ days. Secondly, as the flood events able to uproot vegetation are rare, we expect $t_d \ll t_g$ (figure 3.3) and, as a result, it follows $t_g \approx 365$ d. By doing so, we assume the disturbances induced by high floods having a negligible effect on vegetation growth. Now, by comparing Eq. (3.1) and Eq. (3.4) and using the approximation for t_g, it is easy to obtain:

$$Q \cdot 365^{7/8} = Q_d \cdot t_d^{7/8} \tag{3.5}$$

which represents a relation among the flow discharge at the steady state Q, the *reference* flow discharge Q_d and the decay duration t_d. Lastly, the flow duration curve is involved in the system of equations, to have an additional relation between flow discharge and time.

FIGURE 3.4: Convergent banks in rivers are an ubiquitous planform configuration. a,b) Worldwide location of the river reaches included in the analysis (images from Google Earth).

We started our analysis by retrieving data for hydraulic (historical daily mean flow discharge), sediment (grain size curve and sediment transport rate) and riparian vegetation properties (species, cover percentage, age and dimensions) for rivers showing a reach with converging banks. We could collect data for 19 rivers and a total of 35 reaches (figure 3.4). Although convergent boundaries is a worldwide ubiquitous pattern (see figure 3.4 and figure 1 in Perona et al. (2014)), we selected river reaches according to the availability of previously collected data. For reaches in the same rivers, for which we could not find specific data on sediment transport and vegetation cover, we used information from the near cross section. Data about flow discharge were collected at the closest measuring station and used to calculate the yearly duration curve of daily mean flow discharges, while grain size curve and

sediment transport rate were taken from previous studies (see complete references after Table A.1). We used the D_{50} to calculate the coefficient D_G and the D_{90} to calculate the Manning coefficient n in Eq. (3.1). For the riparian vegetation properties, we collected data from previous monitoring studies, particularly concerning species, cover percentage, maturity age and maximum diameter at maturity age (see Table A.1 for references about vegetation data). For each river reach, we characterized the vegetation by averaging the parameters of growth rate α_g and carrying capacity ϕ_m of each species, according to cover percentage, as

$$\overline{\phi}_m = \frac{1}{4046.86} \sum_i \frac{C_i}{b_{0,i}} \left(\frac{D_{m,i}}{0.0254} \right)^{-b_{1,i}} \tag{3.6}$$

$$\overline{\alpha}_g = \frac{\pi}{4 \cdot 31536000} \sum_i \frac{C_i \, D_{m,i}^2}{T_{m,i}} \tag{3.7}$$

Therein, C_i is the cover percentage and $D_{m,i}$ is the diameter at maturity age $T_{m,i}$ of the i$-th$ species, being $b_{0,i}$ and $b_{1,i}$ two coefficients related to the family of the plant. Eq. (3.6) was modified from Arner et al. (2001) whereas we derived Eq. (3.7) by considering the growth rate of each single species to be constant during the whole life-stage (i.e., the maturity age $T_{m,i}$). Then, according to similar properties of the predominant vegetation species and cover, the 35 study reaches were gathered in 8 different groups. Table 3.1 summarises group properties and river reach characteristics, whereas all the data can be found in Table A.1. Lastly, we took measurements of river width at the vegetation front from Google Earth (e.g., figure 3.2).

TABLE 3.1: Main vegetation properties and river reaches for each group included in the analysis.

Group	Main properties	Species	Cover	ID	River reaches[a]
1	Populus $\geq$ 64%	Balsam poplar	64%	1	Clearwater 1
		Other willows	33%	2	Clearwater 2
		Sandbar willow	3%	3	Clearwater 3
		Douglas fir.	77%	16	Salmon
		Sandbar willow	23%		
		Plains cottonwood	78%	32	Yellowstone 1
		Russian olive	16%	33	Yellowstone 2
		Sandbar willow	6%	34	Yellowstone 3
				35	Yellowstone 4
2	Populus < 55% Tamarix > 30%	Fremont cottonwood	52%	14	Rio Grande 1
		Salt cedar	41%	15	Rio Grande 2
		Russian olive	6%		
		Sandbar willow	1%		
		Plains cottonwood	42%	17	San Juan 1
		Russian olive	29%	18	San Juan 2
		Salt cedar	29%		
		Salt cedar	43%	19	San Juan 3
		Russian olive	36%	20	San Juan 4
		Plains cottonwood	21%		

Group	Main properties	Species	Cover	ID	River reaches[a]
3	Salix > 30%	Salt cedar	56%	4	Colorado 1
		Other willows	30%	5	Colorado 2
		Box elder	14%	6	Colorado 3
		Goat willow	66%	7	Endrick
		Common alder	17%	8	Feshie
		Scots pine	17%		
		Sandbar willow	82%	31	Yampa
		Box elder	18%		
4	Eleagnus > 30%	Other willows	60%	11	Little snake 1
		Russian olive	40%	12	Little snake 2
5	Celtis	Netleaf hackberry	100%	23	Snake 1
				24	Snake 2
6	Thuja	Western cedar	79%	13	NF Clearwater
		Box elder	13%		
		Other willows	8%		
		Western cedar	59%	21	Selway 1
		Ponderosa pine	22%	22	Selway 2
		Other willows	19%		
7	Alnus & Pinus	Grey alder	57%	9	Johnson
		Red osier dogwood	43%	25	SF Salmon 1
				26	SF Salmon 2
8	Acer, Betula & Picea	Norway spruce	46%	10	Kander
		Scots pine	31%		
		Grey alder	23%		
		Common alder	40%	27	Tay
		Downy birch	40%		
		Scots pine	20%		
		Salt cedar	62%	28	Virgin
		Freemont cottonwood	23%		
		Black willow	15%		
		Water birch	48%	29	Wind 1
		Spruce	36%	30	Wind 2
		Narrowleaf cottonwood	16%		

[a]Numbers, when present, refer to different reaches in the same river

At this point, we have a system of three equations (i.e., Eqs (3.1), (3.5) and flow duration curve for each river reach) but four unknowns: the parameter $\beta = \frac{\alpha_d}{\alpha_g}$, the *reference* flow discharge Q_d, the time durations t_d and the flow discharge at the steady state Q. We solve the problem by exploring the space of solutions in terms of the unknown parameter β over a range of values covering 4 orders of magnitude (i.e., from 10^0 to 10^3 $s^2\,m^{-5}$) for each river reach in a group. Once fixed a value of β, the flow discharge at the steady state Q can be calculated by reversing Eq. (3.1). It is now straightforward to calculate the left-hand side term in Eq. (3.5). Then, by using the flow duration curve, it is possible to calculate the (t_d, Q_d) couples (right-hand side

term in Eq. (3.5)) that solve the problem. Usually, two pair values appear as solution (the quantity $Q_d \cdot t_d^{7/8}$ has a typical parabolic like shape) and, between them, we select the one with higher Q_d according to the initial hypothesis $t_d \ll t_g$. The procedure is graphically explained in figure 3.5: the flow duration curve (continuous blue line) is multiplied, once, by the quantity $365^{7/8}$ (continuous red line) to calculate the left-hand side term and, once, by the corresponding time $t^{7/8}$ (dashed red line) to obtain the right-hand side quantity in Eq. (3.5). Flow discharge Q_d and the corre-

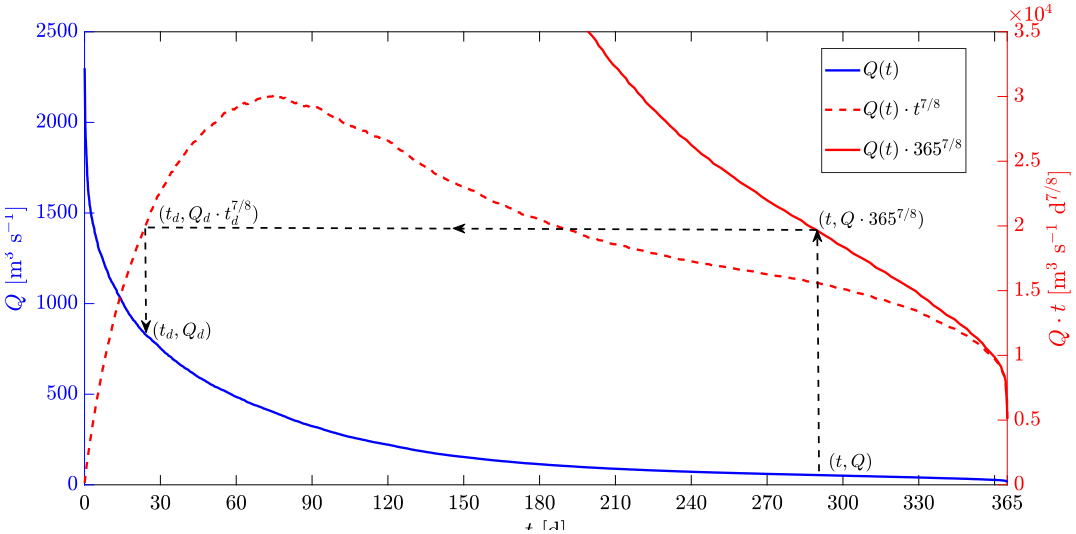

FIGURE 3.5: A common flow duration curve (continuous blue line) and the associated parabolic-like shape curve obtained as a result of the product by its duration time to the power of 7/8 (dashed red line). Continuous red curve is the flow duration curve multiplied by $365^{7/8}$. Dashed black lines show the calculation of the flow discharge Q_d and its relative duration time t_d.

sponding time t_d are recorded for all the river reaches in the same group (i.e., similar vegetation cover) and, then, we calculate the standard deviation of the flow duration t_d, for each tested value of the parameter β. Figure 3.6 shows the clear trend of such standard deviation at varying the parameter β for some groups of river reaches. As a result, it is possible to identify a minimum in the standard deviation, and, as we are dealing with equilibrium conditions, a minimum in a function seems to suggest the presence of scaling laws associated to the predominant vegetation cover. Moreover, we argue that it is unlikely that different river reaches, with different hydraulic conditions and morphological characteristics, can satisfy the predicting relation (Eq. (3.1)) and show the existence of such minimum in the t_d standard deviation without it being the expression of an underlying fundamental dynamics depending on similar vegetation cover. In the end, for a particular vegetation cover (i.e., group of river reaches), we select the value of the parameter β corresponding to the minimum in the t_d standard deviation, the calculated *reference* flow discharge Q_d and its associated flow duration t_d. Lastly, for the river reaches in a group, we calculate an average decay rate $\overline{\alpha}_d = \beta \cdot \overline{\alpha}_g$.

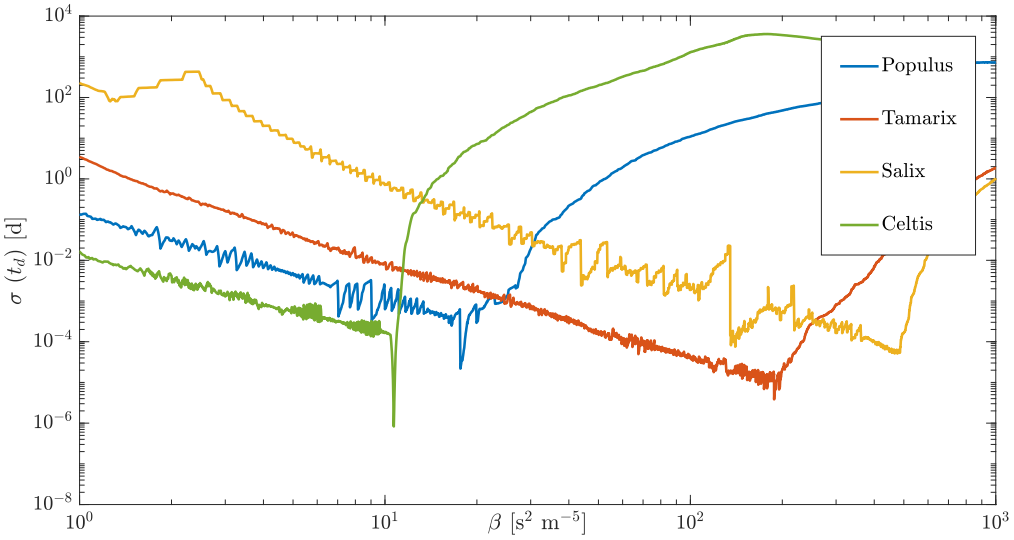

FIGURE 3.6: t_d standard deviation (σ) versus the parameter β at varying the vegetation cover properties (i.e., river group). The curves show the t_d standard deviation slowly decreasing and fast rising after having reached a minimum.

3.3 Results

We first used the proposed procedure and a dataset of different vegetation cover properties and hydro-morphological characteristics to validate the relation derived by Perona et al. (2014). We explored the space of the unknown parameter β (i.e., the ratio between decay and growth rates) over four orders of magnitude (i.e., from 10^0 to 10^3 s^2 m^{-5}, see figure 3.6). As a matter of fact, for higher values of the parameter β, either Eq. (3.1) does not provide any solution or the solution shows very high t_d standard deviation. As a result, we obtained different values for the parameter β according to the different vegetation properties. We argue that it depends on the interactions among river morphology (i.e., river width), river hydrology (i.e., flow duration curve) and, intrinsically, the characteristic of the vegetation (i.e., species and coverage). We interpret these interactions and the existence of the minimum in the t_d standard deviation as the orchestrated dynamical action of flow and morphological adjustments which together contribute to select vegetation species sharing biomechanics properties that guarantee their survival in such environments. We used such values of the β parameter to predict the river width at the vegetation front and compare it against the measured one (e.g., figure 3.2). Figure 3.7 shows the comparison between measured and calculated river widths at the vegetation front for each tested river reach. For most of the rivers, the error for the calculated width at the vegetation front is within $\pm$ 20% bound, resulting in a high value of the correlation coefficient ($R^2 = 0.926$). We applied the proposed procedure and the previous calculated β parameters to two additional rivers not included in Table 3.1: the Tagliamento River (see figure 3.8) (Gurnell and Petts, 2006)) and the Maggia River (see Figure 9 in Perona et al. (2014)). We found very good agreement between measured

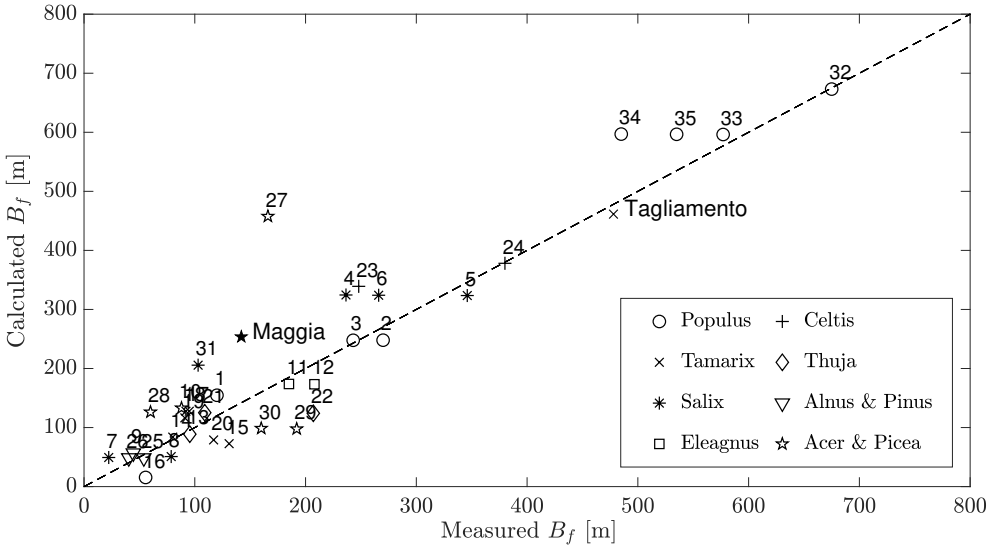

FIGURE 3.7: Comparison between measured and calculated river width at the vegetation front (B_f) for the tested river reaches, according to different vegetation cover (Group ID). The comparison for the Maggia River (Group 8 - black star) and the Tagliamento River (Group 2 - black cross) is shown as validation cases.

and calculated width at the vegetation front for the case study of the Tagliamento River, whereas the agreement is fairly less good for the Maggia River. The altered flow regime due to upstream flow regulation, in the case of the Maggia River, modified the flow duration curve and, as a result, the return period for moderate flood controlling the vegetation growth and decay is affected when compared to that of natural flood events. Similar conclusion was given by Perona et al. (2014) as well.

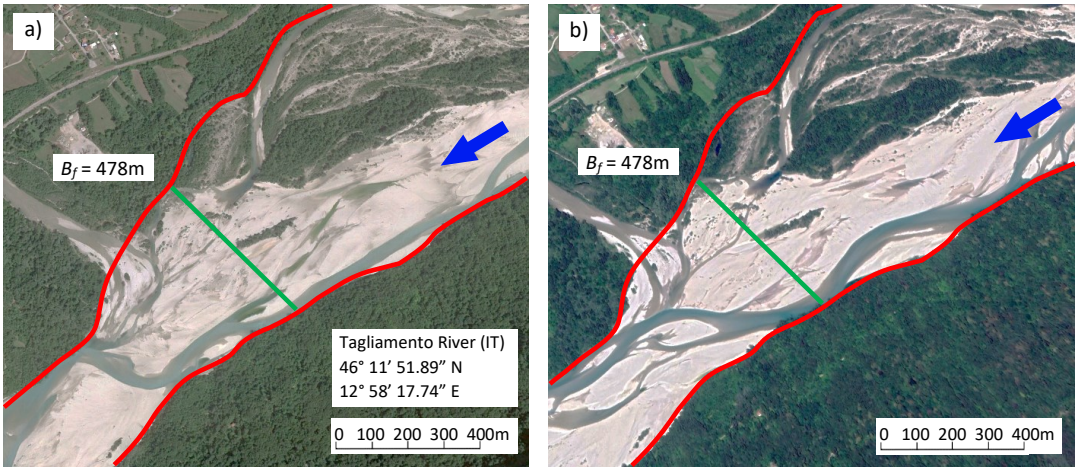

FIGURE 3.8: A river reach of the Tagliamento River near Forgaria nel Friuli (IT) showing convergent banks highlighted by red lines (images from Google Earth). Flow is from right to left (blue arrow). Position (green line) and river width at the vegetation front are shown. Although changes in the riverbed morphology, the vegetation front is stable. a) picture taken in July 2015; b) picture taken in June 2018.

Furthermore, the procedure proposed in this work allows to calculate the flow magnitude Q_d, its percentile (namely t_d) in the flow duration curve and, additionally, its return period (i.e., t_d^{-1}). Eventually, Eq. (3.5) provides the equivalent steady state

flow discharge Q to be involved in Eq. (3.1). We combined such results in scaling relationships both for the averaged vegetation decay $\overline{\alpha}_d$ and the averaged growth $\overline{\alpha}_g$ rates, with respect to the different hydrological time scales. Consequently, we could correlate the first one to the time t_d, which fairly resembles the duration of a flood event (figure 3.9). It is well acknowledged, indeed, that only during high flood events vegetation can be uprooted and removed, due to the simultaneous action of flow drag and bed erosion (Type II uprooting according to Edmaier et al. (2011)). Figure 3.9 shows that each vegetation cover has a particular combination of decay rate and temporal scale t_d governing its removal process. For instance, plant species of Group 2 and 4 (e.g., Tamarix and Eleagnus) are prone to uprooting (i.e., high $\overline{\alpha}_d$) and can be uprooted with shorter t_d temporal scale. On the contrary, plants species of Groups 1 and 5 (e.g., Populus and Celtis) resulted stronger against uprooting (i.e, low $\overline{\alpha}_d$) and require, for instance, deeper bed erosion for their removal during a flood event. As a result, it turns out that instantaneous uprooting (Type I

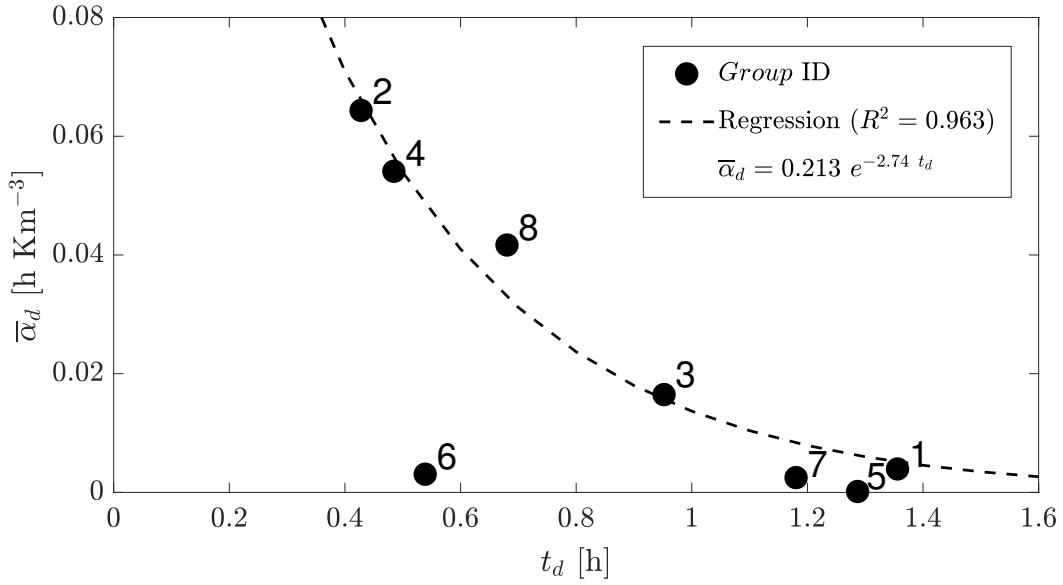

FIGURE 3.9: Average vegetation decay coefficient $\overline{\alpha}_d$ versus the characteristics time t_d in the flow duration curve controlling the biomorphological properties at the reach scale. Each vegetation cover is characterised by a particular combination of decay rate $\overline{\alpha}_d$ and temporal scale in the flow duration curve, showing that underlying interactions between hydro-morphology and vegetation govern the uprooting process at the reach scale, according to the different plant species.

according to Edmaier et al. (2011)) is unlikely to occur in riverine habitats with already established vegetation and certain flood duration is required for morphological changes (i.e., bed erosion) to reduce root anchoring and promote plant uprooting (Perona and Crouzy, 2018; Calvani et al., 2019a). Moreover, we could correlate the average growth rate $\overline{\alpha}_g$ to the return period of the flow magnitude Q_d, which represents a reasonable timescale for plants to start colonising, establish and grow on river bare bedforms. The flood return period $T(\xi)$ was calculated as the reciprocal of the timescale t_d: for the sake of clarity, $T(\xi)$ is the return period of a daily flow discharge equal to the *reference* flow discharge Q_d. The results of the correlation are

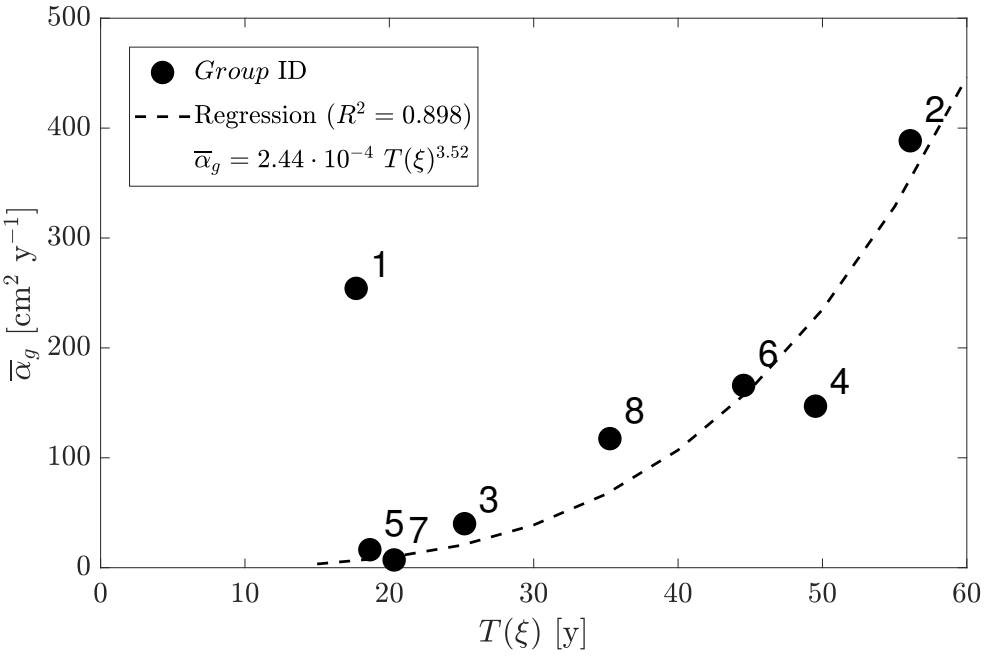

FIGURE 3.10: Average vegetation growth rate $\overline{\alpha}_g$ versus the return period $T(\xi)$ of the flow controlling the river width at the reach scale. Species with higher growth rate can develop a strong root apparatus so withstand and survive to higher flow discharges. Conversely, slowly growing plants are more susceptible to be uprooted even for low flow events.

shown in figure 3.10. Particularly, figure 3.10 highlights that plants with low growth rate (e.g., Group 5 and 7) can survive in fluvial systems characterised by low flow magnitude Q_d (i.e., short return period $T(\xi)$). On the contrary, species with higher growth rate can withstand higher flood events. In this regard, the case of Tamarix species (Group 2) represents a particular case, as this species is recognised to be invasive in many ecosystems and, once established, very hard to removed (e.g., Sher et al., 2002; Stromberg et al., 2007). In such a way, the results suggest that in a given hydro-morphological fluvial system (i.e., once the channel geometry, grain size distribution and hydrological regime are fixed), only some plants species, and within the same species, only mature plants (i.e., old enough to have developed a strong root apparatus) can tackle flood events. We interpreted these biomorphological scaling relationships as the ability for rivers to select vegetation according to their growing and survival properties. On the contrary, such relationships quantify the ability for plants species to withstand convectively increasing specific stream power within the converging channel and the particular hydrological conditions.

3.4 Discussion

The role of riparian and in-channel vegetation is commonly acknowledged among the factors controlling the morphodynamic evolution of fluvial environments (see Camporeale et al., 2013, for a review). As the presence of such biological component started to be taken into account in modelling only recently (e.g., van Oorschot

et al., 2016), the morphodynamic equilibrium at the reach scale is usually modelled by means of empirical relationships, mostly related to bankfull discharge or other characteristic values (e.g., Parker et al., 2007; Wilkerson and Parker, 2010), without explicitly accounting for the presence of vegetation. Figure 3.11 shows the comparison between the measured width at the vegetation front and the predicted bankfull width using the Lacey's relationship (Savenije, 2003) for the steady state flow discharge Q resulting from the performed analysis.

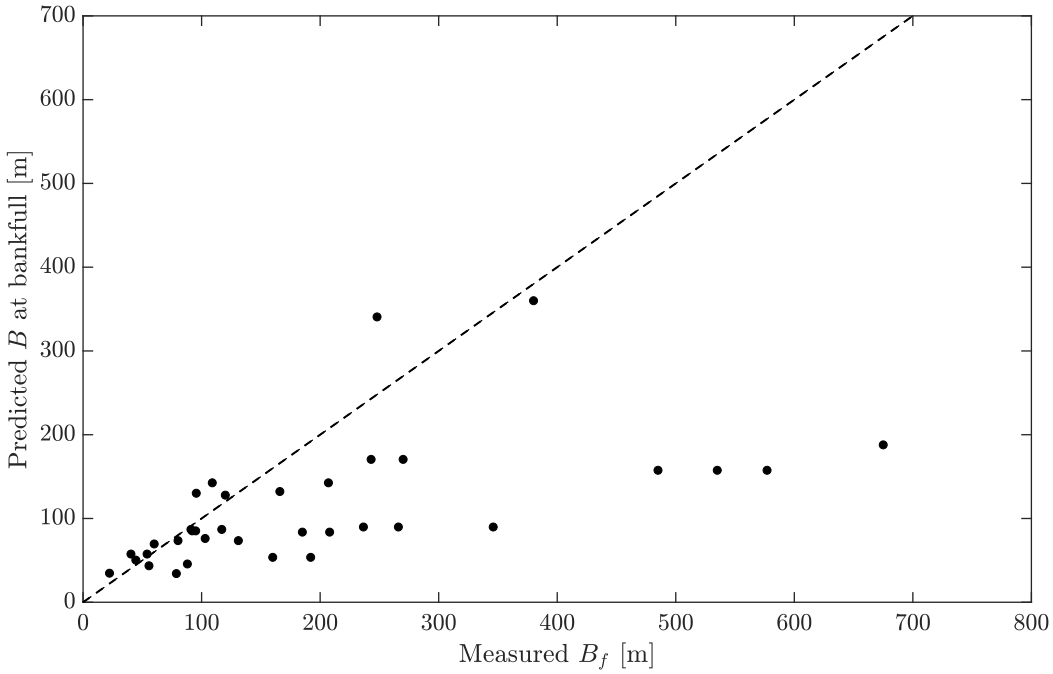

FIGURE 3.11: Comparison between measured width at the vegetation front and the bankfull width predicted using Lacey's relation for the steady flow discharge Q. Agreement is good only for very small rivers whereas it is lost for widths larger than approximately 150m.

Results are somehow controversial: the bankfull predictor seems to work better in the cases where one can expect vegetation to play a significant role, that is when river width is narrower (i.e., measured B_f lower than 150 m). On the contrary, for wider rivers, the prediction works well with the proposed formulation (see figure 3.7 for comparison). This suggests that the steady state flow discharge Q in Eq. (3.1) is representative of bankfull discharge only for narrow fluvial systems (i.e., with $B_f <$ 150m), whereas the vegetation dynamics is governed by higher flow discharges in larger rivers. Similarly, vegetation front is located at the bankfull width in small streams, whereas its location is upstream (i.e., where river width is larger due to the convergent configuration) of the bankfull width correspondent to the flow discharge Q.

Figure 3.7 shows some predicting errors in the estimation of river width at the vegetation front. Such errors can be ascribed to the simplifications introduced in the model (Eq. (3.4)), with particular focus on the one-dimensional approach to river

geometry and flow. In this regard, for river reaches showing in-channel vegetated bars (see figure 3.2), it is straightforward to assume the steady state flow discharge Q as a conceptual value only, whereas the *reference* discharge Q_d represent the flow governing the vegetation dynamics. Additionally, the evolution of such large-scale bedforms (see figure 3.2) is not explicitly taken into account in Eq. (3.1) (the model is one-dimensional) but their influence on flow can be considered by an appropriate roughness coefficient n. Prediction errors can also be correlated to either measuring errors from Google Earth (although limited to some meters) or the different flow period when pictures were taken (e.g., low or high water stage). Furthermore, in some cases, due to the absence of measuring stations, we used similar data of flow duration curve and vegetation cover for different reaches in the same river, regardless of the distance among them (e.g., reaches 33, 34 and 35 in figure 3.7). Although we did not identify tributaries from aerial photos, the presence of small streams may lead to downstream alteration in the flow regime.

Analysis results are intrinsically related to the additionally hypothesis made in the proposed procedure. Conversely to t_d for $\overline{\alpha}_d$, we cannot involved t_g as a temporal scale for the growth rate $\overline{\alpha}_g$, as we fixed its value ($t_g \approx$365d). It follows that, according to the flow regime of each particular river, this approximation may lead to errors when, for instance, the bio-morphological equilibrium requires longer time to be achieved. Morphodynamic processes (e.g., width adjustment, bank erosion, bar migration) can delay the achievement of such equilibrium and, in this case, a longer time scale t_g should be taken into account. This should also be considered when dealing with important alterations in the flow regime, both in relation to natural changes due to climate change (e.g., Stromberg et al., 2010; Rivaes et al., 2013) and human interventions due to flow regulation (e.g., Johnson, 1997) or dam removal (e.g., Shafroth et al., 2002), and in the vegetation cover, due to alien species colonisation (e.g., Stromberg et al., 2007) or artificial plantations (e.g., Perry et al., 2001). In this regards, the presence of outliers in figure 3.9 (Group 6) and in figure 3.10 (Group 1) can be explained by considering the main species composing the vegetation cover. Group 1 is mainly constituted by river reaches showing *Populus* species in the plant composition: poplars are known for its fast growing ($\overline{\alpha}_g$ in figure 3.10) and, accordingly, they were artificially introduced in riverine environments for timber production. Conversely, Group 6 is mainly constituted by reaches showing plants of the genre *Thuja*. Such plants are more typical of swamps and wetlands, rather than riverine habitats, and their low decay rate $\overline{\alpha}_d$ may be related to the rare occurrence of flow uprooting in such environments (Stewart, 2009).

3.5 Conclusions

In this chapter, we analysed the interactions between river morphodynamics and vegetation properties at the reach scale. We based our analysis on the one-dimensional

equations derived by Perona et al. (2014) for the river width where vegetation front is located, provided the existence of an ubiquitous pattern in rivers with convergent boundaries. We first proposed a procedure to calculate the biological parameters and hydrological timescales governing such equilibrium at the reach scale. Accordingly, we validated the proposed procedure against data from real rivers on a yearly time scale, accounting for the effective duration of flow removal, and concluded that vegetation front location is predictable and dependent on the vegetation species, thus providing guidance for future river restoration projects. Due to the defined planform configuration, we could point out the implicit interplays among plants species, river morphology and flow duration. As a result, we demonstrate the ability for rivers to select, by hydrodynamic-induced mortality, biomass (i.e., plant species) according to the flow regime (flood event return period and duration) of the river itself. Furthermore, our analysis shows the importance of accounting for vegetation dynamics and its influence on river properties, both in long-term simulations where flow conditions change in time according to time-scale depending on growth rate α_g and at the flood event scale, where vegetation density changes according to α_d: therefore, the choice of time-scale and time-step shall reflect not only hydraulic conditions but also vegetation properties

Chapter 4

Vegetation uprooting: a new model and its application

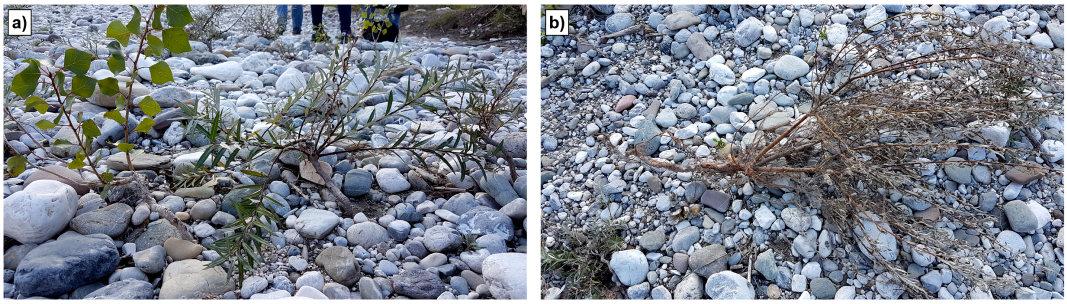

FIGURE 4.1: Survival outcomes after a flood event in the Tagliamento River. a) Seedlings of *Populus* on the left and *Salix* on the right survived to flood. The erosion on the bar, testified by the exposed roots, was not enough to uproot these seedlings; b) An uprooted plant of *Salix* with intact root. Photos taken near San Daniele del Friuli (IT).

This chapter explains the development of a new physic-based model to predict the critical conditions of flow and bed erosion leading to plant uprooting. Flume experiments and field measurements to validate the model are described as well.

This chapter has been published by the author in *Journal of Geophysical Research: Earth Surface*: **124**(4):1018-1034, doi:10.1029/2018JF004747 (Calvani et al., 2019a). Minor changes have been done for formatting purposes.

4.1 Introduction

The water channel and its adjacent areas form a complex environment interacting through almost regular flooding. This interaction takes place mainly in the riparian zone, defined as floodplains, banks, and all fluvial landforms below the bankfull elevation (Hupp and Osterkamp, 1996). Therefore, river evolution is not only governed by fluid dynamics and sediment processes (erosion, transport and deposition) but also driven by aquatic and terrestrial elements, especially riparian vegetation (Camporeale et al., 2007; Solari et al., 2016). In fact, vegetation has the capability of providing additional flow resistance thus reducing the actual shear stress on the bed; consequently, erosion might be reduced and sediment deposition could be promoted (Nepf, 2012b). Lastly, vegetation can decrease soil erodibility by providing additional soil tensile strength due to the presence of roots (Bankhead et al., 2017). As a result, riparian vegetation acts as a river system engineer, useful for river restoration projects (Gurnell, 2014). Therefore, it is essential to link the dynamic interactions between the fluvial and vegetative processes to understand the state and evolution of a fluvial environment (see Camporeale et al. (2013) for a review).

Among the various processes involved in the interaction between vegetation and hydromorphology, the mechanism of vegetation uprooting is still poorly understood. The existing threshold for conditions of uprooting are expressed either in the form of a modified Shields parameter (Bertoldi et al., 2014) or in terms of scour depth (van Oorschot et al., 2016). These criteria are oversimplified due to the fact that they do not consider the coupled action of both hydrodynamics and bed scour on the vegetation removal. Moreover, they generally underestimate the conditions required for uprooting; nevertheless, field campaigns after flooding events have shown that vegetation can be eradicated even following the development of a limited local scour around the stem (e.g., Tanaka and Yagisawa, 2009).

A major source of uncertainty is characterised by a poor understanding of root systems which present an extremely high variability (Pasquale et al., 2012). It is commonly recognised that riparian vegetation increases soil particle binding and reduces the soil erodibility through the action of roots. This is quite thoroughly studied and modeled for cohesive soils in hillsides and riverbanks (e.g., Pollen and Simon, 2005; Pollen, 2007; Burylo et al., 2012) whereas awareness of the influence and role of below-ground biomass on non-cohesive soil materials like riverbed sediment is scarce (e.g., Gyssels et al., 2005). An attempt at modeling root resistance was made by Ennos (1990) who proposed three failure mechanisms during uprooting: root breaking, depending on tensile breaking strength of root material, root pull-out, depending on the shear strength of the soil material, and soil-root ball failure, depending on the tensile strength of the soil. The effective resistance of the plant to uprooting is represented by the weakest mechanism of the three. The lack of knowledge concerning the effect of roots on vegetated bars in water channels was

highlighted by Edmaier et al. (2011). They hypothesised that vegetation uprooting in non-cohesive soils occurs as a consequence of two distinct mechanisms. The first mechanism, namely "Type I", takes place when the resultant of buoyancy and drag forces acting on the plant exceeds its anchoring ability: this leads to an almost instantaneous removal of the entire plant due to root breakage or extirpation from the soil. This mechanism is mainly relevant to very young vegetation, due to its relatively short and simple root architecture. For mature vegetation with a deeper and stronger root apparatus, a reduction in the resisting force is required for uprooting to occur. This reduction may be the result of local scour around the plant, causing the root to be partially exposed to the flow, thus decreasing its anchoring force. This process, namely "Type II" mechanism, differs from the previous one in the time delay needed for erosion to achieve the critical equilibrium between resisting and destabilising forces. Therefore, uprooting occurrence depends not only on the flow conditions but also on the factors controlling root resistance, which are species- and situ- dependent (Edmaier et al., 2011; Edmaier et al., 2014b). Bywater-Reyes et al. (2015) further differentiated the latter mechanism into "Type IIa" and "Type IIb", accounting for the differing sources of scour around the plant stem. In Type IIa, the scour is self-induced by the presence of the plant, which causes the formation of a horseshoe vortex upstream and relatively high erosion around the stem. The self-induced scour scales with the diameter of the seedling, similar to that which can be observed around bridge piers (Dargahi, 1990; Edmaier et al., 2011; Crouzy and Perona, 2012). Conversely, in Type IIb, the reduction in resistance is mainly due to erosion process acting on longer length scales (bar or reach length) or spatially varying sediment transport.

To quantify the resistance to uprooting of riparian seedlings, the Type II mechanism was investigated by Edmaier et al. (2015) in flume experiments with *Avena sativa*. In accordance with Perona et al. (2012a), they found that uprooting resistance is mainly dependent on root length. Kui et al. (2014) used cottonwood and tamarix seedlings to investigate feedbacks between flow and vegetation in a prototype scale meandering channel and found that 55% of the uprooted plants was located either at the edge of the sandbar or in areas subjected to high scour. Bywater-Reyes et al. (2015) focused on both the main uprooting mechanisms in field campaigns on the floodplains of three rivers in the USA. They measured the resistance of 1-5 years old Populus and Tamarix seedlings to uprooting, by simulating the drag force exerted by flow during floods using lateral pull tests, as proposed by Stone et al. (2013) and previously used by Mickovski et al. (2005) and Burylo et al. (2009). They involved different conditions of imposed scour around plants and compared measurements to predicted forces for the occurrence of Type I and Type II uprooting mechanisms. Field pull-out tests were recently carried out by Bankhead et al. (2017) to measure the resisting force of three different species of vegetation (*Phragmites australis*, cottonwood *Populus deltoides* and reed canarygrass *Phalaris arundinacea*) on vegetated islands in the Platte River. Perona and Crouzy (2018) proposed a formulation for the

occurrence of Type II mechanism. Uprooting occurs when superposition of the deterministic erosion and a random process noise reaches a critical erosion length. The model was applied to dataset of Edmaier et al. (2015) with good agreement. However, the critical erosion length remains undetermined for different plants.

As far as we know, from literature review, there was very little experimentation on vegetation uprooting under controlled laboratory conditions (Edmaier et al., 2014b). Moreover, riparian species typical of European rivers (e.g., poplars, willows, alders) was not considered in these experiments. For bridging this gap, we propose a model for predicting the uprooting of flexible juvenile seedlings by combining the destabilising actions of both bed scour and flow pull-out. This type of vegetation can be commonly found on alluvial bars (such as point and lateral bars). Hortobágyi et al. (2018) demonstrated that the area of establishment of pioneer vegetation, such as the Salicaceae species (e.g., *Salix purpurea*), is the zone where the most exposed location of alluvial bars meets with the main channel. Such plants actively interact with morphological processes giving rise to sediment accumulation and thus driving the evolution of river bars (Corenblit et al., 2007).

Our approach is a combination of laboratory flume experiments, field measurements and numerical simulations. We first introduced a conceptual model for the mechanism of root pull-out in flexible juvenile seedlings and a novel physics-based balance equation to predict the threshold conditions for Type I and Type II uprooting. To properly quantify the forces acting on seedlings under conditions of controlled erosion of the bed, we carried out laboratory experiments regarding the uprooting process of two different species of vegetation, *Avena sativa* and *Salix purpurea*. The ensuing results from this experiment were used to validate the conceptual model. In addition, we conducted field campaigns to measure root resistance along the Ombrone Pistoiese River on a gravel bar: here a flooding event which occurred in November 2016, resulted in the uprooting of established *Salix purpurea* pioneer vegetation. A 2D hydraulic model reproducing the effects of that flooding event was implemented. Based on the simulated bed shear stresses, we applied the conceptual model and we compared the prediction of vegetation uprooting with field observations.

4.2 Conceptual model for flexible vegetation uprooting by flow

We derive a conceptual model valid for flexible juvenile seedlings, capable of mathematically evaluating the critical conditions for which uprooting due to pull-out mechanism occurs. The model can be applied to cohesive soils as well, although

riverbeds are typically constituted by non-cohesive sediments. In fluvial environments, plants are subject both to destabilising and resisting forces: the former includes flow pull-out F_D, bed erosion L_e and buoyancy B, and the latter is the friction shear stress exerted between the root surface and the soil. We take into account the high flexibility of seedlings and hypothesise that during a flood juvenile plants are prone, parallel to the bed and aligned along the main flow direction (figure 4.2-b)). In this condition, pull-out force due to the flow is represented by the bed shear stress acting on the lateral surface of stem and leaves rather than the flow drag which instead becomes important for mature plants (e.g., Baptist et al., 2007; Sand-Jensen, 2008; Schnauder and Moggridge, 2009). Additionally, scouring process exposes the tops of the roots to flow, thus reducing the anchoring resistance (Edmaier et al., 2011). Exposed roots have less bending stiffness (Coutts, 1983) and increase the length of the plant and the bending moment exerted by flow. As a result, plants easily bend over in the flow (figure 4.2-c)). The resisting force is given by the resultant of the soil shear stresses acting upon the lateral surface of the below-ground remaining part (after bed erosion) of the root apparatus. In our model, vegetation roots are represented by vertical cylinders with a constant diameter (Ennos, 1990). For the soil shear stresses we use the general Mohr-Coulomb criterion for soil resistance, given by (simplified from Fredlund et al., 1978):

$$\tau_{soil} = c' + (\sigma_{soil} - u_w) \cdot \tan \phi' \tag{4.1}$$

where c' is the soil cohesion; u_w is the pore water pressure; ϕ' is the soil shear strength angle. In analogy with a frictionless pulley mechanism, the load due to bed

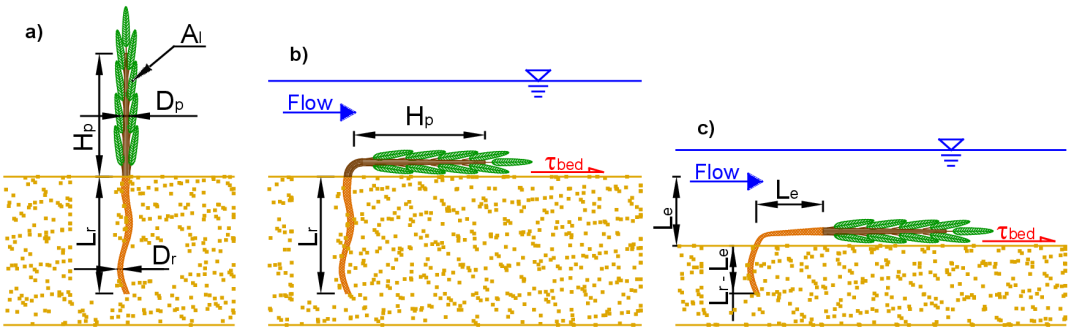

FIGURE 4.2: Outline of the conceptual model and main dimensions involved in the proposed equation for vegetation uprooting: a) initial state (i.e., t=0) without reconfiguration during a dry period; b) plant reconfiguration when water starts flowing: if large enough, τ_{bed} can lead to Type I uprooting (removal without bed erosion); c) plant configuration at the time of removal, after bed erosion equal to L_e (Type II uprooting).

shear stress acting on the lateral surface of the above-ground part of the seedling is directly transferred to the below-ground part. Therefore, the force balance simply stipulates that the resisting force F_R equals the destabilising forces associated with flow pull-out F_D and buoyancy F_B, in other words:

$$F_R = F_D + F_B \tag{4.2}$$

with

$$F_R = \pi f \left(c' \sum_{i=1}^{N_R} \left(D_{r,i} \left(L_{r,i} - L_e \right) \right) + \left(\gamma_{sat} - \gamma_w \right) \sum_{i=1}^{N_R} \left(D_{r,i} \frac{\left(L_{r,i} - L_e \right)^2}{2} \right) \tan \phi' \right) \tag{4.3}$$

$$F_D = \tau_{bed} \pi \left(H_p D_p + \frac{A_l}{\pi} + L_e \sum_{i=1}^{N_R} D_{r,i} \right) \tag{4.4}$$

$$F_B = \left(\gamma_w - \gamma_v \right) \pi \left(\frac{H_p D_p^2}{4} + \sum_{i=1}^{N_T} \frac{L_{r,i} D_{r,i}^2}{4} + \frac{A_l \, t_l}{\pi} \right) \tag{4.5}$$

where γ_{sat}, γ_w and γ_v are the saturated soil, water and vegetation unit weight, respectively; N_R is the number of resisting roots; $D_{r,i}$ and $L_{r,i}$ are the diameter and length, respectively, of the i-th root; D_p and H_p are the diameter and height of the seedling; A_l is the foliage area, t_l is the average thickness of the leaves, τ_{bed} is the bed shear stress and f is the dimensionless soil-wood friction coefficient ranging from 0.7 to 0.9, according to Potyondy (1961) and Gray and Sotir (1996). The foliage area A_l is estimated through the LAI (*Leaf Area Index*) using data from the literature (Aberle and Järvelä, 2013). L_e here represents the critical bed erosion for which Type II uprooting occurs. We solve Eq. (4.2) for the critical bed erosion L_e, by substituting Eqs (4.3), (4.4) and (4.5) and imposing a constant diameter D_r for all the roots. Following mathematical calculations, we obtain a quadratic equation ($c_2 \, L_e^2 + c_1 \, L_e + c_0 = 0$) with the following coefficients:

$$c_2 = 1 \tag{4.6}$$

$$c_1 = -2 \left(\frac{1}{N_R} \sum_{i=1}^{N_R} L_{r,i} + \frac{\tau_{bed} + c'}{\left(\gamma_{sat} - \gamma_w \right) f \tan \phi'} \right) \tag{4.7}$$

$$c_0 = \frac{1}{N_R} \sum_{i=1}^{N_R} L_{r,i}^2 - 2 \, \frac{\tau_{bed} \left(\pi H_p D_p + A_l \right) + F_B}{\left(\gamma_{sat} - \gamma_w \right) \pi N_R D_r f \tan \phi'} + \frac{2c'}{\left(\gamma_{sat} - \gamma_w \right) f \tan \phi'} \frac{1}{N_R} \sum_{i=1}^{N_R} L_{r,i} \tag{4.8}$$

In the case of *Avena sativa* the total number of roots N_T is equal to 3, and N_R is assumed to be 1 as 2 of the 3 roots are superficial and thus do not contribute to the anchorage of the plant (Edmaier et al., 2014b). The model can be also applied for Type I uprooting (vegetation removal without riverbed erosion). In this case, Eq. (4.2) can be solved for τ_{bed} by neglecting terms containing L_e and matching N_R to N_T. The resultant formula reads as follows:

$$\tau_{bed}^I = \frac{\pi f D_r \left(2c' \sum_{i=1}^{N_T} L_{r,i} + \left(\gamma_{sat} - \gamma_w \right) \tan \phi' \sum_{i=1}^{N_T} L_{r,i}^2 \right) - 2B}{2 \left(\pi H_p D_p + A_l \right)} \tag{4.9}$$

where the superscript I stands for Type I uprooting.

4.3 Methods

Methods included flume experiments in the Hydraulics Laboratory of our Department, field surveys of topography, sediment and vegetation in the Ombrone Pistoiese River, and 2D numerical modelling.

4.3.1 Experimental activity

We performed flume experiments to test the proposed conceptual model. In particular, we reproduced vegetation uprooting driven by general bed erosion (Type IIb mechanism according to Bywater-Reyes et al. (2015)). We ran flume tests with juvenile *Avena sativa* and *Salix purpurea* seedlings; the former was selected in continuity with the previous work of Edmaier et al. (2015), while the latter can be typically observed on river bars (Hortobágyi et al., 2018), as in the case of the Ombrone Pistoiese River (figure 4.4-c)). We collected juvenile *Salix purpurea* seedlings from the Ombrone Pistoiese River bar described in section 4.3.2. Then, they were carefully relocated in plastic boxes and kept watered for 96-120 h to limit stress. This time period was sufficient for young *Salix purpurea* seedlings to grow new small root branches and recover from transplanting (Manners et al., 2015). Conversely, *Avena sativa* plants were grown directly from seeds, kept in wet cotton wool until sprouting. Afterwards, sprouted seeds were placed in plastic boxes with removable walls, filled with the same flume sediment and watered to saturation. We cultivated *Avena sativa* for 96-144 h. Plants were grown and cultivated outside the flume without using special lights in a room where temperature was maintained between 18 and 21°C to ensure uniform growth conditions (Edmaier et al., 2015).

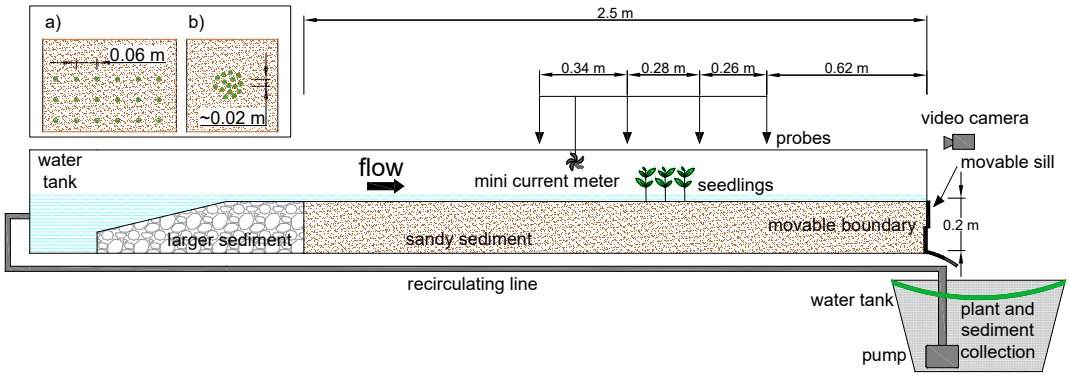

FIGURE 4.3: Experimental set-up of the flume. Probes indicate the positions where water and bed levels were continuously measured. The water tank was covered with a net for sediment and plant collection. In the inset panel, the two spatial arrangements involved in the experiments. a) Isolated plants with distance of 6 cm in both the directions; b) Non-Isolated patchy arrangement with distance of approximately 2 cm between plants.

The flume was 5 m long and 0.44 m wide. Here, we built a 2.5 m long mobile bed channel filled with poorly graded quartz sand ($D_{10} = 0.4$ mm, $D_{60} = 0.6$ mm,

coefficient of uniformity $C_u = 1.5$) with a mean diameter of $D_{50} = 0.57$ mm. The outlet cross-section was equipped with a movable bed sill. To obtain quasi-parallel bed erosion (Edmaier et al., 2015), bed sill was lowered at a sufficiently low speed ($\dot{\eta}$=2 mm min^{-1}) by manually turning a 2 mm pitch threaded rod half a turn every 30 seconds. The maximum lowering of the sill was 0.09 m. Flow discharge was maintained constant during each experiment, provided by a recirculating pump (maximum flow discharge: 14 l s^{-1}) and regulated by a control valve. In each experiment, we measured flow discharge using an electronic flow meter placed along the pump pipe and water surface elevation by means of 4 ultrasonic probes (USs) Honeywell series 943-F4V-2D-1C0-330E, two located upstream and two downstream of the vegetated area. In the same cross sections, we continuously measured bed levels. A Canon SX600HS camera located above the flume recorded the entire experiment and helped to identify the time at uprooting of each seedling (see figure 4.3). The uprooted seedlings were collected at the flume outlet and then measured.

We placed vegetation in the flume using a procedure similar to Edmaier et al. (2015): the plastic boxes, in which we previously cultivated the plants, were carefully inserted into the downstream half of the working flume, employing a variety of spatial arrangements. We then removed the lateral walls of the boxes to allow for sediment transport and bed erosion. The bottom panels of the boxes were left inside the flume, as they were deeper than the maximum achievable erosion depth and could not affect the experiment running. For each vegetation species, we ran the experiments under four different flow discharges (7.4, 8.4, 9.6 and 10.5 l s^{-1}). Bed slope was set to 0.5%.

We investigated two planimetric arrangements of the vegetation, namely Isolated and Non-Isolated: we refer to plant isolation with regard to root interference but not to possible above-ground interactions (e.g., drag alteration or turbulence feeding (Nepf, 2012b)). Following the considerations of Edmaier et al. (2015) on soil surface affected by the presence of roots (a cone with 60° aperture), we considered plants to be isolated against flow removal when their underground soil volumes are not interfering at the time of uprooting. The condition for which this happens is governed by the following relation:

$$\Delta s > 2\,\frac{L_r - L_e}{\sqrt{3}} \tag{4.10}$$

where Δs is the minimum spatial distance between the uprooted seedling and the surrounding plants. Therefore, in the Non-Isolated configuration 15 seedlings were placed at a distance Δs of approximately 0.02 m in both the streamwise and the transversal directions to mimic a vegetated patch (figure 4.3-b)). We investigated the Isolated configuration by involving three different spatial arrangements, 1 row of 6 plants, 3 rows of 6 aligned plants, and 3 rows of 6 staggered plants (see Table 4.1). In

these arrangements, distance Δs between plants is 0.06 m in both the directions (figure 4.3-a)). During the experiment, we intercepted uprooted plants at the end of the flume by a collecting net, carefully recovered and organised them according to the time of uprooting. We switched the pump off and stopped running the experiment as soon as either all the seedlings were uprooted or the maximum lowering of the downstream wall was reached. We then measured the height and diameter of both the stem and root for each of the plants involved.

TABLE 4.1: Experimental setup with species, spatial arrangements and data for each run. $\overline{a}$ is the average stem area per unit volume, Q is the flow discharge, Y is the measured flow depth, Re and F_r are the computed Reynolds and Froude numbers, respectively.

Vegetation species	Spatial arrangement	$\overline{a}$ [m^{-1}]	Q [$l\,s^{-1}$]	Y [mm]	Re [-]	Fr [-]
Avena sativa Isolated	1 row of 6 plants	0.361	7.4	39.7	16793	0.68
			8.4	40.5	19035	0.75
			9.6	42.5	21845	0.80
			10.5	43.0	23865	0.85
	3 rows of 6 aligned plants	0.361	7.4	35.0	16800	0.82
			8.4	37.7	19076	0.83
			9.6	39.5	21804	0.89
			10.5	43.3	23858	0.85
Avena sativa Non-Isolated	patch	3.25	7.4	34.4	16818	0.84
			8.4	42.8	19091	0.70
			9.6	44.7	21818	0.74
			10.5	47.1	23864	0.75
Salix purpurea Isolated	1 row of 6 plants	0.278	7.4	38.6	16829	0.71
			8.4	40.9	19304	0.74
			9.6	45.3	21835	0.72
			10.5	47.2	23883	0.74
	3 rows of 6 aligned plants	0.278	7.4	37.2	16814	0.75
			8.4	39.1	19315	0.79
			9.6	44.4	21800	0.74
			10.5	48.3	23860	0.72
	3 rows of 6 staggered plants	0.278	7.4	37.5	16800	0.74
			8.4	42.9	19562	0.69
			9.6	45.6	21842	0.72
			10.5	48.6	23863	0.71
Salix purpurea Non-Isolated	patch	2.50	7.4	41.4	16808	0.64
			8.4	45.8	19328	0.62
			9.6	44.1	21830	0.75
			10.5	49.7	23856	0.69

4.3.2 Case Study: the Ombrone Pistoiese River

The Ombrone Pistoiese River is a tributary of the Arno River and is located in the centre of Italy. The field site is a 300 m long reach located close to the village of Gello, north of the city of Pistoia, and near the junction with the Vincio Creek (figure

4.4-a,b)). The main channel is on average 15.5 m wide and the bed slope is 0.008. We selected this site due to the active dynamics in this reach of the Ombrone Pistoiese River: in the last 15 years the main channel trajectory shifted from the left to the right side of the floodplain due to the combined effects of both natural (e.g., flood events) and human impacts (i.e the construction of a transversal weir upstream of the field site). The active dynamics promoted the vegetative colonisation on a bare gravel deposit; for this reason, in the floodplain we found juvenile species but not mature trees. This area represents a natural habitat for the establishment of Salicaceae species, and an excellent position from which we observed the removal of *Salix purpurea* seedlings during a flood event (figure 4.4-c,d)).

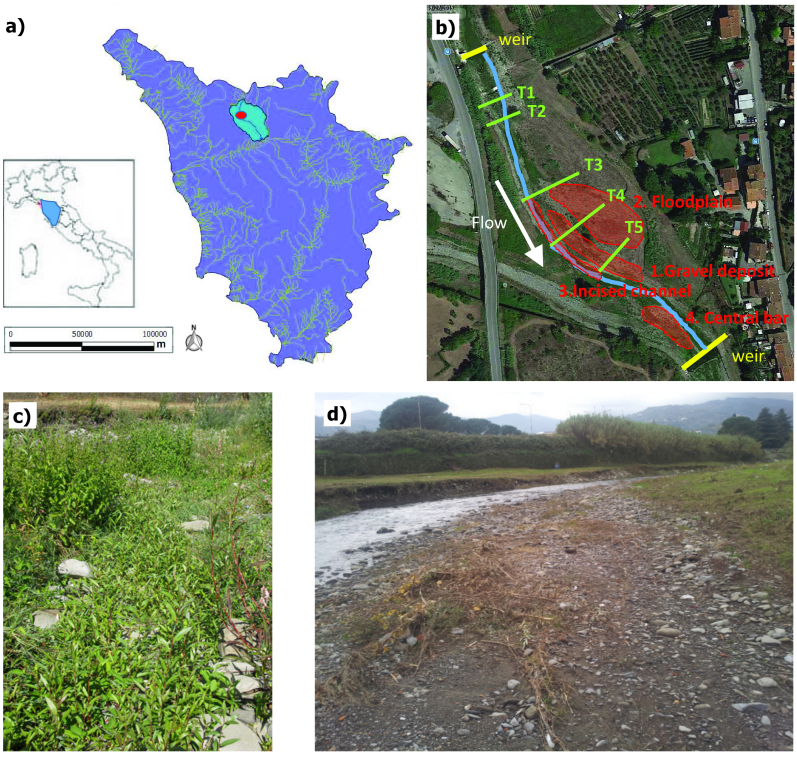

FIGURE 4.4: Location of the study site, the Ombrone Pistoiese River near Gello (IT) and upstream view of the vegetated bar: a) View of Ombrone Pistoiese basin; b) Location of the surveyed areas for bed sediment and transects for monitoring vegetation; c) Lively *Salix purpurea* juvenile seedlings during the field campaign on September 2016. d) Almost bare riverbed soil due to vegetation uprooting after the flood event. Although damaged, elder plants on the left survived to the flood event whereas vegetation in the remaining part was completely eradicated.

Field activities included sediment sampling and topographic surveys done in September and November of 2016, as well as density and distribution mapping of *Salix purpurea* and measurements of root resistance to uprooting that was done in September. We characterised the bed sediment on the surface layer in four distinct areas (figure 4.4-b)): 1) a gravel deposit on the left side of the incised channel, partially vegetated; 2) a floodplain surface to the left of the site characterised by higher bed levels; 3) the incised channel and 4) a central bar, close to the junction with the tributary coming from the right. The floodplain exhibits smaller values of sediment size ($D_{50} = 10.5$ mm) compared to the other samplings which have $D_{50} = 41.2$ mm

(gravel deposit), $D_{50} = 50.9$ mm (incised channel) and $D_{50} = 45.3$ mm (central bar).

Topographic surveys were conducted in the main channel and on the floodplain. Bed elevation was measured using RTK GPS instrumentation (LEICA RX1250 Smart Rover); in the transversal (streamwise) direction of the main channel, the spacing of survey points was approximately 1 m (1.5 m), whereas in the floodplain region, the interval between survey points was increased to 3 m in both directions. Accuracy was 0.01 m in the plane directions and 0.02 m in the vertical one. We found spacing and accuracy suitable for measuring the principal characteristics and changes in the bed elevation. The GPS survey was first conducted in September 2016. A second run of measurements was repeated after the flooding event of November 2016. During the first topographic survey, we also monitored riparian vegetation by characterising density, size and distribution of the *Salix purpurea* seedlings along five transversal transects (figure 4.4-b)). We identified a 1 m wide cell along the transect sections and measured the number of plants, stem size and height every 0.5 m. Collected data were summed up as a single measurement at the center of each measuring cell. The vegetation survey was repeated after the November flood.

We also carried out field measurements of root resistance to uprooting of approximately 1-3 years old *Salix purpurea* pioneer plants, by following the approach previously adopted by Bywater-Reyes et al. (2015) and Bankhead et al. (2017). A rope was clamped to the base of the plant and slowly pulled in the downstream direction using a hand winch until uprooting. The hand winch was attached at a height of 0.5 m to a fence post placed 2 m downstream of the plant. Thus, the traction force was oriented at about 14° from horizontal, consistent with measurements of the pronation of juvenile vegetation during high flows (Manners et al., 2015). Before running each pull-out test, we watered the sediment around the plant to simulate the wet conditions of flooding. Applied force to the plant was continuously measured by a load cell (AEP transducers type TS, max load: 200 Kg) installed along the rope and data were simultaneously registered using a datalogger (AEP Star datalogger). We performed 94 validated tests: 53 plants failed due to root-soil interface sliding and for them we measured root length and diameter, 41 plants failed due to root breakage and for them we could measure root diameter only.

4.4 Modelling vegetation uprooting

4.4.1 Experimental results

During the initial phase of each experiment we observed vegetation bending downstream under the action of the flow (figure 4.5-b)). When we started lowering the downstream bed sill, bed erosion and root exposure promoted plant bending, until

a final horizontal equilibrium configuration was achieved (figure 4.5-c)). After some minutes, we observed the increasing exposure of the root apparatus (figure 4.5-d)), until the destabilising forces (buoyancy and bed shear stress) reached a critical value such that uprooting took place and plants were removed and dragged downstream. Each experiment lasted a maximum of 1 hour, due to the fixed limit in lowering the bed sill. According to the ratio between stem diameter and mean grain size adopted

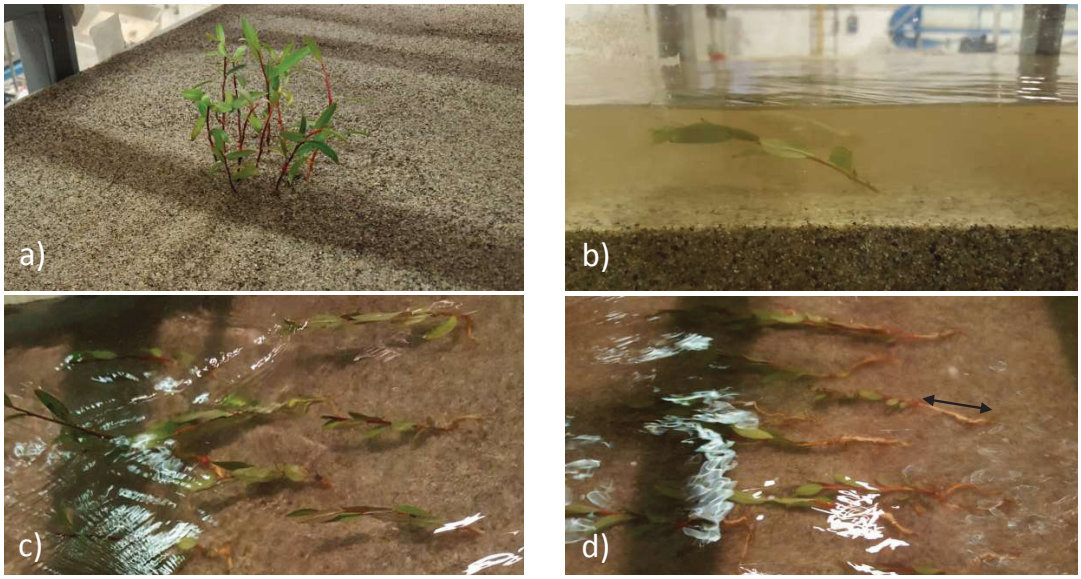

FIGURE 4.5: Description of the physical processes observed during the flume experiments, flow is from right to left: a) View of a *Salix purpurea* patch after positioning inside the flume; b) Bending process of *Salicaceae* seedlings at the beginning of one experiment; c) Salix seedlings lying on the sand bed; d) Exposed roots of Salix seedlings before uprooting.

in the experiments ($D_p/D_{50} \approx 1$), self-induced scour around stems can be legitimately neglected (Melville and Sutherland, 1988). Therefore, the reduction in root anchoring force was mainly driven by the generalised bed erosion induced by lowering the downstream bed sill (Type IIb uprooting mechanism). The hypothesis of parallel bed erosion was satisfied in most of the experiments; this was confirmed using data of erosion depth in the four monitored cross sections. However, bedforms (ripples) developed in the experiments with 9.6 l s^{-1} and 10.5 l s^{-1}. Vegetation-induced bedforms were observed also by Diehl et al. (2017) in flume experiments under unsteady flow conditions. In our case, they were sometimes so high ($\approx$ 7 mm) to alternately bury and uncover the plants, particularly the smallest seedlings of *Avena sativa*. In these cases, we were unable to validate the initial hypothesis of parallel bed erosion so we removed these data from the analysis.

The capability of our model in predicting uprooting conditions is illustrated in figure 4.6 where we plotted the measured critical erosion depth against the estimated one for all the uprooted plants. The comparison is given for the two species

of vegetation (*Avena sativa* and *Salix purpurea*) according to the differing spatial distances between the plants (Isolated and Non-Isolated configurations). The comparison shows positive correspondence in the cases of Isolated plants whereas the prediction regarding the Non-Isolated cases is less accurate. The level of agreement is acceptable for the experiments with Isolated *Avena sativa* in which the error is contained within 30% (dashed lines in figure 4.6). For most of the plants, the error is well below the 20% ($R^2 = 0.68$), a value we consider acceptable when coping with the randomness of nature (Tron et al., 2015). On the contrary, the comparison shows less agreement ($R^2 = 0.31$) for the Non-Isolated *Avena sativa*. We find the same trend in the experiments with *Salix purpurea* seedlings: the Isolated case shows a higher agreement ($R^2 = 0.51$) than the Non-Isolated one ($R^2 = 0.36$). However, if we include the uprooted plants with vegetation-induced bedforms, the correlation decreases to $R^2 = 0.35$ for the Isolated and to $R^2 = 0.22$ for the Non-Isolated plants.

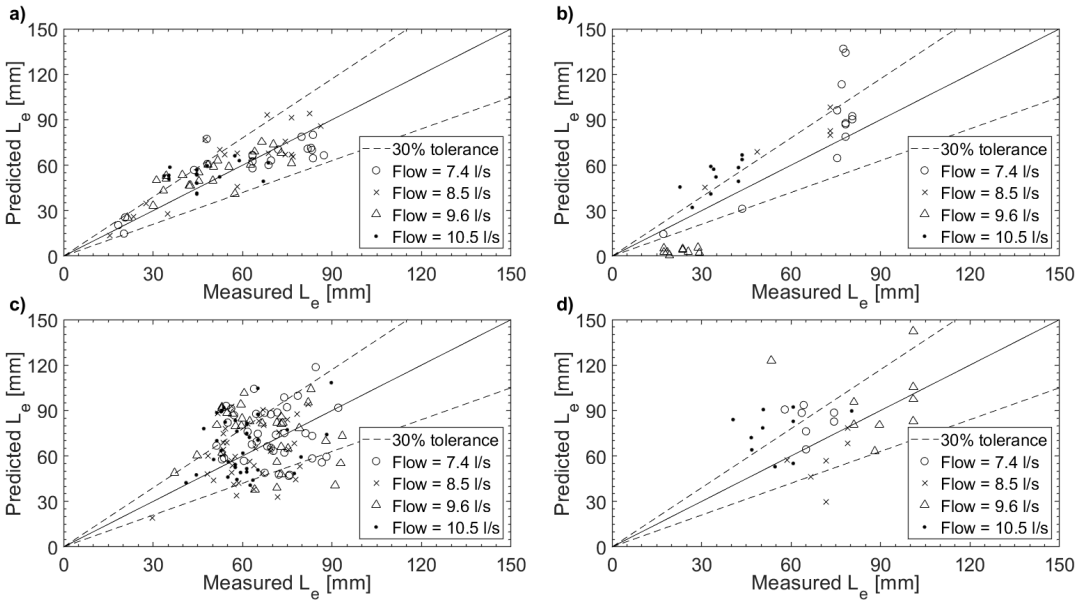

FIGURE 4.6: Comparison between predicted and measured bed erosion at the time of uprooting for *Avena sativa* and *Salix purpurea* seedlings in the case of *Isolated* and *Non − Isolated* plants: a) *Avena sativa* Isolated ($R^2 = 0.68$); b) *Avena sativa* Non-Isolated ($R^2 = 0.31$); c) *Salix purpurea* Isolated ($R^2 = 0.51$); d) *Salix purpurea* Non-Isolated ($R^2 = 0.36$). Dashed black lines delimit a 30% tolerance area around the perfect agreement continuous black line.

4.4.2 Field surveys

The comparison between the topographic surveys confirms that during the November flood the river bed remained unaltered except for a confined region near the right bank. Figure 4.7 shows the cross-sections along the five transects we monitored before (dashed black line) and after (continuous black line) the flood event. Even though some deposition and erosion patterns are shown, the changes are mainly limited to few centimetres, comparable to the accuracy of the GPS instrumentation. In the same graph (figure 4.7), the results of the monitoring activity on the presence

of vegetation (i.e., *Salix purpurea*) are expressed in terms of dimensionless vegetation density (sum of the frontal stem area per unit surface area). Vegetation densities are shown before (wide light-grey bars) and after (narrow dark-grey bars) the flood event. In fact, we verified that most of the young seedlings were uprooted by the flow, whereas the more established bushes and trees were not removed and survived (narrow dark-grey bars).

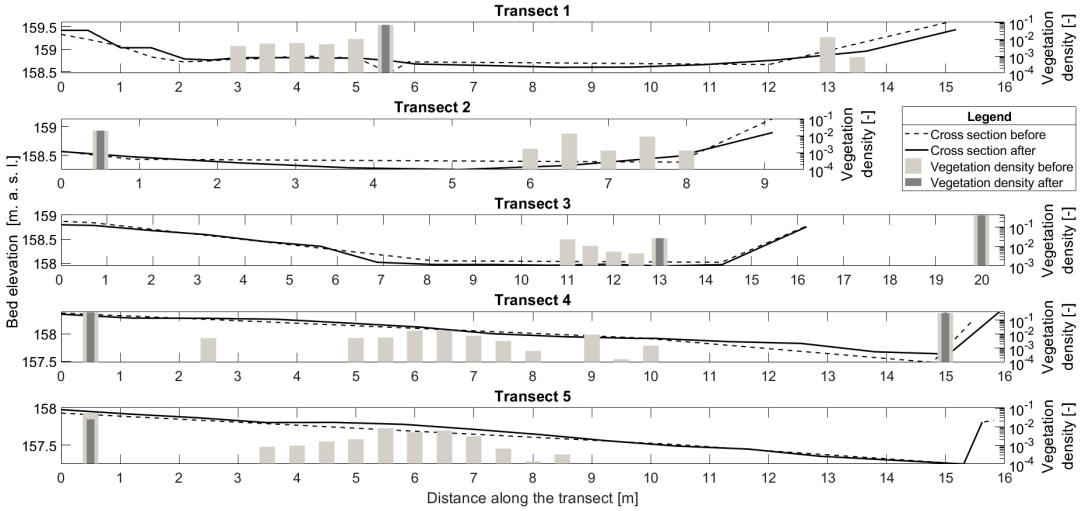

FIGURE 4.7: A summary of field survey measurements along five transects on the Ombrone Pistoiese River. Dashed black lines are the cross sections measured during the first GPS survey (27-28/10/2016). Continuous black lines are the cross sections measured during the GPS survey after the flood (27/11/2016). Columns show dimensionless vegetation density (sum of frontal stem area per unit area) along the transects: light grey for the vegetation density measured during the survey before the flood, dark grey for the survived vegetation measured after the flood event. Most of vegetation was completely removed by flood event.

During the field pull-out tests, plants experienced different failure mechanisms (either breakage or sliding), so plants with similar growth stage could require different force to be uprooted (figure 4.8-b)). According to the different failure mechanisms, we divided pull-out tests into two series: the first referring to tests with intact roots (sliding failure), the latter to those broken. For each series, we found that the maximum measured force scales with the plant stem area, i.e., the product between seedlings height and diameter. Unlike Bywater-Reyes et al. (2015) and Bankhead et al. (2017), we used the plant stem area due to its measuring simplicity and quickness. Additionally, neither advanced technologies nor computations are required, thus allowing for time and cost saving in extensive field campaigns. Moreover, total frontal area (stem area plus foliage cover) remains a function of species and growth conditions, and, as such, can be later considered using the Leaf Area Index. Figure 4.8-b) show that plants uprooted due to breakage have a resistance generally higher than those removed by sliding. For the two different failure mechanisms, we found the following correlations for uprooting resistance, valid for the ranges of stem area in which we uprooted plants (1 - 30 cm^2 for the sliding mechanism and 1-80 cm^2 for the breakage).

$$F_R^b = 100133\, H_p\, D_p + 19.05 \quad (R^2 = 0.67) \tag{4.11}$$

$$F_R^s = 81670\ H_p\ D_p - 6.33 \quad (R^2 = 0.62) \tag{4.12}$$

where forces are expressed in [N] and plant height H_p and diameter D_p in [m].

Figure 4.8-c–f) shows the different root apparatus of four uprooted *Salix purpurea* plants. In spite of the comparable depths, one can notice the different shapes of the four main roots. Due to the proximity of the plants, causing comparable conditions of water, light and nutrient availability, the main driving tropism is probably given by the presence of big gravel stones under the surface driving the root growth away from vertical direction (thigmotropism) (Gregory, 2008). Uprooted seedlings

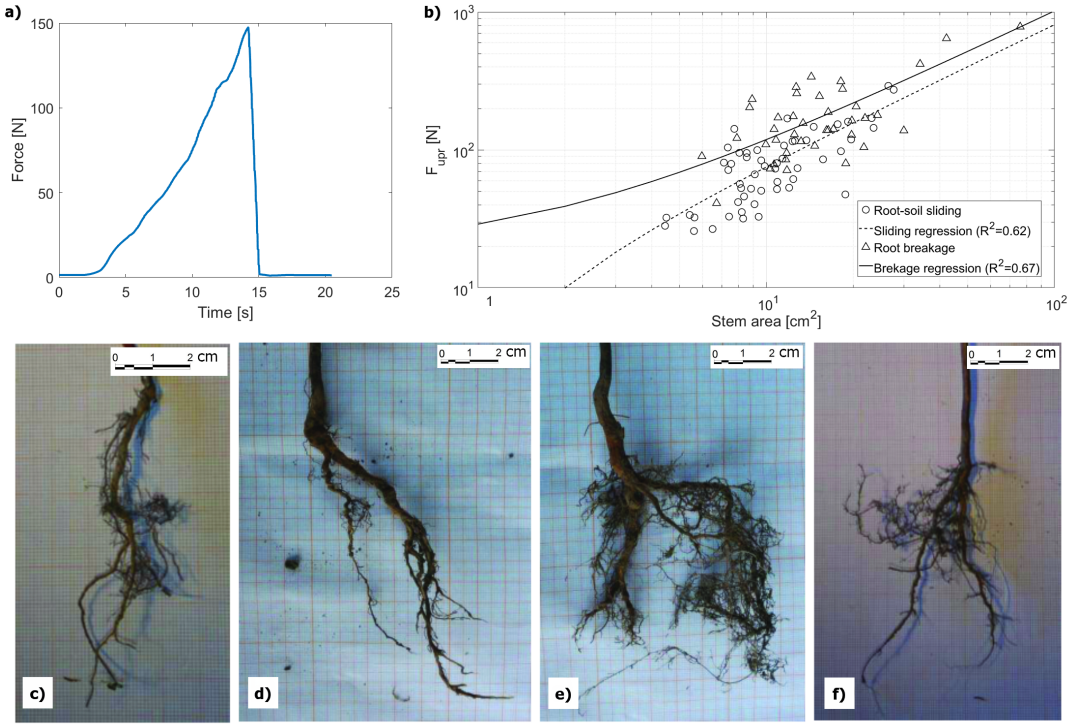

FIGURE 4.8: Field pull-out tests and plant characteristics. a) Diagram of force measured during a typical pull-out test. We considered the maximum force as the force needed for plant removal. The characteristics of the test were: stem height = 36.5 cm, stem diameter = 4 mm, main root length = 17.8 cm, root diameter = 5 mm, maximum force= 147.4 N; b) Regression relationships for maximum uprooting force measured in field tests for the two uprooting mechanisms: root-soil sliding (53 plants) and root breakage (41 plants). Regression lines and correlation coefficients are shown; c-f) View of uprooted *Salix purpurea* plants. The main variables of the tests are: c) L_r = 11.9 cm, F = 25.9 N; d) L_r = 17.8 cm, F = 147.4 N; e) L_r = 19 cm, F = 86.6 N; f) L_r = 11.6 cm, F = 73.38 N.

of *Salix purpurea* were further employed to derive relationships between the emergent part and below-ground root apparatus. Particularly, data analysis on uprooting tests was mainly focused on inferring root length and diameter as a function of the seedling stem area. We found the following regression relationships:

$$L_r = 49.7\ H_p\ D_p + 0.105 \quad (R^2 = 0.35) \tag{4.13}$$

$$D_r = 2.24\ H_p\ D_p + 0.00223 \quad (R^2 = 0.69) \tag{4.14}$$

where all the terms are expressed in [m]. For plants outside the presented range of

stem area, a correlation for root resistance to uprooting based on field measurements must be provided. Indeed, elder and more mature plants, with stem area greater than 100 cm^2 are likely to exhibit a divergent trend. Although the specific range of application, we provide these empirical relationships as we used them to infer uprooting conditions for the vegetation in the field site using the proposed model.

4.4.3 Hydraulic simulation

A 2D depth-averaged numerical model was implemented with the aim of reproducing the flood event of November 2016 and validating our model of uprooting with data from real case vegetation removal caused by high flows. We used the numerical tool BASEMENT v2.7.0 (Basic Simulation Environment) to calculate water depth, depth-averaged flow velocities and bed shear stresses (Vetsch et al., 2016). The tool does not explicitly take into account vegetation for the drag, although it was proved to work in numerical simulations involving vegetation using the Manning's approach (e.g., Bertoldi et al., 2014; Caponi and Siviglia, 2018). The unstructured grid was created using the tool BASEmesh. The maximum cell size was 1 m^2 in the main channel region and 5 m^2 in the floodplains, for a total of more than 11000 triangular cells in the whole model domain. Bed levels were interpolated using the GPS measurements taken before the flood event. A hydrograph of the event was registered at the Pontelungo measuring station located 4.5 km downstream of the study reach (data available from http://cfr.toscana.it). Due to the presence of small tributaries, we adjusted the measured flow discharges following the approach of Dunne and Leopold (1978) and Pazzaglia et al. (1998), according to the relation $Q_i = Q_{tot} \left(A_i / A_{tot}\right)^{0.6}$, where Q_i and A_i are respectively the flow discharge and the catchment area of the i-*th* river, Q_{tot} and A_{tot} are the measured flow discharge and the catchment area at the cross section of the measuring station. We obtained a peak flow discharge equal to 38.60 $m^3\ s^{-1}$. We adopted different Manning's coefficients for the different regions of the domain (main channel, lateral banks and floodplain, gravel deposit, central bar and concrete weirs), according to the mean grain size of bed material and the presence and type of vegetation. We calibrated the model according to the high-water marks observed in the field after the flood. We carried out the numerical simulation using fixed bed conditions: overall measured bed changes were very limited being in the order of few centimetres, although local erosion was observed on the right bank, just downstream of the lateral deposit (see Transects 3, 4 and 5 in figure 4.7).

We compared the calculated bed shear stress to the threshold for incipient motion of the D_{90} of the grain size distribution. To support the occurrence of sediment transport during the flood event, we considered the D_{90} in the dimensionless critical Shields stress τ^*_{cr} instead of the common D_{50} (e.g., Wilcock and Southard, 1988; Chiew and Parker, 1994). Figure 4.9 illustrates the distribution of the ratio between

the maximum Shields number and its critical value for the onset of sediment motion. Hence, we stated that the gravel surface layer was indeed mobilised by the

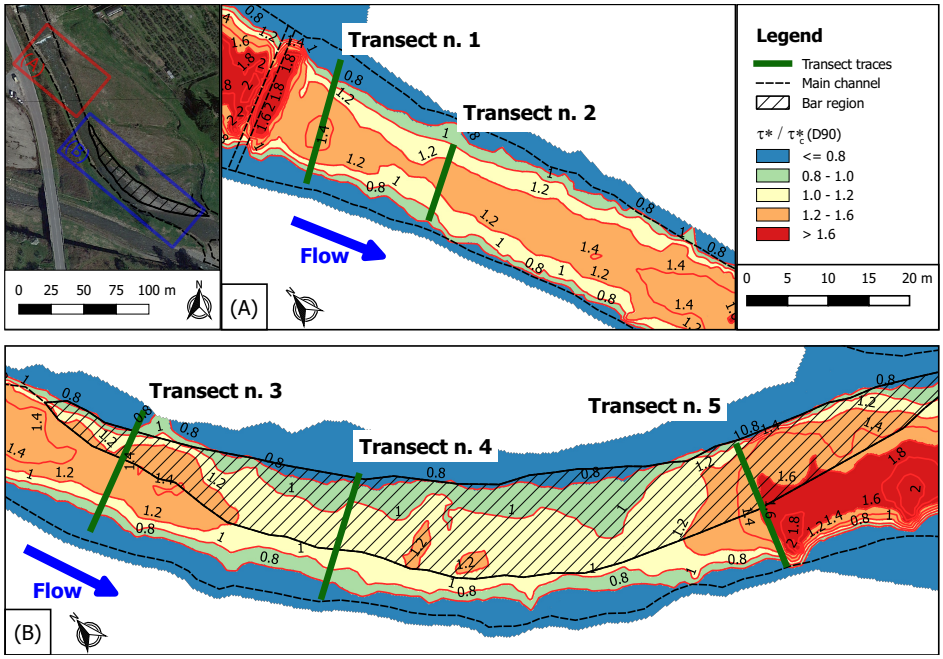

FIGURE 4.9: Dimensionless bed shear stress distribution (ratio between $\tau*$ and $\tau*_{cr}$ for the D_{90}) as a result of the numerical simulation. The figure confirms sediment transport took place in the main channel as well as on the vegetated bar (highlighted by dashed filling).

flow during the flood event: we assumed the thickness of the mobilised layer of the same order of the D_{90} of the surface-layer sediment (i.e., $2\,D_{90} = 0.214$m) (Parker, 1990). We hypothesised that mobilised layer by sediment transport reduced the anchoring force of plants, leading to Type IIb uprooting, similarly to what observed in the flume experiments under general bed erosion conditions. Indeed, moving sediments do not contribute to the increase soil resistance as calculated by Eq. (4.1) (Fredlund et al., 1978). Under this hypothesis, vegetation was subjected to similar conditions for root exposure during the flood. In order to analyse vegetation uprooting, we used the empirical relationships (i.e., Eqs (4.13) and (4.14)) to predict root length L_r and diameter D_r from the measured stem area of the vegetation along the surveyed transects. With all these ingredients and bed shear stresses from numerical simulation, we calculated the erosion depth L_e required for Type II uprooting for the monitored plants. Figure 4.10 shows the comparison between the calculated L_e and the thickness of the mobilised surface layer. Young seedlings characterised by small stem area (left part of the figure) are characterised by L_e well below the thickness of the mobilised layer: these plants were in fact removed by the flood. On the contrary, the more resistant bushes of *Salix purpurea*, characterised by higher values of stem area, showed higher values of L_e: most of them survived to the flood event (see figure 4.7 for a comparison between before and after the flood event). As an example, we calculated critical erosion depths of 0.56 m and 0.82 m for the plants shown in figure 4.4-d). These values are higher than the thickness of the mobilised

layer (0.214m) and, indeed, these plants survived to the flood event. Overall, the prediction error (i.e., number of mistaken predictions per total number of monitored plants) is below 3%.

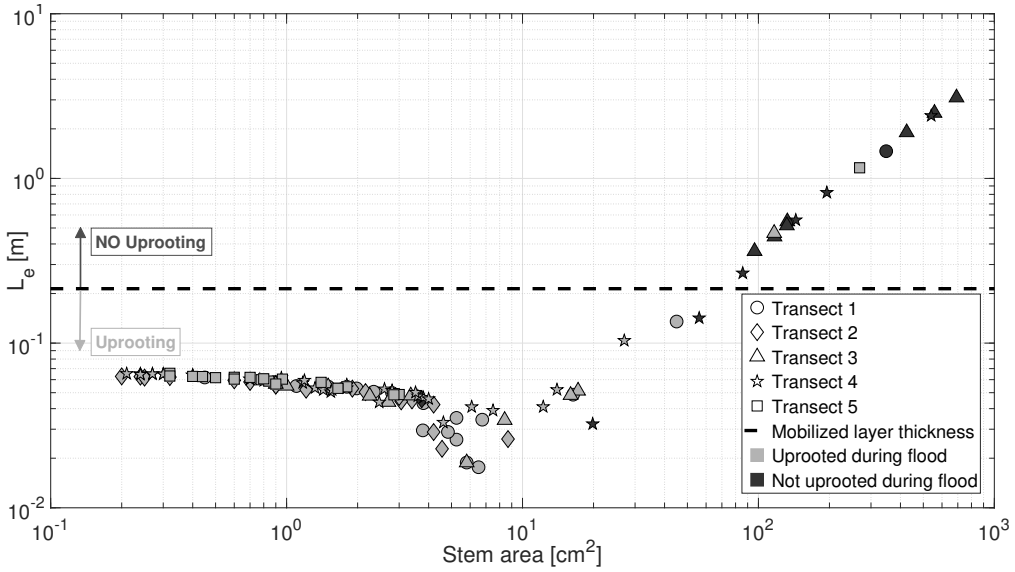

FIGURE 4.10: Comparison between predicted and monitored vegetation uprooting along the five surveyed transects and dimensionless analysis of type of uprooting (Type I versus Type II). Critical erosion depth predicted by the model for monitored vegetation and comparison to the mobilised layer thickness (light-grey symbols for uprooted seedlings, dark-grey for survived plants).

Figure 4.11-a) shows the comparison between the required force to uproot monitored *Salix purpurea* seedlings in the field and the hydraulic force established during a flood. We calculate the required force by multiplying τ_{bed}^{I} from Eq. (4.9) by the total plant surface (stem area plus foliage area). Eq. (4.12) provides the force needed for uprooting plants. As a result, ratio between forces is well above the unity for all the monitored seedlings. Similarly, figure 4.11-b) shows the comparison between bed shear stress for Type I uprooting (Eq. (4.9)) and the threshold for the incipient motion of sediment. The ratio is far greater than one for all the surveyed plants along the transects. Our analysis demonstrated that a mere destabilising force due to bed shear stress is not enough to uproot plants, even the very young seedlings (Bywater-Reyes et al., 2015). Additionally, we found vegetation uprooting time-scale longer than sediment mobilisation and bed erosion processes. Again, this supports the thesis of Type I uprooting unlikely to occur. Therefore, flow uprooting and plant survival depends on two time scales: one associated with the biological growth rate of the vegetation and the other being the frequency and magnitude of flooding events.

4.5 Discussion

We next explore how interactions between plants (Isolated vs. Non-Isolated) influence the uprooting process. Moreover, the experimental results are compared with the very recent stochastic model by Perona and Crouzy (2018).

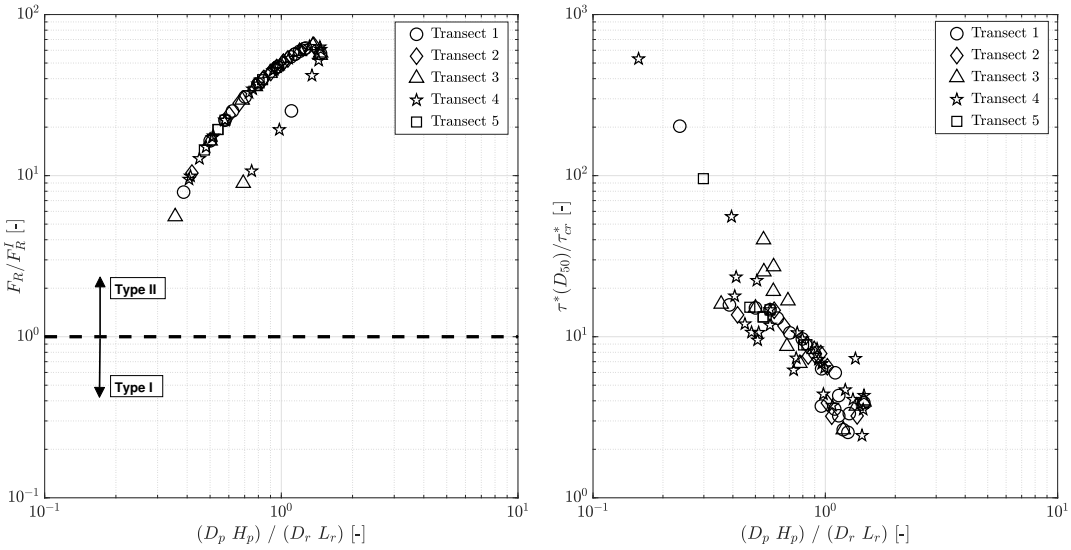

FIGURE 4.11: Dimensionless analysis of type of uprooting (Type I versus Type II) for the monitored vegetation. a) Ratio between removing force required for uprooting and the resultant of bed shear stress against stem-to-root area ratio. The dashed line represents the threshold between types I and II of uprooting; b) Ratio of bed shear stresses between Type I uprooting (Eq. (4.9)) and the threshold for sediment motion against stem-to-root area ratio.

The present study investigates vegetation removal due to flow and bed erosion (Type II uprooting) by flume experiments and field measurements. Critical bed scour is mainly driven by generalised (Type IIb) rather than local (Type IIa) degradation, both in the experiments (stem-to-grain ratio ≈ 1) and in the field (stem-to-grain ratio < 0.5) (Melville and Sutherland, 1988). With these values, self-induced scour is either hampered (in the flume experiments with Isolated plants) or limited to some centimetres (in the field). For similar values of stem-to-grain ratio, Bywater-Reyes et al. (2015) concluded that Type IIa can be important for juvenile seedlings (<1 year), although they did not measure uprooting resistance of such young plants. In the light of our experimental results, we found out that Type IIa is negligible even for young seedlings in the Isolated configuration. Conversely, the presence of self-induced scour can be relevant in the patchy arrangement (Non-Isolated): as a matter of fact, in this configuration the scour around stem is mainly driven by the patch size-to-grain ratio (Yager and Schmeeckle, 2013; Diehl et al., 2017). Additionally, when plants are Non-Isolated, interactions among root systems become relevant, as illustrated by the scarce correlation between predicted and measured erosion depth L_e at the time of uprooting (figure 4.6-b,d)).

Seedlings with different properties of stem height and main root length, for which we predicted different values of critical bed erosion L_e, were uprooted at the same time instead. Therefore, seedling proximity represents a cooperative mechanism of survival for juvenile plants (Grime, 2006), whereas it becomes a competitive factor when plants become older (Casper and Jackson, 1997). On the contrary, good agreement is found for the Isolated configuration: *Avena sativa* shows better agreement than *Salix purpurea* (see figure 4.6-a,c)) because foliage area, being the greatest

area exposed to flow, is negligible in the former. In the case of Salix seedlings, uncertainty in the evaluation of the critical bed erosion is mainly related to the difficulties of estimation of foliage area (Aberle and Järvelä, 2013; Västilä and Järvelä, 2014), as plants with similar characteristics (i.e., height and diameter) can exhibit different foliage area. The hypothesis of root vertical position (root depth equal to root length) represents another source of error (Edmaier et al., 2015). Although the hypothesis can be suitably satisfied in plants grown in uniform grain size soils (Fakih et al., 2017), root architecture can be somehow divergent in natural environments (e.g., riverine habitats), where the presence of large sedimentary objects in the substrate influences root growth (i.e., thigmotropism) (Gregory, 2008).

In order to take into account variability in plant characteristics, we applied the stochastic model proposed by Perona and Crouzy (2018) to our dataset (figure 4.12). We calculated the cumulative distribution of uprooting probability P_τ as the integral of the inverse Gaussian distribution $p_\tau = \frac{e^{-(1-\tilde{T})^2/2\tilde{\sigma}^2\tilde{T}}}{\sqrt{2\pi\tilde{T}^3\tilde{\sigma}}}$ (Eq. (3.2) in Perona and Crouzy (2018)) where $\tilde{T} = T\dot{\eta}/L_r$ is the dimensionless time of uprooting and $\tilde{\sigma}^2 = \sigma^2/L_r\dot{\eta}$ is the dimensionless process variance, and $\dot{\eta}$ is the bed erosion rate, equal to 2 mm min^{-1} (see Section 4.3.1). The variance of the time of uprooting takes into account randomness in sediment transport (i.e., fluctuations induced by flow turbulence or bedforms, scour around stem and grain-grain interactions (Perona and Crouzy, 2018)). We calculated $\tilde{\sigma}^2$ as the variance of the dimensionless time of uprooting $\tilde{T}$, for each combination of species and spatial configuration (Isolated and Non-Isolated). Therefore, the dimensionless process variance $\tilde{\sigma}^2$ includes also all the other sources of randomness (i.e., foliage area and non-vertical root growth).

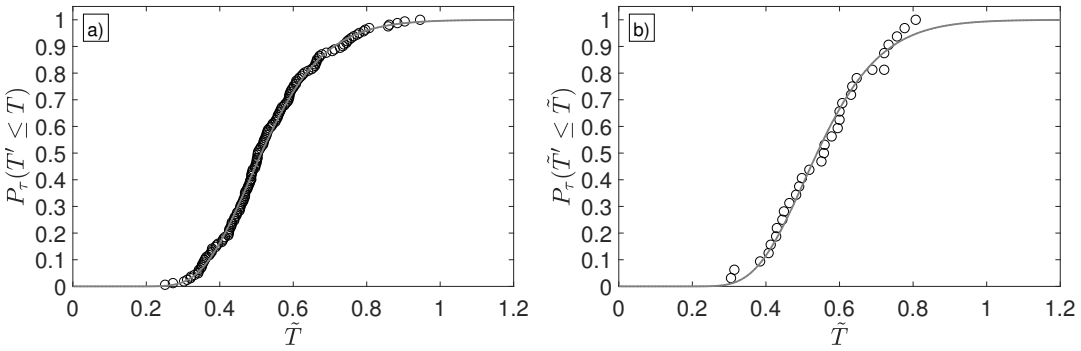

FIGURE 4.12: Application of the stochastic model by Perona and Crouzy (2018) to the experimental data of *Salix purpurea*. Continuous grey lines are the theoretical curve and black points are the empirical data of the cumulative density function (uprooting probability). a) Isolated configuration ($R^2 = 0.99$); b) Non-Isolated configuration ($R^2 = 0.98$).

As an example, figure 4.12 shows the comparison between probability of uprooting P_τ of the Isolated and Non-Isolated *Salix purpurea* and the theoretical curve. The very low probability of uprooting P_τ for dimensionless time of uprooting $\tilde{T}$ less than 0.2 confirms that Type I uprooting is unlikely to occur. As a consequence, Type II uprooting events are delayed with respect to both the initiation of sediment transport (Edmaier et al., 2011) and the presence of bed erosion conditions. This is more

evident in figure 4.12-b) where cooperation among root system of different plants (Non-Isolated configuration) postpones the occurrence of Type II uprooting for most of the seedlings. Indeed, only 3 plants were uprooted for $\tilde{T} < 0.4$. From a general point of view, the good agreement between the experimental data and the stochastic model shows that uncertainty in quantification of the variables (e.g., foliage surface) must be taken into account. However, as the root mean square error $\tilde{\sigma}$ is less than 1 (0.35 and 0.34 for the Isolated and Non-Isolated configuration, respectively), the deterministic drift (i.e., the predicted L_e by the proposed model) prevails on the process noise (Perona and Crouzy, 2018). This supports the capability of our model in predicting the main characteristics of uprooting occurrence (flow and critical bed erosion).

4.6 Conclusion

In this study, we proposed a physics-based model and developed an analytic approach to calculate the critical conditions of either bed shear stress (i.e., Type I uprooting) or bed erosion (i.e., Type II uprooting). Our model addresses the removal of flexible juvenile pioneer vegetation of the type that can be commonly found on gravel river bars in temperate climates, such as the Salicaceae species. Additionally, we performed i) flume experiments with two species of vegetation (*Avena sativa* and *Salix purpurea*) and a quasi-parallel bed erosion setup to simulate uprooting; ii) field measurements of root resistance to pull-out and iii) numerical simulations of a flooding event in the Ombrone Pistoiese River to analyse the predictions obtained using our model in comparison with an authentic case of vegetation removal. The comparison shows the overall capability of the proposed model to correctly capture the uprooting conditions observed both in the flume experiments and in the field.

Moreover, the combination of different approaches (experimental, field and numerical) shows the unlikeliness of Type I compared to Type II removal under flow and bed erosion controls (Bywater-Reyes et al., 2015), even though the larger timescale needed to achieve the critical erosion depth L_e required for the latter mechanism. The implications are related to the eco-morphological evolution of river bars: the area for establishment of pioneer vegetation is typically along the main channel, thus seedlings survival following recruitment is crucial for bar development. In fact, their presence promotes sediment accumulation, bar expansion, outer bank erosion and channel width adjustment.

Chapter 5

A stochastic approach to flow uprooting

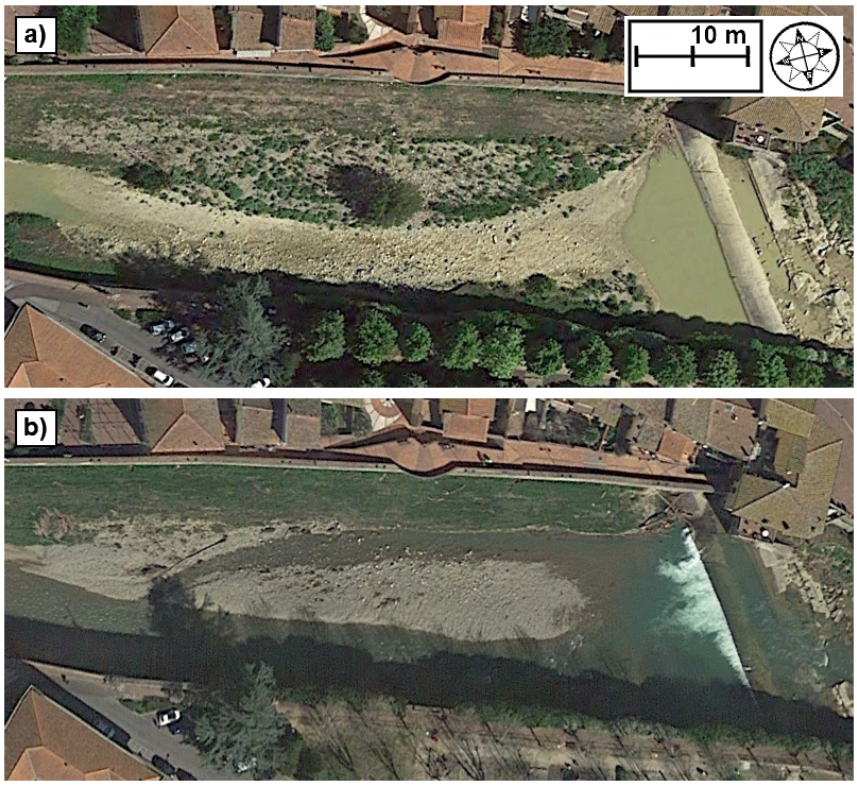

FIGURE 5.1: A river reach of the Pesa River near Montelupo Fiorentino (IT) showing lateral bar deposit shifting from vegetated to barebed configuration after a flood event. a) Vegetated bar with shrubs and small trees in August 2015; b) Barebed configuration in March 2017 (source: Google Earth).

This chapter correlates return period of flood events to the uprooting probability of vegetation by combining stochasticity of flow magnitude and uprooting process.

The work included in this Chapter was conceived and performed while the candidate was visiting the School of Engineering of The University of Edinburgh (UK).
Part of this chapter has been published by the author in *Journal of Hydrology*: doi:10.1016/j.jhydrol.2019.124103 (Calvani et al., 2019c).

5.1 Introduction

Fluvial environments are among the most dynamic systems and their evolution is governed by interactions of vegetation dynamics, sediment processes and flow regime. Riparian plants alter turbulence structures, flow velocity and sediment transport (Nepf, 2012b). At the same time, the alternation of low and high flow discharges drives the recruitment, growth and decay of riparian vegetation (Edmaier et al., 2011). Particularly during high stage events, vegetation is subjected to drag force and plant removal occurs when root anchoring force is reduced through bed erosion to equal the drag force (Edmaier et al., 2011). Vegetation uprooting under flow and scour constraints (Type II) was investigated by Edmaier et al. (2015) in laboratory experiments with *Avena sativa* and by Bywater-Reyes et al. (2015) in field measurements. We used flume experiments with *Avena sativa* and *Salix purpurea* and field measurements to test and validate the proposed model able to predict the critical bed erosion depth for which uprooting occurs (see sections 4.3.1 and 4.3.2). All these studies agree upon the amount of bed erosion required for plant uprooting to occur in relation to the initial plant rooting depth. Perona and Crouzy (2018) hypothesised that the critical erosion depth for Type II uprooting can be achieved by superposition of deterministic erosion (scouring happening at a longitudinal length scale comparable to river width) and random fluctuations mainly induced by turbulence and vegetation-flow interactions. Based on this assumption, they proposed a stochastic model to calculate the uprooting probability of riparian vegetation, by accounting for the time evolution of scour.

The erosion rate is governed by the Exner equation which states that time changing rate in bed elevation depends on the spatial variability of sediment fluxes. In particular, bed erosion takes place when downstream sediment discharge is larger than the upstream one. At the time scale of a flood event, the difference in sediment transport between two consecutive sections is related to the flow velocity and, therefore, to the flow discharge hydrograph. As a result, the achievement of the critical erosion depth L_e during a flood event depends both on the magnitude and the duration of the event itself. The stochastic model for Type II uprooting proposed by Perona and Crouzy (2018) was tested against the dataset of Edmaier et al. (2015) and the predicted values of critical erosion depth for the *Salix purpurea* seedlings tested in section 4.4.1 with good agreement (see figure 4.12 in section 4.5). However, the model was never tested with data from vegetation uprooting in real rivers.

The flow discharge drives the uprooting process and, therefore, the hydrological time scale of flood events governs the dynamics of established riparian vegetation. Accordingly, riparian and aquatic species would have adapted their bio-mechanical properties and life strategies to withstand the flow regime and increase survival chances during stress periods, due to either drought or flood events (Karrenberg et al., 2002; Gibling and Davies, 2012; Gurnell, 2014). As a result, the link between

vegetation dynamics and hydromorphological time scales represents the key factor to understand the biological evolution of riparian species and predict their effects on ecosystem dynamics. However, this link was seldom investigated in literature, particularly by focusing on short time horizon only (Corenblit et al., 2015), whereas the interactions among native and invasive alien species and river morphodynamics employ decades to evolve (Habersack, 2000; Solari et al., 2016).

In this chapter, we link the probability of uprooting P_τ to extreme value analysis of a Compound Poisson Process using the Peak Over Threshold methodology. The Compound Poisson Process (CPP) is a useful tool to represent stochastic systems at a slow dynamic time scale, where instantaneous perturbations cause sudden jumps in the state variable (Cox and Miller, 1965; Ridolfi et al., 2011). Forest fire spread (Daly and Porporato, 2006; Zen et al., 2018), avalanches induced by snowfall (Perona et al., 2007; Perona et al., 2012b), groundwater recharge, soil moisture increase (Rodriguez-Iturbe et al., 1999; Botter et al., 2007), river flood events due to heavy rainfall (Todorovic, 1978; Crouzy and Perona, 2012) and ecomorphodynamics (Bertagni et al., 2018) are only some of the natural processes that can be modelled using the CPP approach. In the following, we focus on flow discharges in a straight channel, characterised by constant width and bed slope. At the same time, Peak Over Threshold (POT) is a common mathematical approach to evaluate the occurrence probability (i.e., return period) of rare extreme events and is widely used in many disciplines, such as meteorology, geological, hydraulic and structural engineering, earth sciences (e.g., Leadbetter, 1991; Novak, 2011; Castillo, 2012). Combining POT and CPP allows to carry out statistical analyses on long term prediction of extreme flood events and correlate their return period to the uprooting probability of riparian vegetation. Additionally, we perform a sensitivity analysis on the parameters involved and test the model with field measurements data from Bywater-Reyes et al. (2015).

5.2 Methods

We first describe flow discharge as the single-state variable of the river system and assume flow variability to be a stochastic process. In particular, this process is driven by a deterministic drift and instantaneous random positive jumps representing the flood events (Botter et al., 2007). Then, we calculate the corresponding deterministic erosion rate, by considering the two main mechanisms of sediment transport (bedload or suspended load). Secondly, we perform an extreme value analysis based on the Peak Over Threshold (POT) methodology to assess flood event return periods and their associated hydrograph. Lastly, we resume the definition of the stochastic model for vegetation uprooting by Perona and Crouzy (2018) and propose a formulation for the random fluctuations of bed erosion. This will allow us to couple the stochastic model for uprooting to a reference average hydrograph for a given return period, and compare hydrological and vegetation time scales.

5.2.1 Hydrological model and erosion events

Consider the flow dynamics in a straight channel as defined by the discharge, $q(t)$, and evolving following a deterministic drift represented by an exponential decrease plus superimposed randomly distributed instantaneous peaks (i.e., shot noise). Flood events are thus represented by the hydrograph raising limb, which can be assumed to be instantaneous at a yearly or even longer temporal scale (Cox and Miller, 1965; Ridolfi et al., 2011). Therefore, the system dynamics can be modelled by a Langevin stochastic differential equation reading:

$$dq/dt = \zeta(t) - q/\tau_P \tag{5.1}$$

Therein, τ_P is an integral temporal scale and $\zeta(t)$ represents the white shot noise. We assume frequency and magnitude of instantaneous peaks be exponentially distributed (i.e., Poisson Process) with mean interval between consecutive pulses λ_P and mean value $\gamma_P = \mu_P/(\lambda_P\,\tau_P)$ with μ_P the average flow discharge of the whole hydrograph (Rodriguez-Iturbe et al., 1999). The solution is given by the probability density function (PDF) of the time-varying flow discharge $q(t)$ and reads:

$$p(q) = \frac{1}{q\Gamma[\beta_P]} \mathrm{e}^{-q/\gamma_P}\,(q/\gamma_P)^{\beta_P} \tag{5.2}$$

where $\Gamma[\beta_P]$ is the Gamma function with argument $\beta_P = \lambda_P\,\tau_P$. Figure 5.2 shows a sample hydrograph and its associated PDF.

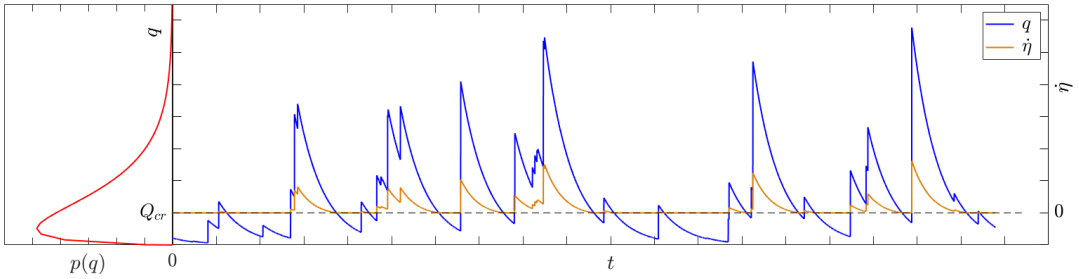

FIGURE 5.2: A sample realisation of a CPP of time-varying flow discharge $q(t)$ based on Eq. (5.2) with $\mu_P = 240$ m^{3}s^{-1}, $\lambda_P = 0.5$ d^{-1} and $\tau_P = 3$ d (blue line). The associated PDF is shown on the left. Orange line is the corresponding erosion rate, positive only for flow discharge higher than the threshold Q_{cr}.

To account for bed elevation changes and scouring leading to Type II uprooting during high flow events, we couple the time-varying flow discharge to the 1D Exner and sediment transport relationships. For the sediment transport, we consider both the cases of bed and suspended load. Specifically, we assume a Meyer-Peter-Müller type formula (Meyer-Peter and Müller, 1948) for bedload and the van Rijn's model (van Rijn, 1984) for the suspended load (see Appendix B). For the resultant relationships to be as simple as possible, we neglect the effects of the time derivative in the momentum equation at the time scale of the process. As a result, bed

shear stress, τ_{bed}, and water depth, Y, can be calculated from flow discharge only, by knowing channel geometry and involving the Manning relation for normal flow. Additionally, for the channel geometry, we assume a wide rectangular cross-section with constant width and bed slope. By combining the aforementioned formulas and assuming negligible upstream sediment discharge (Perona and Crouzy, 2018), we obtain a relationship for the net (deterministic) erosion rate, $\dot{\eta}_d$ (), where the typical structure of sediment transport formula above critical threshold and exponent 3/5 coming from Manning relation can be recognised. The relation reads:

$$\dot{\eta}_d(t) = \psi_1 \, \psi_2 \left(q^{\frac{3}{5}}(t) - Q_{cr}^{\frac{3}{5}} \right)^b \left(q^{\frac{3}{10}}(t) \cdot I(q(t), D_{50}) \right)^{a_{ST}} \tag{5.3}$$

where ψ_1 is a coefficient depending on physical parameters, river size and sediment properties; ψ_2 is a coefficient depending on the main type of sediment load; Q_{cr} is the flow discharge corresponding to incipient sediment motion; b is the exponent in the sediment transport formula (e.g., $^3/_2$ in the case of van Rijn's and MPM's models); $I(q(t), D_{50})$ is a quantity given by the Einstein's integrals (Einstein, 1950) and depending on mean grain size D_{50} and flow discharge in the case of suspended load only (Eq. (B.9)); a_{ST} is a parameter equal to either 0 for bedload or 1 for suspended load. The relation for the parameter ψ_1 reads:

$$\psi_1 = \frac{\sqrt{g}\, D_{50}^{1-b}}{(1-\lambda_s)\Delta x} \left(\frac{\rho_s - \rho}{\rho} \right)^{-b} \left(\frac{n}{B} \right)^{3b/5} S^{7b/10} \tag{5.4}$$

where λ_s is the sediment porosity; Δx is the longitudinal length scale along which net (parallel) bed erosion takes place (see Perona and Crouzy (2018) for explanation); n is the Manning coefficient; B is the river width. The coefficient ψ_2 depends on the main type of sediment transport, according to the following relation:

$$\psi_2 = \begin{cases} \alpha_{BL} \, D_{50}^{1/2} \left(\frac{\rho_s - \rho}{\rho} \right)^{1/2} & a_{ST} = 0 \\ \alpha_{SL} \left(\frac{n}{B} \right)^{3/10} S^{7/20} \, R_{ep}^{-2/10} \, {\tau_{SL}^*}^{-b} & a_{ST} = 1 \end{cases} \tag{5.5}$$

Therein, α_{BL} is the coefficient in the bedload formula (e.g., 3.97 in Wong and Parker (2006)); $\alpha_{SL} = 0.174$ is the coefficient in van Rijn's formula (van Rijn, 1984) for suspended load (see Appendix B); R_{ep} is the particle Reynolds number; τ_{SL}^* is the critical Shields number for incipient motion of suspended particles (Brownlie, 1981).

The threshold flow discharge for the initiation of bed erosion, Q_{cr}, is imposed equal to the one for incipient sediment motion. The latter can be calculated by taking into account the critical Shields parameter τ_{cr}^*, and the relation reads:

$$Q_{cr} = {\tau_{cr}^*}^{5/3} \left(\frac{\rho_s - \rho}{\rho} \right)^{5/3} D_{50}^{5/3} \, \frac{B}{n} \, S^{-7/6} \tag{5.6}$$

where τ_{cr}^* is the critical Shields parameter equal to either 0.03, according to Parker

et al. (2007) for gravel bed rivers subjected to bedload transport, or τ^*_{SL} for sand-bed rivers with suspended load.

5.2.2 Peak Over Threshold

The stochastic model for the uprooting of vegetation (Perona and Crouzy, 2018) requires to know the net erosion rate $\dot{\eta}_d$. As we seek to link the uprooting probability to the corresponding return period, we need to know the mean hydrograph event associated to such return period. Then, the net erosion rate can be calculated using Eq. (5.3). Therefore, we first assess the return periods by involving extreme value analysis tools, then we calculate the corresponding reference mean event, $Q_{\tilde{\xi}}(t)$.

Extreme value analysis is a common tool to evaluate the occurrence of rare events. We perform an extreme value analysis using the Peak Over Threshold (POT) methodology developed by Todorovic (1970) and then applied to exponentially distributed peak events (CPP) by Zelenhasic (1970). POT can be applied when large time series data are available and independent and identically distributed (i.i.d.) and, as a consequence, is one of the most commonly used method in hydrology and hydraulic engineering (Solari and Losada, 2012). As POT is a well established methodology (e.g., Todorovic, 1970; Zelenhasic, 1970; Lang et al., 1999; Solari and Losada, 2012), the mathematical details are omitted here (detailed explanation of the mathematical steps can be found in Appendix C). Once a certain threshold, $\tilde{\xi}$, is set and the CPP of flow discharges is accounted for, the POT probability, $P_{\tilde{\xi}}$, (i.e., the probability of events higher than $\tilde{\xi}$) reads:

$$P_{\tilde{\xi}} = \mathrm{e}^{-\lambda'_P \, P^+_{\tilde{\xi}}} \tag{5.7}$$

where $\lambda'_P = \frac{1}{T^+_{\tilde{\xi}} + T^-_{\tilde{\xi}}} = \frac{\mathrm{e}^{-\phi} \, \phi^{\beta_P}}{\tau_P \, \Gamma[\beta_P]}$ (Eqs (C.1) and (C.2)) is the frequency of events above the threshold $\tilde{\xi}$; ϕ is the ratio between the threshold $\tilde{\xi}$ and the mean value of pulses γ_P; $P^+_{\tilde{\xi}} = \frac{\Gamma[\beta_P, \phi]}{\Gamma[\beta_P]}$ is the probability of flow discharge values higher than the threshold $\tilde{\xi}$ where $\Gamma[\beta_P, \phi]$ is the upper incomplete Gamma function (Abramowitz and Stegun, 1965). Therein, $T^+_{\tilde{\xi}}$ and $T^-_{\tilde{\xi}}$ represent the average time above and below the threshold $\tilde{\xi}$, respectively, and can be calculated using theory on stochastic processes driven by white shot noise (Cox and Miller, 1965; Ridolfi et al., 2011), as:

$$T^+_{\tilde{\xi}} = \frac{1}{\lambda_P} \, {}_1F_1[1; 1 + \beta_P; \phi] \, \frac{\Gamma[\beta_P, \phi]}{\Gamma[\beta_P] - \Gamma[\beta_P, \phi]} \tag{5.8}$$

$$T^-_{\tilde{\xi}} = \frac{1}{\lambda_P} \, {}_1F_1[1; 1 + \beta_P; \phi] \tag{5.9}$$

where ${}_1F_1[\,\cdot\,;\,\cdot\,;\,\cdot\,]$ is the confluent hypergeometric function of the first kind, namely Kummer function (Abramowitz and Stegun, 1965).
We update the shot noise frequency (i.e., from λ_P to λ'_P), as the POT analysis deals

with constant rate processes and this is valid for CPP only at very high values of the threshold ξ (compared to than mean value, μ_P). As a result, the return period $T(\xi)$ of events higher than the threshold ξ simply reads:

$$T(\xi) = \frac{1}{1 - P_{\xi}} \tag{5.10}$$

5.2.3 Reference mean event

We now proceed to define the corresponding reference mean event, $Q_{\xi}(t)$. The reference mean event is a statistically averaged flow hydrograph following a jump (peak) above the threshold ξ. For the sake of simplicity, we assume the reference mean event to start when flow up-crosses such threshold ξ. Moreover, as we focus on Type II uprooting driven by bed erosion (Edmaier et al., 2015; Bywater-Reyes et al., 2015) (see also section 4.3.1), we consider the event to finish when flow discharge down-crosses the lower threshold Q_{cr}. Because of the extreme value analysis, it is trivial to assume the threshold ξ higher than the threshold Q_{cr} for bed erosion.

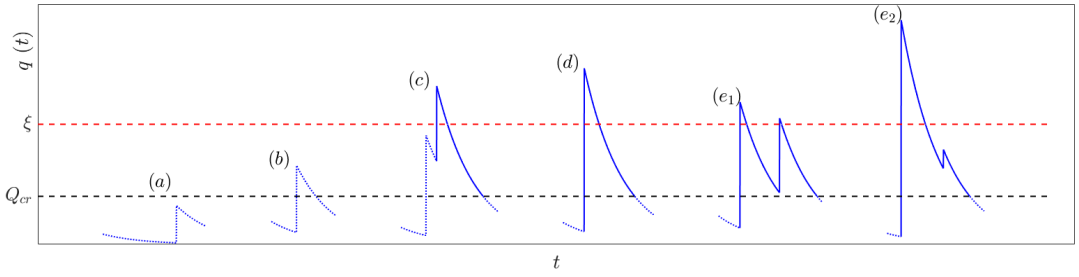

FIGURE 5.3: Typical peak events above and below Q_{cr} and ξ thresholds in a CPP of flow discharge $q(t)$. The whole stochastic process can be reconstructed by combining and merging different peak events (see figure 5.4-b)) for some possible events above threshold ξ). Continuous blue line is for the hydrograph we take into account to build the reference mean event $Q_{\xi}(t)$, dashed line for the discarded events or parts of them.

A typical CPP of flow discharges (see figure 5.2) is made by randomly high and distributed peaks, each one followed by an exponential decreasing. However, once set the thresholds ξ and Q_{cr}, peak events can be gathered in five main types. Figure 5.3 shows the different typologies of peak events:

(a) the flow discharge during the event is always below the lower threshold Q_{cr};

(b) the peak overtakes Q_{cr} but always remains below the higher threshold ξ;

(c) the event is composed by a sequence of two peaks such that the first one is higher than Q_{cr} but lower than ξ and the second jump allows to overtake the higher threshold before flow decreases below Q_{cr};

(d) the peak overtakes both the thresholds at the same time then flow exponentially decreases until lowering threshold Q_{cr};

(e) the event is similar to the (d)-type but, before flow reaches the lower threshold Q_{cr}, a new peak occurs, either able to overcome again threshold ξ (e_1) or not (e_2).

To the Peak Over Threshold analysis, we therefore discard (a) and (b) types of peak events and neglect the first part of (c)-type peak events. Then, we calculate $Q_\xi(t)$ by keeping some properties of the general hydrograph unchanged, in particular the average flow duration, T_ξ^+, the mean flow value, $\overline{Q}_{q>\xi}$, above the threshold ξ, and the average flow duration from threshold ξ to Q_{cr} during the falling limb, $T^+_{\xi\to Q_{cr}}$. More in detail, once set the threshold ξ, we consider a peak event, $Q_0(\xi)$, happening at $t = 0$ and exponentially decreasing to reach $Q_\xi(t) = \xi$ at $t = T_\xi^+$. Then, a second exponential decrease drives the flow from ξ to Q_{cr} lasting $T^+_{\xi\to Q_{cr}}$. The total duration of the event is therefore equal to $\hat{T}_\xi = T_\xi^+ + T^+_{\xi\to Q_{cr}}$ (see figure 5.4-a)) for a graphical explanation). Therein, the bed erosion rate $\dot{\eta}(t)$ is calculated according to Eq. (5.3) for both the sediment transport mechanisms and the critical flow discharge Q_{cr} using Eq. (5.6).

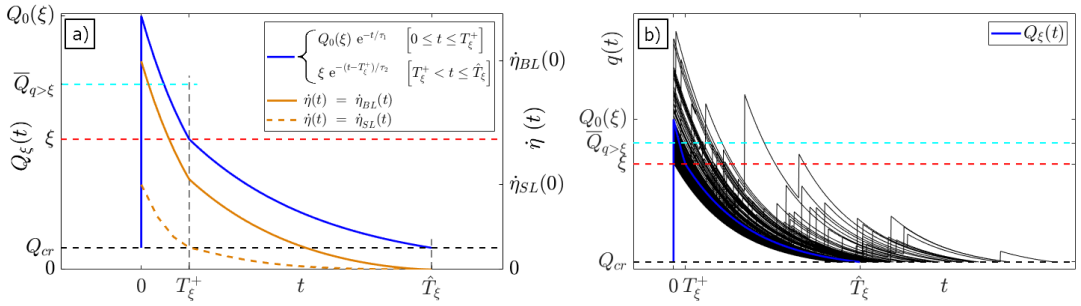

FIGURE 5.4: The general outline of the reference mean event $Q_\xi(t)$ and the associated bed erosion rates $\dot{\eta}$ according to the main type of sediment load. a) the reference mean event $Q_\xi(t)$ in blue for a given threshold ξ and the main quantities involved in its calculation. Dark yellow lines identify the erosion rate $\dot{\eta}$ according to the main type of sediment transport: continuous line for the bedload transport (subscript BL), dashed line for the suspended load (subscript SL). b) a comparison between the reference mean event $Q_\xi(t)$ and some events above the same threshold ξ from a Compound Poisson Process. $Q_\xi(t)$ is the statistical average of all the possible events overcoming the threshold ξ.

The reference mean event $Q_\xi(t)$ is defined by a piecewise function (figure 5.4-a)):

$$Q_\xi(t) = \begin{cases} Q_0(\xi)\, \mathrm{e}^{-t/\tau_1} & \left[0 \le t \le T_\xi^+\right] \\ \xi\, \mathrm{e}^{-(t-T_\xi^+)/\tau_2} & \left[T_\xi^+ < t \le \hat{T}_\xi\right] \end{cases} \tag{5.11}$$

The unknown parameters $Q_0(\xi)$, τ_1 and τ_2 are calculated to fulfil the three aforementioned conditions, as reported here below.

$$Q_\xi(t = T_\xi^+) = \xi \tag{5.12}$$

$$\int_0^{T_\xi^+} Q_\xi(t)\, dt = T_\xi^+\, \overline{Q}_{q>\xi} \tag{5.13}$$

$$Q_\xi(t = \hat{T}_\xi) = Q_{cr} \tag{5.14}$$

As a result, after some maths, we find:

$$Q_0(\xi) = \xi \, \mathrm{e}^{T_\xi^+ / \tau_1} \tag{5.15}$$

$$\tau_1 = \frac{-T_\xi^+}{\frac{\xi}{\overline{Q}_{q>\xi}} + W_{-1}\left[\frac{-\xi}{\overline{Q}_{q>\xi}} \, \mathrm{e}^{-\xi/\overline{Q}_{q>\xi}}\right]} \tag{5.16}$$

$$\tau_2 = \frac{T^+_{\xi \to Q_{cr}}}{\log\left(\xi / Q_{cr}\right)} \tag{5.17}$$

In Eq. (5.16), the letter W_{-1} identifies the second limb of the Lambert function (Corless et al., 1996). As a matter of fact, the first limb (W_0) provides the trivial solution with $\tau_1 = \infty$ and $Q_\xi(t) = \overline{Q}_{q>\xi}$ in $t = \left[0, T_\xi^+\right]$. Temporal quantities are calculated according to the analysis made by Laio et al. (2001), whereas average value above threshold is calculated using theory on stochastic processes driven by white shot noise (Ridolfi et al., 2011). Involved relations are reported here below (see also Eqs (5.6) and (5.8)).

$$\begin{aligned} T^+_{\xi \to Q_{cr}} = {} & \tau_P \phi_{cr}^{-\beta_P} \, \mathrm{e}^{\phi_{cr}} \, \Gamma[\beta_P, \phi_{cr}] \; - \; \tau_P \phi^{-\beta_P} \, \mathrm{e}^{\phi} \, \Gamma[\beta_P, \phi] \\ & + \tau_P (-1)^{\beta_P} \, \Gamma[\beta_P] \; \left(\Gamma[1-\beta_P, -\phi] \; - \; \Gamma[1-\beta_P, -\phi_{cr}]\right) \\ & + \frac{1}{\lambda_P} \, \phi_{cr} \, {}_2F_2[1,1;2,1+\beta_P;\phi_{cr}] \\ & - \frac{1}{\lambda_P} \, \phi \, {}_2F_2[1,1;2,1+\beta_P;\phi] \end{aligned} \tag{5.18}$$

$$\overline{Q}_{q>\xi} = \frac{\mu_P}{\beta_P} \, \frac{\Gamma[1+\beta_P, \phi]}{\Gamma[\beta_P, \phi]} \tag{5.19}$$

where ${}_2F_2[\,\cdot,\cdot\,;\,\cdot,\cdot\,;\,\cdot\,]$ is the generalised hypergeometric function (Prudnikov et al., 1986). The comparison between the reference mean event and the superposition of the events above the threshold ξ is shown in figure 5.4-b) .

5.2.4 The uprooting model

The probability of uprooting by flow for a given erosion event is computed using the stochastic model developed by Perona and Crouzy (2018). The PDF of uprooting times reads:

$$p_\tau(t) = \frac{L_e}{2\sqrt{\pi \, G^3(t)}} \left(\frac{g_t(t)}{2} \exp\left[- \frac{(L_e - V(t))^2}{4 \, G(t)} \right] + W(t) \exp\left[\frac{L_e \, V(t)}{G(t)} \right] \right) \tag{5.20}$$

where $g_t(t)$ is related to the Gaussian noise of the erosion process, $G(t) = \frac{1}{2}\int_0^t g_t(\tau) d\tau$, $V(t) = \int_0^t \dot{L}_d(\tau) d\tau$ and $W(t) = \sqrt{\pi \, G(t)} \; \mathrm{Erfc}\left[\frac{L_e + V(t)}{2\sqrt{G(t)}}\right] \left(\dot{L}_d(t) - \frac{g_t(t)}{2} \, \frac{V(t)}{G(t)}\right)$, with τ a dummy time variable of integration. Therein, the deterministic part of the root exposing rate due to bed erosion is $\dot{L}_d = \dot{\eta}_d(t) \; dL/d\overline{\eta}$ where $dL/d\overline{\eta}$ accounts

for the root shape and architecture within the soil. We assume $dL/d\overline{\eta} = 1$ under the simplifying hypothesis of root vertical position (Edmaier et al., 2015). This simplifying hypothesis was previously involved in Eq. (4.3) to predict the critical erosion length L_e.

The quantity g_t has the unit of a diffusivity (i.e., $m^2\,s^{-1}$) and takes into account the stochasticity in sediment transport rate. Since no formulation are available in literature, we argue that a relation for the quantity g_t can resemble the formula of the eddy viscosity, ν_t (Pope, 2001; Michael, 2015), because the disturbances in sediment transport are directly related to, among other factors, fluid-obstacle interactions and flow turbulence at the stem scale (Nepf, 2012b; Perona and Crouzy, 2018). Thus, the formula reads:

$$g_t(t) = l_s \cdot u_* \tag{5.21}$$

where l_s is the *sediment mixing length* (i.e., a length scale along the vertical direction y) which plays the analogous role of the Prandtl mixing length, l_m, for the flow velocity, and u_* is the shear velocity, that plays the role of a velocity scale along the longitudinal direction x, similarly to the case of eddy viscosity, ν_t. We set the sediment mixing length, l_s, equal to the mobilised sediment layer thickness, which is in the order of magnitude of the D_{90} (Parker, 1990) (i.e., $l_s = k_g \cdot D_{90}$), and, for consistency in unit of measurement, a multiplying constant of $1\,s\,d^{-1}$ has to be taken into account when considering the Wiener process strength (see Eq. (2.10) in Perona and Crouzy (2018)).

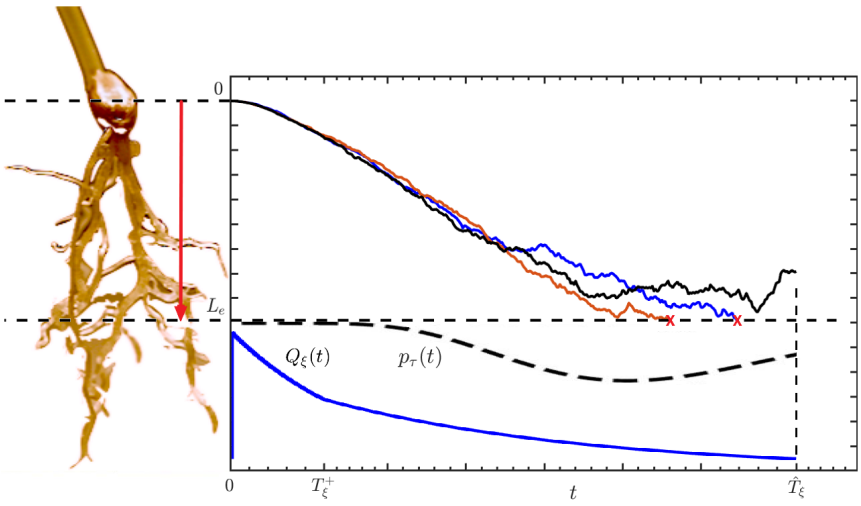

FIGURE 5.5: Illustration of the approach described by Eq. (5.22). The erosion rate evolves according to Eq. (5.3) and stochasticity g_t, both driven by flow rate of the reference mean event $Q_{\bar{\xi}}(t)$. Vegetation is removed when total erosion reaches the threshold L_e.

Finally, the relation for the probability of Type II uprooting $P_\tau(t)$ reads (Perona and Crouzy, 2018):

$$P_\tau(t) = \int_0^t p_\tau(\tau)\, d\tau \tag{5.22}$$

In our analysis, we calculate the probability of uprooting at the end of the reference mean event, namely $P_\tau(t = \hat{T}_\xi)$ (figure 5.5).

5.3 Results

We compared numerical and analytic values to assess the reliability of our model for the reference mean event, in terms of total duration $\hat{T}_\xi$ of the reference mean event $Q_\xi(t)$ and flow volume from $Q_0(\xi)$ to Q_{cr}. Then, we performed a sensitivity analysis on the parameters λ_P and τ_P to evaluate the effects on the reference mean event duration and minimum return period for POT validity. Lastly, we presented results on the uprooting probability of reference mean events $P_\tau(t = \hat{T}_\xi)$ according to their return period. The uprooting probability is function of many variables, so we considered the effects of one parameter at a time. In particular, we varied the critical erosion for uprooting, L_e, the average frequency of peak flows, λ_P, the integral temporal scale τ_P, and the coefficient α_{BL} for bed erosion in case of bedload transport. For this part of the analysis, we considered the quantity g_t constant. We took into account the effects of a time-varying g_t and k_g in the discussion (section 5.4).

5.3.1 Reference mean event

We first verified the analytical form of the reference event duration $\hat{T}_\xi$ (Eqs (5.8) and (5.18)) using numerical simulations. Numerical data were extracted from a CPP of flow discharges with different values of parameters λ_P and τ_P. In particular, we considered four values of the average frequency of peak occurrence (λ_P = 0.01, 0.05, 0.1, 0.2 d^{-1}) and four values of the autocorrelation time (τ_P = 1, 3, 5, 7 d) for a total of 16 tested combinations. We also did the comparison for the flowed volume during the reference mean event (i.e., from $Q_0(\xi)$ to Q_{cr}) corresponding to a fixed threshold ξ. The analytic evaluation for the flow volume is given by $\int_0^{\hat{T}_\xi} Q_\xi(t)dt$. Figure 5.6 shows the graphical results of the analysis for the tested combinations of λ_P-τ_P parameters.

We found a almost perfect agreement between analytical and numerical results for the time $\hat{T}_\xi$ for all the tested combinations with respect to the threshold ξ. The agreement seems to decrease when for very high thresholds ξ and large parameter values (e.g., λ_P=0.20 d^{-1}, τ_P=7 d). However, this depends only on the restricted number of peak events higher than the threshold ξ. Indeed, bottom-right inset panel in figure 5.6-a) shows null duration for peak events higher than ξ=3000 $m^3\,s^{-1}$ which is reasonably unfeasible. For the flow volume, we found a slightly lower agreement between numerical data and analytical solution. In particular, the analytical value underestimates the flow volume when the peak frequency λ_P is very low, i.e., less than 0.1 d^{-1} (e.g., for ephemeral rivers), whereas it overestimates for λ_P>=0.1 d^{-1} when threshold ξ is very high (see inset panels in figure 5.6-b)). Nevertheless, the

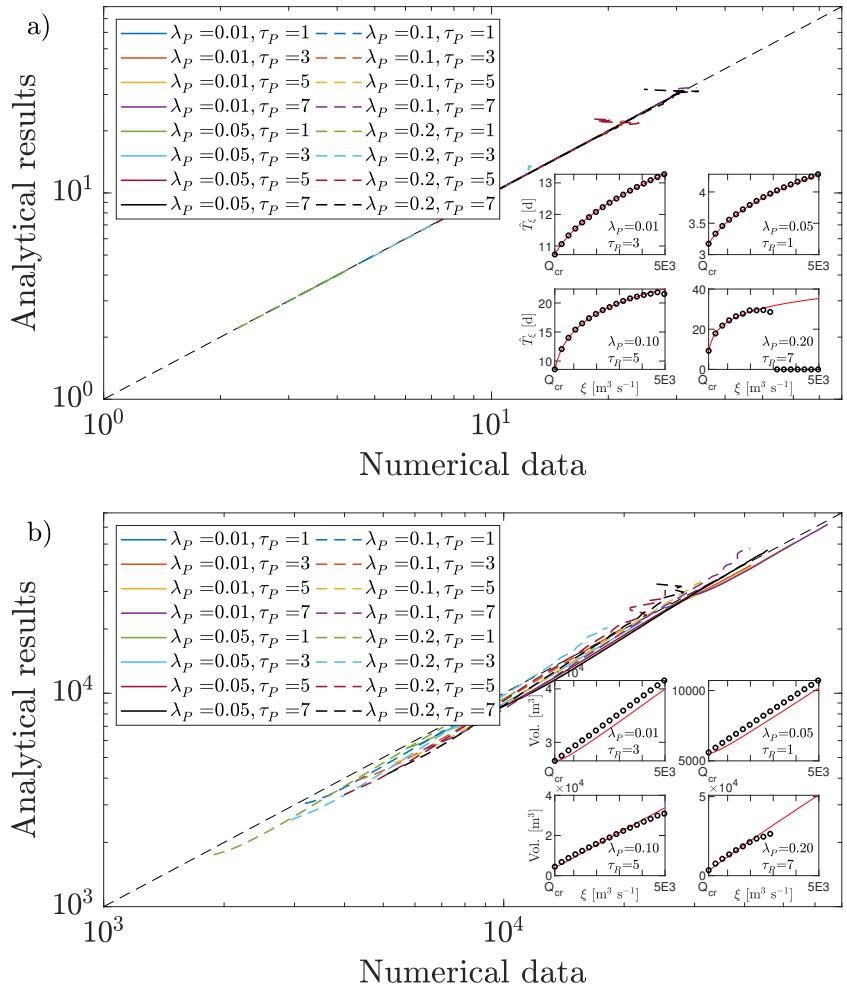

FIGURE 5.6: Graphical comparison between analytical and numerical results for the tested combinations of parameter λ_P-τ_P. Units are [d^{-1}] for λ_P and [d] per τ_P. a) Comparison for the peak event duration $\hat{T}_\xi$ from $Q_0(\xi)$ to threshold Q_{cr}. b) Comparison for the flow volume during the reference mean event. The inset panels show the comparison with respect to the referring threshold ξ for some of the tested combinations. Black points represent the numerical results, blue line is the analytical solution.

error is generally lower than 5%, whereas, for particular λ_P-τ_P combinations, it increases up to 10%. This supports the consistency of the proposed formulation for the reference mean event, $Q_\xi(t)$.

5.3.2 Sensitivity analysis

We investigated the effects of the parameters λ_P and τ_P on the peak event duration $\hat{T}_\xi$ above the threshold Q_{cr} for extreme events. We considered the occurrence of such events by the return period analysis, given by Eq. (5.10). Figure 5.7 shows the results of the analysis performed with some combinations of the two parameters λ_P and τ_P. In particular, it shows that the parameter λ_P governing the peak event frequency is responsible for varying the minimum return period below which the POT analysis does not work, although this minimum value is very low (i.e., lower than 1 y).

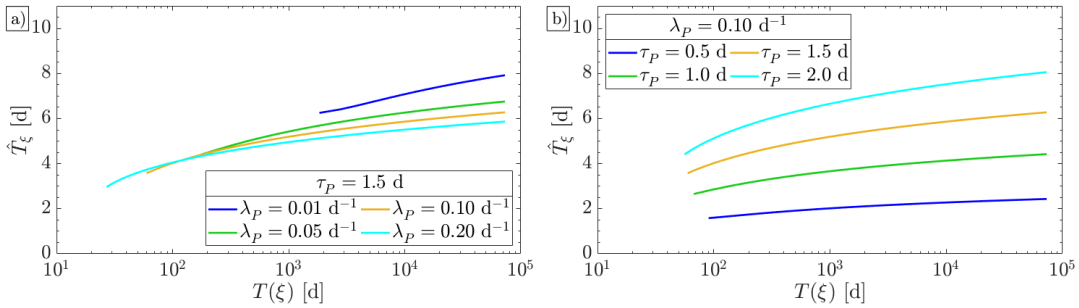

FIGURE 5.7: Effects of varying the parameters λ_P and τ_P on the total duration $\hat{T}_\xi$ of the reference mean event $Q_\xi(t)$ above threshold Q_{cr} versus the return period $T(\xi)$ correspondent to the peak event above the same threshold ξ. $\hat{T}_\xi$ is calculated for a given average flow discharge μ_P=240 m^3 s^{-1}. a) curves with different average peak frequency λ_P. b) curves with different integral temporal scale τ_P.

Figure 5.7-a) shows the effects of varying the parameter λ_P on the reference mean event duration $\hat{T}_\xi$. For return period less than 10^3 d, the duration $\hat{T}_\xi$ does not change significantly. For higher return periods, differences among curves are remarkable only when considering the lowest tested λ_P (e.g., λ_P=0.01d^{-1}). Additionally, it is clearly recognisable the effect on the value of the minimum return period for the validity of the extreme value analysis using the POT method. Again, for λ_P=0.01d^{-1} the minimum return period is approximately larger than 3 y, whereas for the other tested values it is less than 3 y, with a value of 30 d for the largest tested λ_P (λ_P=0.20 d^{-1}). The trend is in agreement with POT analysis which requires a large number of events for its consistency (Leadbetter, 1991; Lang et al., 1999; Castillo, 2012).

Figure 5.7-b) shows the effects of varying the integral temporal scale τ_P. The curves show a similar minimum value of return period (differences among curves are in the order of some days) for the tested values of τ_P. Moreover, the total duration $\hat{T}_\xi$ clearly increases only for high values of τ_P and remains almost constant when the integral temporal scale is low (e.g., τ_P=0.5 d). As a matter of fact, a high value of τ_P extends the duration of the exponential decreasing and, therefore, increases the chances for new peaks to occur before reaching the lower threshold Q_{cr}. As a result, the total duration of the reference mean event is longer.

Globally, figure 5.7 shows that the reference mean event $Q_\xi(t)$ generally lasts for many fewer days than the corresponding return period (i.e., $\hat{T}_\xi \ll T(\xi)$). Indeed, we found comparable values of $\hat{T}_\xi$ and $T(\xi)$ only for very small values of the return period (i.e., $T(\xi)$<20 d) which can be reasonably discarded when dealing with extreme events. This supports the validity of joining the reference mean event and POT approach.

5.3.3 Return periods of uprooting events

We linked the Peak Over Threshold analysis to the probability of vegetation removal driven by general bed erosion (Type II uprooting). Due to the complex relation for

the $P_\tau(t = \hat{T}_\xi)$, we performed a graphical analysis on the effects of varying parameter values, one at a time. In particular we considered the effects of the critical erosion for uprooting, L_e, the coefficient α_{BL} in bed load sediment transport formula, the average frequency of peak flows, λ_P, and the integral temporal scale τ_P. Figure 5.8 shows the trend of the uprooting probability function $P_\tau(t = \hat{T}_\xi)$ versus the corresponding return period T_ξ. For the sake of simplicity, we performed the calculations

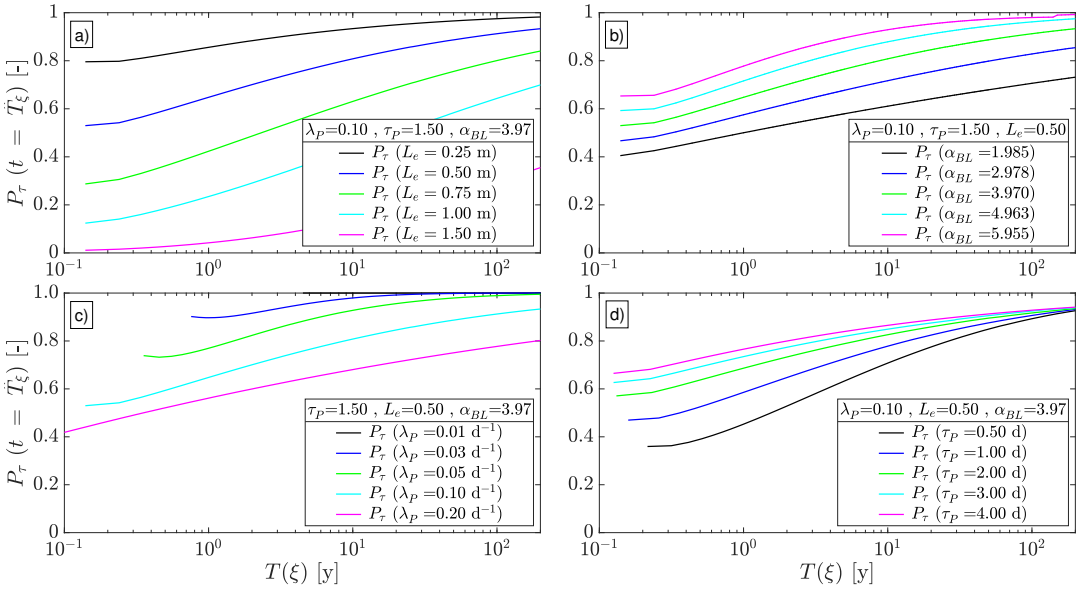

FIGURE 5.8: Uprooting probability, $P_\tau(t)$, at the end of the reference mean event ($t = \hat{T}_\xi$), according to different values of the parameters involved in Eq. (5.22). Mean flow discharge μ_P is set to 400 m^3 s^{-1}, g_t is set to 0.05 m^2 d^{-1}, values of the other constant parameters are shown. When not explicitly written, units are: [m] for L_e, [d^{-1}] for λ_P, and [d] for τ_P. a) $P_\tau(t = \hat{T}_\xi)$ versus return period varying the critical length of erosion L_e; b) $P_\tau(t = \hat{T}_\xi)$ versus return period varying the coefficient α_{BL} in the bedload transport formula; c) $P_\tau(t = \hat{T}_\xi)$ versus return period varying the mean frequency of jumps λ_P; d) $P_\tau(t = \hat{T}_\xi)$ versus return period varying the temporal integral scale τ_P.

of $P_\tau(t = \hat{T}_\xi)$ for an ideal river characterised by cross section width B equal to 100 m, bed slope S equal to 0.002 and mean grain size D_{50} equal to 0.04 m, subjected to bedload, regardless of the Shields number. A D_{90} equal to 0.1 m is used to calculate a Manning coefficient n equal to 0.262 s m$^{-1/3}$. The hydrology is characterised by a mean flow discharge μ_P of 400 m^3 s^{-1} and the length Δx is set equal to 10 times the length scale of potential river bars, approximately equal to 5·B (Leopold and Wolman, 1957). Additionally, we kept constant the value of fluctuations of the sediment transport rate (g_t=0.05 m^2 d^{-1}), regardless of Eq. (5.21), to highlight the changes induced by the other investigated parameters.

Figure 5.8 shows curves associated to different values of involved parameters. As expected, the critical erosion depth L_e plays an important role in the probability of uprooting. Indeed, figure 5.8-a) shows that an increment of 0.25m in L_e (e.g., from 0.5 m to 0.75 m) raises survival chances (=1-P_τ) by 20% for a yearly flood event. According to the model proposed in section 4.2 (Eq. (4.3), plants do not need to grow root depth of that amount, as soil strength increases going down. Furthermore,

the same gain in L_e can be achieved by reducing the frontal area subjected to drag, either by increasing flexibility (i.e., reconfiguration) or by physically losing leaves. The latter mechanism appears to be a possible strategy for riparian plants in the temperate zone to adapt their deciduous period to autumn and winter seasons, not only to save energy, but also to withstand the larger and more frequent peak events.

For the effects of the coefficient of the bedload transport formula, we considered the original value proposed by Wong and Parker (2006) and four other values, differing by $\pm$25% and $\pm$50%. Figure 5.8-b) shows that increasing (decreasing) the coefficient α_{BL} by 25% raises (decreases) uprooting probability by approximately 5% in the whole range of tested return periods. As a result, the parameter α_{BL} in the range of tested values does not seem to significantly affect the uprooting probability.

On the contrary, the frequency of events plays a key role. Figure 5.8-c) shows, for example, that vegetation in ephemeral rivers, for which frequency of peak is very low ($\lambda_P \leq$0.03 d^{-1}) is totally or almost completely uprooted ($P_\tau(t = \hat{T}_{\tilde{\xi}}) \geq$70%). For the involved value of critical erosion depth (L_e=0.5 m), a small percentage of plants can survive to the 200 y return period event only when peak frequency λ_P is larger than 0.05 d^{-1}) (e.g., 10% for λ_P=0.10 d^{-1} and 20% for λ_P=0.20 d^{-1}). Nevertheless, by including considerations on figure 5.8-a), one can argue that survival probability of younger plants and pioneer seedlings with longer L_e is even higher.

Figure 5.8-d) shows the results of the sensitivity analysis on the parameter τ_P. For the tested values of τ_P, the integral temporal scale affects plant removal probability only for very low flow return period (i.e., $T(\xi) < 5$ y), whereas the probability varies only in the order of 10% for higher return periods. Yet, it is remarkable to note that for low return periods the uprooting probability is higher for high values of the integral temporal scale, whereas a different behaviour can be found for high return periods. We explain this trend by considering the different reference mean events obtained with a low (e.g., τ_P=0.5 d) and a high (e.g., τ_P=3 d) values of the integral temporal scale. For low values, the mean reference event is mainly representative of a single peak event ((d)-type event, see figure 5.3), with low probability of further peak events during the falling limb due to the short duration $\hat{T}$ (e.g., $\hat{T} \approx$ 2 d, see figure 5.7-b)). As a result, the uprooting process is mainly driven by the magnitude of the peak. Conversely, when the parameter τ_P is high (namely larger than 2 d), the occurrence of other peaks events is more probable. For this reason, the reference mean event is represented by a sequence of (e)-type events (see figure 5.3) with a longer duration above the threshold Q_{cr} and, therefore, the uprooting probability is higher for low return periods. We refer to this dualism as *magnitude driven* and *duration driven* uprooting events.

5.4 Discussion and application example

In this section, we focused on Eq. (5.21) and the associated time-varying g_t. Moreover, we applied the model to field measurements of uprooting provided by Bywater-Reyes et al. (2015) on the Santa Maria River (Arizona, USA), shown in figure 5.9.

FIGURE 5.9: The reach of the Santa Maria River investigated by Bywater-Reyes et al. (2015). Flow is from right to left. The Santa Maria River is an ephemeral channel, mostly dried during the year.

First, we investigated the effects of different values of k_g (i.e., different thickness of the mobilised sediment layer) and compared the resulting uprooting probabilities with constant and time-varying g_t. For the sake of the analysis, we considered the constant g_t as the integral average of the time-varying one over the entire duration $\hat{T}_\xi$ of the reference mean event $Q_\xi(t)$ for a given return period $T(\xi)$.

Figure 5.10 shows the comparison among uprooting probabilities with constant and time-varying g_t according to different values of k_g. Time-varying g_t plays a significant role in modifying the resultant $P_\tau(t = \hat{T}_\xi)$ only for either very high or very low values of k_g (e.g., $k_g = 0.2$ or $k_g = 20$). For more reasonable values (e.g., $k_g = 2$ (Parker, 1990)), the uprooting probabilities are very similar and, therefore, the average value defines the entire trend. Moreover, for values of k_g equal to 4, time-varying g_t increases the uprooting probability for low return periods (e.g., $T(\xi)$<11 y), whereas $P_\tau(t = \hat{T}_\xi)$ is almost equal for slightly higher recurrence intervals (e.g., 10 y <$T(\xi)$<50 y). For higher return period ($T(\xi)$>50 y), the uprooting probability with the time-varying g_t is lower than the correspondent with constant g_t. For even higher values ($k_g = 20$), the uprooting probability with time-varying g_t is always larger, for the tested range of return period and hydrological parameters. It is interesting to highlight that for k_g lower than 4, the uprooting probability function behaves in the opposite way. We didn't investigate on the threshold value of k_g that switches between the two different trends.

Then, we applied the POT theory with reference mean event and the uprooting model to the Santa Maria River (Arizona, USA) (see figure 5.9). This river was

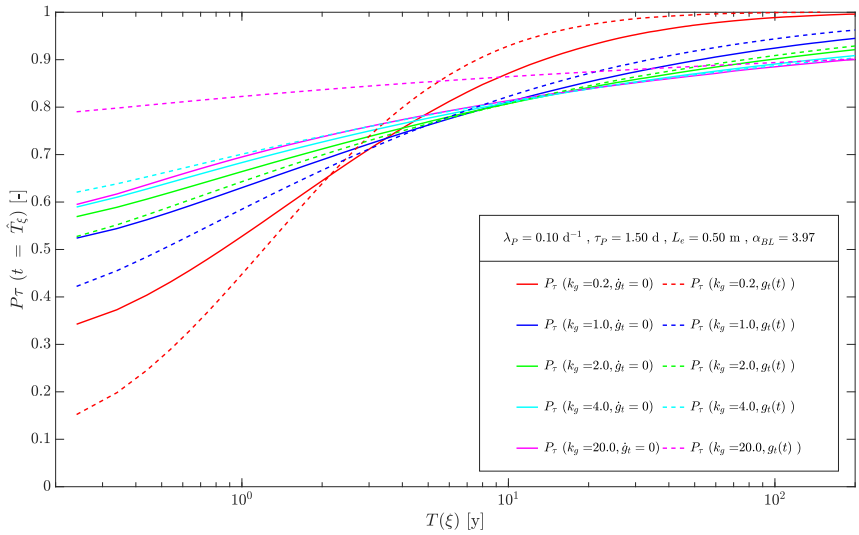

FIGURE 5.10: Graphical comparison of the uprooting probability, $P_\tau(t = \hat{T}_\xi)$, versus the return period, $T(\xi)$, for different values of the time-varying erosion noise, $g_t(t)$, and its integral mean over the duration $\hat{T}_\xi$ for different values of the scale k_g of the *sediment mixing length* l_s. Continuous lines are for the uprooting probability with constant g_t, dashed lines are for the one with time-varying g_t. High differences in the resultant P_τ are observed only for k_g either larger than 10 (e.g., $k_g = 20$) or smaller than 1 (e.g., $k_g = 0.2$).

investigated by Bywater-Reyes et al. (2015) and plants on a bar along it were mechanically uprooted under different conditions of scouring (2.6). As a results, data of flow discharge to fit the CPP and measurements of root resistance and plant geometry are largely available. Figure 5.11-a) shows the reference mean event and its associated erosion rate $\dot{\eta}$ driven by suspended load (a_{ST}=1 in Eq. (5.3)) for the 10 y return period peak event. We calculated the uprooting probability according to dif-

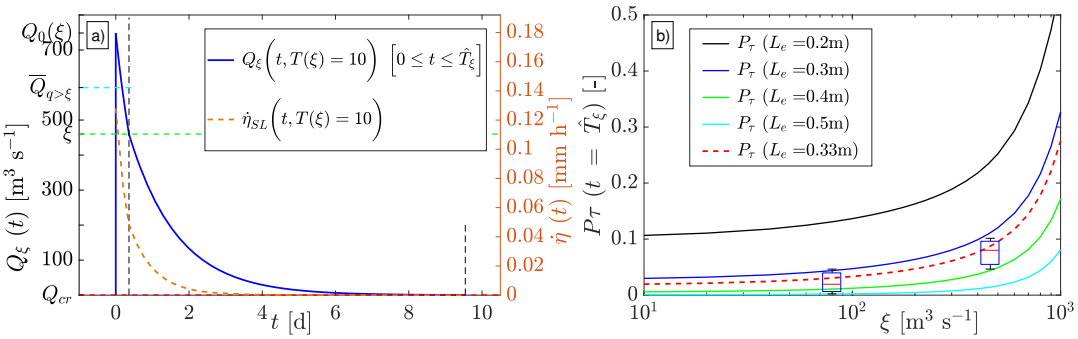

FIGURE 5.11: The uprooting probability in the Santa Maria River, Arizona (USA) and the comparison with data calculated by Bywater-Reyes et al. (2015). a) The reference mean event for 10 y return period and its associated erosion rate $\dot{\eta}(t)$ due to suspended load. b) Comparison of $P_\tau(t = \hat{T}_\xi)$ with different L_e for the Santa Maria River (Arizona, USA). Boxplots are the probability of uprooting calculated with measured data by Bywater-Reyes et al. (2015) for 2 and 10 y return periods. Good agreement between model and data is found for L_e calculated using the approach proposed in section 4.2.

ferent critical erosion length L_e and compared the results for the two flow discharges investigated by Bywater-Reyes et al. (2015) (Q_2=80 m^3 s^{-1}; Q_{10}=460 m^3 s^{-1}) and the plants uprooted under 0.30 m scouring condition. For the measured plants, we calculated the minimum, median and maximum of uprooting probability according to the corresponding velocities as output of the numerical simulation carried out by

Bywater-Reyes et al. (2015) for the two investigated return periods. Figure 5.11-b) shows the uprooting probability $P_\tau(t = \hat{T}_\xi)$ versus the threshold ξ for different values of the unknown variable L_e for the Santa Maria River. The critical erosion length $L_e = 0.33$ m used in figure 5.11-b) was calculated according to the model proposed in section 4.2 for the mechanically uprooted plants for which measurements of intact root (i.e., main root length) were available. Uprooting probability for measured plants are shown as boxplots. As a final result of our analysis, we found a very good agreement between measured and modelled uprooting probability for both the flow discharges. Therefore, this supports the validity of the analysis and the robustness of the approach.

5.5 Conclusion

We linked the uprooting probability given by the stochastic model of Perona and Crouzy (2018) to the return period of flood events, calculated using the Peak Over Threshold method on a Compound Poisson Process. We proposed a simple approach to calculate a reference statistically averaged event for a given return period and its application on the stochastic model for the uprooting probability.

Our analysis has been carried out for one single flood event and returns the probability of uprooting associated to characteristic flood/erosion events of assigned return period. Riparian vegetation may withstand many more erosion events in its life. This suggests that the interval between consecutive peak events and the ability for riparian species to recover and grow in this interval play a fundamental role in the evolution of water driven patterns, both from the biological and the morphological point of view (Edmaier et al., 2015; Perona and Crouzy, 2018; Bertagni et al., 2018) (see also section 3.3). For this reason, the role of intertime between consecutive flood events and the cumulative effects of these events should be further investigated.

Nevertheless, the results suggest that the critical erosion length L_e and the average frequency of peak events λ_P are the key parameters to define the uprooting probability of riparian vegetation in a given river basin. Yet, this study confirms that long time scale interactions between river hydro-morphology and riparian vegetation are fundamental to shape the riverine environment (Solari et al., 2016; Bywater-Reyes et al., 2015). For a given hydrological regime, the mechanisms at the base of such interactions may be key to select species according to their ability to survive in water-driven environments. In a climate change scenario, invasive riparian plants can take advantage of these interactions, leading to colonisation of new fluvial landforms and suppression of local species.

Chapter 6

Conclusions and recommendations

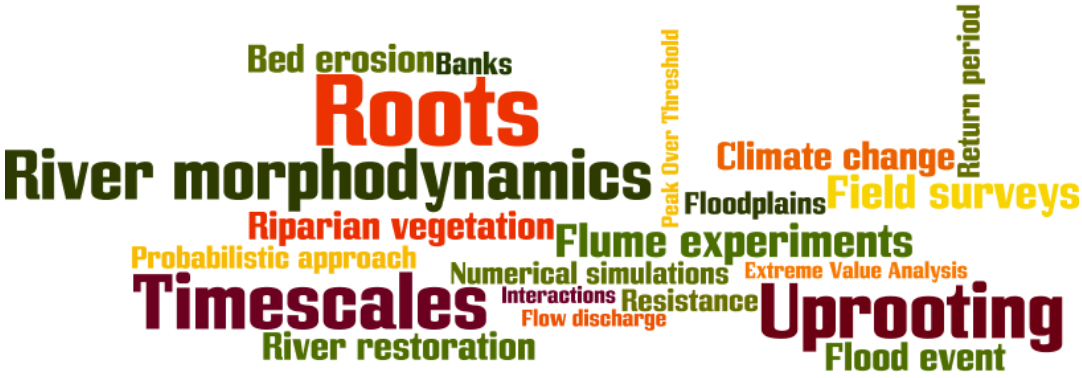

FIGURE 6.1: PhD thesis word cloud (created with Wordle http://www.wordle.net).

This chapter summarises the main findings of this PhD research and includes some recommendations.

6.1 Main conclusions

The results of this PhD research are here presented as answers to the research questions (section 1.3).

- **What are the growth and mortality timescales of riparian vegetation when dynamics is altered by flood events?**

The dynamics of the riparian vegetation living on the floodplains and near the main channel is altered by periodical inundations and flood events. The alterations induced by flow are responsible for the selection of species able to withstand such events and to adapt their biological dynamics to such perturbations. Generally, vegetation colonises exposed bare riverbed and deposits during low flow periods, whereas it dies due to uprooting during high stage events. Such processes happen during different periods and last differently. The connection between these two processes was addressed in this research by carrying out an analysis on river reaches showing downstream narrowing width (chapter 3).

Indeed, due to the continuously narrowing cross-section, water flow is, in turn, continuously accelerated, therefore its capacity to uproot vegetation similarly increases. As a result, it emerges a particular bio-morphological pattern, characterised by a vegetation front downstream which plants are likely to be removed. This front has an exact position depending on both flow and plant properties, that can be studied considering an average flow discharge at the steady state. Therefore, the fixed planform configuration is key to carry out the analysis.

35 rivers (plus 2 as validating cases) with various characteristics of grain size distribution, geometry, hydrological regime and vegetation cover were analysed. The results show that similar vegetation covers can adapt to the different hydrological regimes and morphological conditions (different rivers within the same vegetation Group, see tables 3.1 and A.1). However, the different rivers, for a given Group, agree upon the return period of the flood event governing the equilibrium at river reach. The return period of such events are related to the averaged growth rate of the plants colonising the lateral floodplains. As a consequence, biological properties like diameter and age at maturity of plants able to survive in a given fluvial environment are related to the magnitude of extreme flood events governed by the hydrological regime of that specific river (see figure 3.10).

Additionally, similar considerations can be done between the average decay rate and the duration of a flood event (see figure 3.9). As a matter of fact, plant removal requires time to occur (Type II versus Type I uprooting, see section 4.4.1). Therefore, the duration of the flood event is key to provide the required erosion to uproot established vegetation.

The conclusion is that duration and return period of flood events drive the survival of plants in fluvial environments, according to their specific properties.

- **What are the most important factors affecting vegetation mortality due to flow uprooting?**

Uprooting of flexible vegetation is the result of imbalance between the drag action due to flow and turbulence and the resisting force exerted by root systems. Additionally, buoyancy under fully submerged condition exerts an upward vertical action that roots have to counterbalance. The developed model able to predict the critical values of flow and scour depth for juvenile riparian seedling uprooting (section 4.2) accounts for all the three actions.

Nevertheless, for the seedlings tested in flume experiments (both *Avena sativa* and *Salix purpurea*) and the plants measured in the field, neglecting the vertical force due to buoyancy increases the critical erosion length L_e by some millimetres only. Such amount results negligible if compared to the critical erosion length L_e which is in the order of some centimetres. This is mainly related to the tiny size of the seedlings, particularly in the case of herbaceous species (e.g., *Avena sativa*). As a consequence, the buoyancy force can be legitimately neglected for small seedlings. On the contrary, for more mature plants with well developed root and branch systems, the contribution of the whole submerged volume may not be negligible.

At the same time, the higher number of branches and roots enhances both the drag and the resisting force. Indeed, the former increases due to the much larger leaf surface, while the latter because of the longer root length. As a matter of fact, leaves represent the main surface where bed shear stresses act, if compared to the plant stem area, which is primary for leaf-less or poorly leafy species only (e.g., *Avena sativa*). Furthermore, longer roots of more mature plants can exert higher resisting force for two main reasons: as first, the longer root system increases the soil-root contact surface; secondly, deeper roots reach soil layers with higher shear strength. As a consequence, pioneer riparian species exhibit root systems of the types I and III according to the classification of Cannon (see figure 2.8 for the classification and figure 4.8 for some examples of *Salix purpurea* root system).

To conclude, leaf surface and flow velocity are responsible for the primary uprooting action, whereas root depth and soil properties control the resisting force. However, neglecting the additional terms must be taken into account on a case-by-case basis, due to the different plant properties among species and among plants within the same species. Furthermore, randomness is naturally present in the uprooting process both regarding the turbulent flow, sediment transport and soil strength and the above- and below- ground properties of the riparian vegetation. Therefore, taking into account stochasticity in the prediction of time to uprooting is relevant.

- **What is the role of huge flood events (e.g., with return period higher than decades) on the dynamics of riparian vegetation?**

Seed dispersal, sprouting, recruitment, growth and mortality of riparian vegetation are biological processes intrinsically related to river dynamics. Vegetation establishment strongly depends on the presence of newly created barebed deposits and the availability of nutrients and water during low-flow periods. Therefore, seed dispersal, sprouting and recruitment are mainly dependent on flow discharges with low return period. Due to the seasonality of most riparian species, a 1-2 years return period flood can be assumed as the flow discharge governing the establishment of such vegetation.

On the contrary, the dynamics of already established vegetation is governed by higher return period floods. Particularly, for the species analysed in this work (see table 3.1), averaged growth rates are mainly correlated to flood events with a minimum return period of nearly 20 years. Different vegetation covers are related to different return periods, thus supporting the thesis that river hydrological regime, along with sediment properties, is responsible for the selection of species able to grow in such riverine environments. It follows that vegetation cover is differently selected along the fluvial stream, similarly to grain sorting processes (e.g., downstream fining).

Long term average (i.e., steady state) vegetation cover is the result of a continuous adaptation to frequent flood events. Conversely, vegetation selection takes place during high flood events because of removal after bed erosion. Duration and magnitude of flood events are the main factors governing the uprooting process of established vegetation. Particularly, flow discharges with return period higher than the timescale of growth rate (i.e., larger than 50 years) are responsible for the almost resetting of the juvenile riparian vegetation. Such flood events can be withstood by mature vegetation only, provided proper root system developed. The complete removal of young established plants enhances vegetation dynamics in floodplain areas and increases competition among pioneer species in colonising renovated riparian zones. Furthermore, when deposited on floodplains areas, the removed vegetation material contributes to carbon sequestration and provides nutrients for the new plants. As a result, pioneer species colonisation is boosted, leading to new vegetation cover.

As a final conclusion, flood events with high return period are responsible for significant changes in the morphological patterns and the biological components, by shifting the vegetation state through shock dynamics, by renewing the established vegetation cover and by promoting the competitive mechanisms among pioneer species.

6.2 Recommendations

Vegetation removal due to the combined action of flow and scouring around plant plays a key role in the evolution of rivers. As the presence of vegetation affects flow field, sediment transport and soil properties, its removal acts in the opposite manner, altering the dynamics of uncovered deposits and floodplains. Therefore, taking into account vegetation dynamics is essential to predict morphodynamic evolution at the timescale of a single flood event, by accounting for plant removal, and in the long-term by considering recruitment, establishment and growth. Additionally, due to the related interactions of biological components and hydro-morphological processes, the modelling of their mutual feedbacks must be implemented in numerical tools at the proper spatial and temporal scales. Furthermore, the choice of vegetation properties appears to be crucial, with regards to both the growing characteristics and the mortality rate.

Nowadays, climate change is ascertained to be one of the biggest responsible for increasing frequency and magnitude of flood events. Beyond the related issues to flood risk assessment and management, climate change enhances the alterations of hydrological regime of fluvial streams. As a result, modifications of vegetation cover along riverbanks and in the riparian zones are promoted, due to colonisation of alien species able to survive in such altered environments. Various studies have already focused on this aspect in North American rivers, by proving the suppression of native Salicaceae by alien Tamaricaceae species. Similar trend is currently observable in temperate climate European rivers. Therefore, river management must pay attention to design strategies able to sustain the survival of local species.

River restoration has to deal with riparian vegetation as well. The design of fluvial works aiming to re-naturalise river flow has to take into account either the future colonisation or the seeding and implanting of riparian vegetation. In the first case, randomly location of pioneer plants during the first stages of the colonisation process may lead to alteration and changes in the designed morphology. In the second case, the choice of proper vegetation species, along with their implanting at the field site, may enhance their chances to survive and compete with alien species and, as a final result, the success of the whole river restoration project.

Appendices

A

River and vegetation data

This appendix contains complete data about river cross sections and vegetation cover and properties for the analysis carried out in Chapter 3.

TABLE A.1: Summary of the data collected for the 35 river cross-sections analysed in Chapter 3. Group refers to similar characteristics of vegetation cover.

Group	ID	Site[a] (Ref.)	Latitude [° ′ ″]	Longitude [° ′ ″]	B_f [m]	S [‰]	D_{50} [mm]	D_{90} [mm]	Q_s [$m^3\,d^{-1}$]	Vegetation characteristics and parameters Species	Cover [%]	$\overline{\alpha}_g$ [$cm^2\,y^{-1}$]	$\overline{\phi}_v^m$ [$10^{-3}\ m^{-2}$]
1	1	Clearwater 1 (5)(17)(21)(22) (26)(28)(29)	46° 29′ 17.01″ N	116° 15′ 41.91″ W	120	1.57	58.8	114.2	200.7	Balsam poplar Other willows Sandbar willow	64% 33% 3%	79.94	35.46
	2	Clearwater 2 (5)(17)(21)(22) (26)(28)(29)	46° 31′ 16.97″ N	116° 40′ 08.12″ W	270	1.29	44.4	111.3	200.7	Balsam poplar Other willows Sandbar willow	64% 33% 3%	79.94	35.46
	3	Clearwater 3 (5)(17)(21)(22) (26)(28)(29)	46° 29′ 19.63″ N	116° 44′ 28.74″ W	243	1.29	44.4	111.3	200.7	Balsam poplar Other willows Sandbar willow	64% 33% 3%	79.94	35.46
	16	Salmon (5)(20)(21)(22)(28)(29)	44° 15′ 14.13″ N	114° 41′ 00.59″ W	56	3.40	104	396	12.96	Douglas fir. Sandbar willow	77% 23%	309.6	44.14
	32	Yellowstone 1 (5)(17)(18)(21) (22)(28)(29)	47° 07′ 42.86″ N	104° 42′ 05.16″ W	675	0.75	57	160	1382	Plains cotton. Russian olive Sandbar willow	79% 15% 6%	369.3	15.17
	33	Yellowstone 2 (5)(17)(18)(21) (22)(28)(29)	47° 30′ 14.49″ N	104° 15′ 22.42″ W	577	0.36	57	160	1382	Plains cotton. Russian olive Peach. willow Sandbar willow	78% 14% 5% 3%	375.6	11.56
	34	Yellowstone 3 (5)(17)(18)(21) (22)(28)(29)	47° 35′ 27.12″ N	104° 12′ 36.41″ W	485	0.36	57	160	1382	Plains cotton. Russian olive Peach. willow Sandbar willow	78% 14% 5% 3%	375.6	11.56
	35	Yellowstone 4 (5)(17)(18)(21) (22)(28)(29)	47° 37′ 36.64″ N	104° 10′ 07.75″ W	535	0.36	57	160	1382	Plains cotton. Russian olive Peach. willow Sandbar willow	78% 14% 5% 3%	375.6	11.56

[a]Numbers, when present, refer to different reaches in the same river.
List of references at the end of the table

TABLE A.1: Summary of collected data for the 35 cross-sections. Group refers to similar characteristics of vegetation cover.

Group	ID	Site[a] (Ref.)	Latitude [° ′ ″]	Longitude [° ′ ″]	B_f [m]	S [‰]	D_{50} [mm]	D_{90} [mm]	Q_s [m^3 d^{-1}]	Vegetation characteristics and parameters Species	Cover [%]	$\overline{\alpha}_g$ [cm^2 y^{-1}]	$\overline{\phi}_v^m$ [10^{-3} m^{-2}]
2	14	Rio Grande 1 (5)(10)(17)(22) (24)(28)(29)	35° 16′ 13.96″ N	106° 35′ 35.41″ W	80	0.83	0.462	1.125	2247	Fremont cotton. Salt cedar Russian olive Sandbar willow	52% 41% 6% 1%	1.4090	63.56
	15	Rio Grande 2 (5)(10)(17)(22) (24)(28)(29)	35° 05′ 53.99″ N	106° 41′ 35.28″ W	131	0.83	0.462	1.125	2247	Fremont cotton. Salt cedar Russian olive Sandbar willow	52% 41% 6% 1%	444.3	63.56
	17	San Juan 1 (5)(10)(16)(17)(22)(28)	36° 43′ 57.83″ N	108° 14′ 58.31″ W	95	4.10	40	100	28.51	Plains cotton. Russian olive Salt cedar	42% 29% 29%	1.362	50.00
	18	San Juan 2 (5)(10)(16)(17)(22)(28)	36° 43′ 23.14″ N	108° 18′ 53.63″ W	92	4.10	40	100	28.51	Plains cotton. Russian olive Salt cedar	42% 29% 29%	429.5	50.00
	19	San Juan 3 (5)(10)(16)(17)(22)(28)	36° 46′ 22.16″ N	108° 39′ 28.03″ W	91	1.45	90	240	28.51	Salt cedar Russian olive Plains cotton.	43% 36% 21%	291.7	72.59
	20	San Juan 4 (5)(10)(16)(17)(22)(28)	36° 47′ 12.68″ N	108° 41′ 38.69″ W	117	1.45	90	240	28.51	Salt cedar Russian olive Plains cotton.	43% 36% 21%	291.7	72.59

[a]Numbers, when present, refer to different reaches in the same river.
List of references at the end of the table

TABLE A.1: Summary of collected data for the 35 cross-sections. Group refers to similar characteristics of vegetation cover.

Group	ID	Site[a] (Ref.)	Latitude [° ′ ″]	Longitude [° ′ ″]	B_f [m]	S [‰]	D_{50} [mm]	D_{90} [mm]	Q_s [$m^3\,d^{-1}$]	Vegetation characteristics and parameters Species	Cover [%]	$\overline{\alpha}_g$ [$cm^2\,y^{-1}$]	$\overline{\phi}_v^m$ [$10^{-3}\ m^{-2}$]
3	4	Colorado 1 (17)(20)(22)(28)(29)	39° 30′ 59.02″ N	107° 50′ 27.87″ W	237	2.71	58	90	247.5	Salt cedar Other willows Box elder	56% 30% 14%	38.47	129.3
	5	Colorado 2 (17)(20)(22)(28)(29)	39° 18′ 40.61″ N	108° 13′ 30.36″ W	346	2.71	58	90	247.5	Salt cedar Other willows Box elder	56% 30% 14%	38.47	129.3
	6	Colorado 3 (17)(20)(22)(28)(29)	39° 03′ 35.67″ N	108° 26′ 36.66″ W	266	2.71	58	90	247.5	Salt cedar Other willows Box elder	56% 30% 14%	38.47	129.3
	7	Endrik (11)(13)(15)(23)(25)	56° 03′ 19.78″ N	004° 27′ 10.80″ W	22	1.44	28.9	57.3	524.1	Goat willow Common alder Scots pine	66% 17% 17%	43.84	114.3
	8	Feshie (4)(11)(13)(15)(23)	57° 05′ 32.40″ N	003° 54′ 11.34″ W	79	9.62	54	90	20.82	Goat willow Common alder Scots pine	66% 17% 17%	43.84	114.3
	31	Yampa (2)(3)(5)(12)(22)(28)	40° 27′ 40.54″ N	108° 25′ 29.27″ W	103	1.26	34	82	359.1	Sandbar willow Box elder	82% 18%	37.53	124.2
4	11	Little Snake 1 (2)(5)(14)(17)(22)(28)	40° 35′ 16.76″ N	108° 23′ 02.08″ W	185	1.23	48.5	87.0	857.5	Other willows Russian olive	60% 40%	147.0	97.40
	12	Little Snake 2 (2)(5)(14)(17)(22)(28)	40° 53′ 06.27″ N	108° 07′ 29.89″ W	208	1.23	48.5	87.0	857.5	Other willows Russian olive	60% 40%	147.0	97.40
5	23	Snake 1 (5)(20)(21)(22)(28)	46° 02′ 21.87″ N	116° 55′ 48.00″ W	248	1.16	54.0	90.0	172.8	Netl. hackberry	100%	163.7	77.33
	24	Snake 2 (5)(20)(21)(22)(28)	46° 18′ 26.35″ N	117° 00′ 28.75″ W	380	0.47	54.0	90.0	172.8	Netl. hackberry	100%	163.7	77.33

[a]Numbers, when present, refer to different reaches in the same river.
List of references at the end of the table

TABLE A.1: Summary of collected data for the 35 cross-sections. Group refers to similar characteristics of vegetation cover.

Group	ID	Site[a] (Ref.)	Latitude [° ′ ″]	Longitude [° ′ ″]	B_f [m]	S [‰]	D_{50} [mm]	D_{90} [mm]	Q_s [$m^3\,d^{-1}$]	Vegetation characteristics and parameters Species	Cover [%]	$\overline{\alpha}_g$ [$cm^2\,y^{-1}$]	$\overline{\phi}_v^m$ [$10^{-3}\ m^{-2}$]
6	13	NF Clearwater (6)(7)(10)(19)(22)	46° 45′ 04.96″ N	115° 31′ 12.53″ W	96	7.94	95	282	26.87	Western cedar Box elder Other willows	79% 13% 8%	163.7	35.11
	21	Selway 1 (5)(12)(17)(20)(21) (22)(27)(28)(29)	46° 04′ 57.73″ N	115° 25′ 19.69″ W	109	2.60	24	131	70.50	Western cedar Ponderosa pine Other willows	59% 22% 19%	166.8	18.40
	22	Selway 2 (5)(12)(17)(20)(21) (22)(27)(28)(29)	46° 05′ 29.02″ N	115° 32′ 15.49″ W	207	2.60	24	131	70.50	Western cedar Ponderosa pine Other willows	59% 22% 19%	166.8	18.40
7	9	Johnson (5)(20)(21)(22)(28)	44° 52′ 33.17″ N	115° 30′ 26.12″ W	45	5.02	190	430	0.691	Grey alder Red osier dogw.	57% 43%	70.64	351.9
	25	SF Salmon 1 (5)(20)(21)(22)(28)	44° 57′ 08.84″ N	115° 44′ 07.69″ W	54	2.50	38	113	34.56	Grey alder Red osier dogw.	57% 43%	70.64	351.9
	26	SF Salmon 2 (5)(20)(21)(22)(28)	44° 57′ 03.45″ N	115° 44′ 03.38″ W	40	2.50	38	113	34.56	Grey alder Red osier dogw.	57% 43%	70.64	351.9

[a]Numbers, when present, refer to different reaches in the same river.
List of references at the end of the table

TABLE A.1: Summary of collected data for the 35 cross-sections. Group refers to similar characteristics of vegetation cover.

Group	ID	Site[a] (Ref.)	Latitude [° ′ ″]	Longitude [° ′ ″]	B_f [m]	S [‰]	D_{50} [mm]	D_{90} [mm]	Q_s [$m^3\,d^{-1}$]	Vegetation characteristics and parameters Species	Cover [%]	$\overline{\alpha}_g$ [$cm^2\,y^{-1}$]	$\overline{\phi}_v^m$ [$10^{-3}\ m^{-2}$]
8	10	Kander (6)(7)(10)(19)(22)	46° 36′ 17.00″ N	007° 39′ 56.36″ E	88	13.3	76	287	3654	Norway spruce Scots pine Grey alder	46% 31% 23%	233.4	48.35
	27	Tay (1)(8)(9)(11)(22)(23)	56° 29′ 16.19″ N	003° 25′ 35.11″ W	166	2.19	1.14	5	153.2	Common alder Downy birch Scots pine	40% 40% 20%	59.60	49.53
	28	Virgin (5)(20)(21)(22)(28)	36° 53′ 33.21″ N	113° 55′ 09.95″ W	27	2.86	25	75	34.56	Salt cedar Fremont cotton. Black willow	62% 23% 15%	219.8	95.28
	29	Wind 1 (5)(20)(22)(28)	43° 25′ 09.62″ N	109° 19′ 56.54″ W	192	3.34	22	75	267.8	Water birch Spruce Narrow. cotton.	48% 36% 16%	41.31	67.27
	30	Wind 2 (5)(20)(22)(28)	43° 18′ 57.13″ N	109° 08′ 00.02″ W	105	3.34	22	75	267.8	Water birch Spruce Narrow. cotton.	48% 36% 16%	41.31	67.27

[a]Numbers, when present, refer to different reaches in the same river

(1) Al-Ansari and McManus (1979); (2) Andrews (1980); (3) Andrews (1984); (4) Ashworth and Ferguson (1989); (5) Auble et al. (2012); (6) BAFU Data (2017); (7) BAFU GeoData (2017); (8) Bates et al. (2004); (9) Bryant and Gilvear (1999); (10) Charlton et al. (1978); (11) Claessens et al. (2010); (12) Elliott and Anders (2004); (13) Enescu et al. (2016); (14) FLO Engineering (1994); (15) Gilvear et al. (2000); (16) Heins et al. (2004); (17) Hoag (2005); (18) Holnbeck (2005); (19) Jud (2009); (20) Mueller et al. (2005); (21) Mueller and Pitlick (2013); (22) Little and Viereck (1971); (23) National River Flow Archive (2017); (24) Novak (2006); (25) Piedra (2010); (26) Sharma and Parton (2007); (27) Smith (1999); (28) Water Data for the Nation (2017); (29) Warner and Hendrix (1984)

B

Suspended load and Einstein's integrals

This appendix explains the Van Rijn's model for suspended load (van Rijn, 1984) in Chapter 5. Explanation of the term $I(q, D_{50})$ in Eq. (5.3) is given, as well.

In the case of suspended load, sediment transport rate per unit width can be modelled, according to Einstein (1950), as :

$$q_{SL} = 11.6\, c_a\, \delta_a\, u_* \left(\log \left[30.2 \frac{Y}{\epsilon} \right] I_1 + I_2 \right) \tag{B.1}$$

where c_a is the reference concentration of suspended sediment; δ_a is the reference level for the suspended load; u_* is the shear velocity; Y is the flow depth; ϵ is the absolute roughness of the channel bed; I_1 and I_2 are two quantities given by the following relations (Einstein, 1950).

$$I_1 = 0.216 \frac{1}{\Delta_a} \left(\frac{\Delta_a}{1-\Delta_a} \right)^Z \int_{\Delta_a}^{1} \left(\frac{1-w}{w} \right)^Z dw \tag{B.2}$$

$$I_2 = 0.216 \frac{1}{\Delta_a} \left(\frac{\Delta_a}{1-\Delta_a} \right)^Z \int_{\Delta_a}^{1} \left(\frac{1-w}{w} \right)^Z \log[w]\, dw \tag{B.3}$$

Therein, Z is the Rouse number, w is a dummy variable for integration and Δ_a is the dimensionless reference level given by:

$$\Delta_a = \frac{\delta_a}{Y} \tag{B.4}$$

where the reference level, δ_a, can be calculated as:

$$\delta_a = \max[0.01\, Y\, ,\, \epsilon] \tag{B.5}$$

The absolute roughness, ϵ, is defined as:

$$\epsilon = \begin{cases} 3\,D_{50} + 1.1\,A_{vr}\left(1 - \exp\left[-25\frac{A_{vr}}{7.3Y}\right]\right) & \frac{Y-Y_{cr}}{Y_{cr}} \leq 25 \\ 3\,D_50 & \frac{Y-Y_{cr}}{Y_{cr}} > 25 \end{cases} \tag{B.6}$$

where Y_{cr} is the critical water depth for incipient motion of sediment as bedload ($Y_{cr} = Y|_{\tau^*=\tau^*_{cr}}$) and A_{vr} is a length scale given by:

$$A_{vr} = 0.11\,Y\left(\frac{D_{50}}{Y}\right)^{\frac{3}{10}}\left(1 - \exp\left[-0.5\frac{Y-Y_{cr}}{Y_{cr}}\right]\right)\left(25 - \frac{Y-Y_{cr}}{Y_{cr}}\right) \tag{B.7}$$

The reference concentration, c_a, in Eq. (B.1) can be calculated as:

$$c_a = 0.015\,\frac{D_{50}}{\delta_a}\left(\frac{\tau^* - \tau^*_{SL}}{\tau^*_{SL}}\right)^{\frac{3}{2}} R_{ep}^{-2/10} \tag{B.8}$$

Lastly, by including Eq. (B.8) in Eq. (B.1), we obtain the coefficient $\alpha_{SL} = 0.174 = 11.6 \cdot 0.015$, as shown in Eq. (5.5). Additionally, reorganisation of terms and calculation of the Shields parameters τ^* and τ^*_{SL} as functions of flow discharge q and Q_{cr}, respectively, yields to Eq. (5.3) in the case of suspended load (a_{ST}=1) with the quantity $I(q, D_{50})$ given by:

$$I(q, D_{50}) = \log\left[30.2\frac{Y}{\epsilon}\right] I_1(q, D_{50}) + I_2(q, D_{50}) \tag{B.9}$$

C

Peak Over Threshold probability

This appendix contains the mathematical derivation of Peak Over Threshold analysis and return period evaluation presented in Chapter 5. The calculations were made according to the theory developed by Zelenhasic (1970) and the more recent works of Castillo (2012) and Solari and Losada (2012).

Take the Compound Poisson Process of a variable (e.g., the flow discharge $q(t)$) with frequency λ_P and integral temporal scale τ_P into account, similarly to the realisation shown in figure 5.2. On this process, we perform an extreme value analysis to assess the return period $T(\xi)$ of events characterised by low frequency and high magnitude, using the Peak Over Threshold methodology. Once set a value for the threshold ξ, it is possible to calculate the average frequency for which a shot in the process upcrosses such threshold. To the aim of the Peak Over Threshold, it is obvious to consider only high values of the threshold ξ. In this case (i.e., $\xi \to \infty$), the overcoming of the threshold occurs as a new Poisson Process with frequency λ'_P, which is the reciprocal of the average time between overcoming pulses. This average time can be simply calculated as the sum of the average time, T^+_ξ (Eq. (5.8)), above, and, T^-_ξ (Eq. (5.9)), below the threshold ξ. The resulting equation for λ'_P reads:

$$\lambda'_P = \frac{1}{T^+_\xi + T^-_\xi} \tag{C.1}$$

which can be then simplified to

$$\lambda'_P = \frac{\mathrm{e}^{-\phi}\, \phi^{\beta_P}}{\tau_P\, \Gamma[\beta_P]} \tag{C.2}$$

as presented in Section 5.2.2.

With the new frequency λ'_P, the number m of shots ($\zeta(t)$) in a generic period τ can be retrieved from the Poisson distribution:

$$p(m) = \frac{(\lambda'_P\, \tau)^m}{m!} \mathrm{e}^{-\lambda'_P\, \tau} \tag{C.3}$$

Recalling that $\beta_P = \lambda_P \tau_P$, the distribution of the maxima above the threshold ξ is the truncated distribution of $p(q)$ (Eq. (5.2)), whose cumulative value, by accounting for P_ξ^+ relation (see Section 5.2.2), reads:

$$P_\xi^- = \frac{\Gamma[\beta_P] - \Gamma[\beta_P, \phi]}{\Gamma[\beta_P]} = 1 - \frac{\Gamma[\beta_P, \phi]}{\Gamma[\beta_P]} = 1 - P_\xi^+ \tag{C.4}$$

Therefore, the cumulative distribution of m events above the threshold ξ is given by $\left(P_\xi^-\right)^m$. Then, by taking the probability of occurrence $p(m)$ into account, the the probability P_ξ of events higher than the threshold ξ corresponds to the cumulative distribution of the maximum of m shots above the threshold, according to:

$$P_\xi = \sum_{m=0}^{\infty} p(m) \left(P_\xi^-\right)^m \tag{C.5}$$

By substituting Eq. (C.3), we obtain:

$$P_\xi = \sum_{m=0}^{\infty} \frac{(\lambda'_P \tau)^m}{m!} \mathrm{e}^{-\lambda'_P \tau} \left(P_\xi^-\right)^m \tag{C.6}$$

Then, we reorganise the right-hand side terms, so Eq. (C.6) yields:

$$P_\xi = \mathrm{e}^{-\lambda'_P \tau} \sum_{m=0}^{\infty} \frac{\left(\lambda'_P P_\xi^- \tau\right)^m}{m!} \tag{C.7}$$

Now, by remembering that

$$\sum_{m=0}^{\infty} \frac{j^m}{m!} = \mathrm{e}^j \tag{C.8}$$

we can first simplify Eq. (C.7) to

$$P_\xi = \mathrm{e}^{-\lambda'_P \tau} \, \mathrm{e}^{\lambda'_P P_\xi^- \tau} \tag{C.9}$$

and then to

$$P_\xi = \mathrm{e}^{\left(-\lambda'_P \tau + \lambda'_P P_\xi^- \tau\right)} = \mathrm{e}^{-\lambda'_P \tau \left(1 - P_\xi^-\right)} \tag{C.10}$$

From Eq. (C.10), by accounting for Eq. (C.4) and fixing $\tau = 1$ with measuring unit equal to the reciprocal of that of the frequency λ_P, we come to the final relation for the Peak Over Threshold probability P_ξ :

$$P_\xi = \mathrm{e}^{-\lambda'_P \tau \left(1 - P_\xi^-\right)} = \mathrm{e}^{-\lambda'_P P_\xi^+} \tag{C.11}$$

which is briefly presented as Eq. (5.7) in Section 5.2.2.

References

Aberle, J. & Järvelä, J. (2013). Flow resistance of emergent rigid and flexible floodplain vegetation. *Journal of Hydraulic Research*, *51*(1), 33–45.

Abramowitz, M. & Stegun, I. A. (1965). *Handbook of mathematical functions: with formulas, graphs, and mathematical tables*. Courier Corporation.

Al-Ansari, N. & McManus, J. (1979). Fluvial sediments entering the Tay Estuary: sediment discharge from the River Earn. *Scottish Journal of Geology*, *15*(3), 203–216.

Andrews, E. D. (1980). Effective and bankfull discharges of streams in the Yampa River basin, Colorado and Wyoming. *Journal of Hydrology*, *46*(3-4), 311–330.

Andrews, E. D. (1984). Bed-material entrainment and hydraulic geometry of gravel-bed rivers in Colorado. *Geological Society of America Bulletin*, *95*(3), 371–378.

Arcement, G. J. & Schneider, V. R. (1989). *Guide for selecting Manning's roughness coefficients for natural channels and flood plains*. US Government Printing Office Washington, DC.

Armanini, A., Cavedon, V., & Righetti, M. (2015). A probabilistic/deterministic approach for the prediction of the sediment transport rate. *Advances in Water Resources*, *81*, 10–18.

Arner, S. L., Woudenberg, S., Waters, S., Vissage, J., MacLean, C., Thompson, M., & Hansen, M. (2001). National algorithms for determining stocking class, stand size class, and forest type for Forest Inventory and Analysis plots. *Internal Rep. Newtown Square, PA: US Department of Agriculture, Forest Service, Northeastern Research Station. 10p*.

Ashworth, P. J. & Ferguson, R. I. (1989). Size-selective entrainment of bed load in gravel bed streams. *Water Resources Research*, *25*(4), 627–634.

Auble, G. T., Friedman, J. M., Shafroth, P. B., Merigliano, M. F., & Scott, M. L. (2012). Woody riparian vegetation near selected streamgages in the western United States. *US Geological Survey Data Series*, *Data series: 708*.

BAFU Data. (2017). Erhebung von Daten zum Umweltzustand des Bundesamtes für Umwelt; https://www.bafu.admin.ch/bafu/de/home/zustand/daten/umweltdaten.html. Bern (CH): Bundesamt für Umwelt BAFU.

BAFU GeoData. (2017). Verfügbare Geodaten des Bundesamtes für Umwelt; https://www.bafu.admin.ch/bafu/de/home/zustand/daten/geodaten.html. Bern (CH): Bundesamt für Umwelt BAFU.

Bailey, P. H., Currey, J., & Fitter, A. (2002). The role of root system architecture and root hairs in promoting anchorage against uprooting forces in *Allium cepa* and root mutants of *Arabidopsis thaliana*. *Journal of Experimental Botany*, *53*(367), 333–340.

Bankhead, N. L., Thomas, R. E., & Simon, A. (2017). A combined field, laboratory and numerical study of the forces applied to, and the potential for removal of, bar top vegetation in a braided river. *Earth Surface Processes and Landforms*, *42*(3), 439–459.

Baptist, M., Babovic, V., Rodríguez Uthurburu, J, Keijzer, M, Uittenbogaard, R., Mynett, A, & Verwey, A. (2007). On inducing equations for vegetation resistance. *Journal of Hydraulic Research*, *45*(4), 435–450.

Bärenbold, F., Crouzy, B., & Perona, P. (2016). Stability analysis of ecomorphodynamic equations. *Water Resources Research*, *52*(2), 1070–1088.

Barfield, B., Tollner, E., & Hayes, J. (1979). Filtration of sediment by simulated vegetation I. Steady-state flow with homogeneous sediment. *Transactions of the ASAE*, *22*(3), 540–0545.

Bates, C., Moore, C., Malthus, T, Mair, J., & Karpouzli, E. (2004). Broad scale mapping of habitats in the Firth of Tay and Eden Estuary, Scotland. *Scottish Natural Heritage Comissioned Report*, *7*.

Bennett, S. J., Pirim, T., & Barkdoll, B. D. (2002). Using simulated emergent vegetation to alter stream flow direction within a straight experimental channel. *Geomorphology*, *44*(1-2), 115–126.

Bennett, S. J., Wu, W., Alonso, C. V., & Wang, S. S. (2008). Modeling fluvial response to in-stream woody vegetation: implications for stream corridor restoration. *Earth Surface Processes and Landforms: The Journal of the British Geomorphological Research Group*, *33*(6), 890–909.

Bertagni, M. B., Perona, P., & Camporeale, C. (2018). Parametric transitions between bare and vegetated states in water-driven patterns. *Proceedings of the National Academy of Sciences*, *115*(32), 8125–8130.

Bertoldi, W, Gurnell, A., & Drake, N. (2011). The topographic signature of vegetation development along a braided river: results of a combined analysis of airborne lidar, color air photographs, and ground measurements. *Water Resources Research*, *47*(6).

Bertoldi, W., Siviglia, A., Tettamanti, S., Toffolon, M., Vetsch, D., & Francalanci, S. (2014). Modeling vegetation controls on fluvial morphological trajectories. *Geophysical Research Letters*, *41*(20), 7167–7175.

Botter, G, Porporato, A, Daly, E, Rodriguez-Iturbe, I, & Rinaldo, A. (2007). Probabilistic characterization of base flows in river basins: Roles of soil, vegetation, and geomorphology. *Water Resources Research*, *43*(6).

Braudrick, C. A., Dietrich, W. E., Leverich, G. T., & Sklar, L. S. (2009). Experimental evidence for the conditions necessary to sustain meandering in coarse-bedded rivers. *Proceedings of the National Academy of Sciences*, *106*(40), 16936–16941.

Brownlie, W. R. (1981). *Prediction of flow depth and sediment discharge in open channels* (tech. rep. No. No. KH-R-43A). Keck Laboratory, California Institute of Technology.

Bryant, R. G. & Gilvear, D. J. (1999). Quantifying geomorphic and riparian land cover changes either side of a large flood event using airborne remote sensing: River Tay, Scotland. *Geomorphology*, *29*(3-4), 307–321.

Burylo, M, Rey, F, Roumet, C, Buisson, E, & Dutoit, T. (2009). Linking plant morphological traits to uprooting resistance in eroded marly lands (Southern Alps, France). *Plant and Soil*, *324*(1-2), 31.

Burylo, M., Rey, F., Mathys, N., & Dutoit, T. (2012). Plant root traits affecting the resistance of soils to concentrated flow erosion. *Earth Surface Processes and Landforms*, *37*(14), 1463–1470.

Bywater-Reyes, S., Wilcox, A. C., Stella, J. C., & Lightbody, A. F. (2015). Flow and scour constraints on uprooting of pioneer woody seedlings. *Water Resources Research*, *51*(11), 9190–9206.

Calvani, G., Francalanci, S., & Solari, L. (2019a). A physical model for the uprooting of flexible vegetation on river bars. *Journal of Geophysical Research: Earth Surface*, *124*(4), 1018–1034.

Calvani, G, Perona, P, Schick, C, & Solari, L. (2019b). Biomorphological scaling laws from convectively accelerated streams. *Earth Surface Processes and Landforms*, *(accepted for publication)*.

Calvani, G., Perona, P., Zen, S., Bau', V., & Solari, L. (2019c). Return period of vegetation uprooting by flow. *Journal of Hydrology*, *578*.

Camporeale, C & Ridolfi, L. (2006). Riparian vegetation distribution induced by river flow variability: A stochastic approach. *Water Resources Research*, *42*(10).

Camporeale, C, Perucca, E., Ridolfi, L., & Gurnell, A. (2013). Modeling the interactions between river morphodynamics and riparian vegetation. *Reviews of Geophysics*, *51*(3), 379–414.

Camporeale, C., Perona, P., Porporato, A., & Ridolfi, L. (2007). Hierarchy of models for meandering rivers and related morphodynamic processes. *Reviews of Geophysics*, *45*(1), RG1001.

Cannon, W. A. (1949). A tentative classification of root systems. *Ecology*, *30*(4), 542–548.

Caponi, F & Siviglia, A. (2018). Numerical modeling of plant-root controls on gravel-bed river morphodynamics. *Geophysical Research Letters*, *45*(17), 9013–9023.

Carter Johnson, W. (2000). Tree recruitment and survival in rivers: influence of hydrological processes. *Hydrological Processes*, *14*(16-17), 3051–3074.

Casper, B. B. & Jackson, R. B. (1997). Plant competition underground. *Annual review of ecology and systematics*, *28*(1), 545–570.

Castillo, E. (2012). *Extreme value theory in engineering*. Elsevier.

Charlton, F., Brown, P., & Benson, R. (1978). *The hydraulic geometry of some gravel rivers in Britain*. Wallingford (UK): Hydraulics Research Station.

Chiew, Y.-M. & Parker, G. (1994). Incipient sediment motion on non-horizontal slopes. *Journal of Hydraulic Research*, *32*(5), 649–660.

Choi, S.-U. & Kang, H. (2004). Reynolds stress modeling of vegetated open-channel flows. *Journal of Hydraulic Research*, *42*(1), 3–11.

Claessens, H., Oosterbaan, A., Savill, P., & Rondeux, J. (2010). A review of the characteristics of black alder (*Alnus glutinosa* (L.) Gaertn.) and their implications for silvicultural practices. *Forestry*, *83*(2), 163–175.

Coppin, N. J. & Richards, I. G. (1990). *Use of vegetation in civil engineering*. London (UK): Construction Industry Research and Information Association.

Corenblit, D., Tabacchi, E., Steiger, J., & Gurnell, A. M. (2007). Reciprocal interactions and adjustments between fluvial landforms and vegetation dynamics in river corridors: a review of complementary approaches. *Earth-Science Reviews*, *84*(1), 56–86.

Corenblit, D., Steiger, J., Gurnell, A. M., & Naiman, R. J. (2009). Plants intertwine fluvial landform dynamics with ecological succession and natural selection: a niche construction perspective for riparian systems. *Global Ecology and Biogeography*, *18*(4), 507–520.

Corenblit, D., Baas, A., Balke, T., Bouma, T., Fromard, F., Garófano-Gómez, V., … Julien, F. et al. (2015). Engineer pioneer plants respond to and affect geomorphic constraints similarly along water-terrestrial interfaces world-wide. *Global Ecology and Biogeography*, *24*(12), 1363–1376.

Corless, R. M., Gonnet, G. H., Hare, D. E., Jeffrey, D. J., & Knuth, D. E. (1996). On the LambertW function. *Advances in Computational mathematics*, *5*(1), 329–359.

Coulthard, T., Hicks, D., & Van De Wiel, M. J. (2007). Cellular modelling of river catchments and reaches: advantages, limitations and prospects. *Geomorphology*, *90*(3), 192–207.

Coulthard, T., Wiel, M., Van De, J et al. (2006). A cellular model of river meandering. *Earth Surface Processes and Landforms*, *31*(1), 123–132.

Coutts, M. (1983). Root architecture and tree stability. *Plant and soil*, *71*(1), 171–188.

Cox, D. & Miller, H. (1965). *The theory of stochastic processes*. Methuen, London (UK).

Crosato, A. & Saleh, M. S. (2011). Numerical study on the effects of floodplain vegetation on river planform style. *Earth Surface Processes and Landforms*, *36*(6), 711–720.

Crouzy, B. & Perona, P. (2012). Biomass selection by floods and related timescales. Part 2: Stochastic modeling. *Advances in Water Resources*, *39*, 97–105.

Crouzy, B., Bärenbold, F., D'Odorico, P., & Perona, P. (2016). Ecomorphodynamic approaches to river anabranching patterns. *Advances in water resources*, *93*, 156–165.

Daly, E. & Porporato, A. (2006). State-dependent fire models and related renewal processes. *Physical Review E*, *74*(4), 041112.

Dargahi, B. (1990). Controlling mechanism of local scouring. *Journal of Hydraulic Engineering*, *116*(10), 1197–1214.

De Langre, E., Gutierrez, A., & Cossé, J. (2012). On the scaling of drag reduction by reconfiguration in plants. *Comptes Rendus Mécanique*, *340*(1-2), 35–40.

Diehl, R. M., Wilcox, A. C., Stella, J. C., Kui, L., Sklar, L. S., & Lightbody, A. (2017). Fluvial sediment supply and pioneer woody seedlings as a control on bar-surface topography. *Earth Surface Processes and Landforms*, *42*(5), 724–734.

Dijk, W., Teske, R, Lageweg, W., & Kleinhans, M. (2013). Effects of vegetation distribution on experimental river channel dynamics. *Water Resources Research*, *49*(11), 7558–7574.

Dijkstra, J. & Uittenbogaard, R. (2010). Modeling the interaction between flow and highly flexible aquatic vegetation. *Water Resources Research*, *46*(12).

Dittrich, A, Marek, M, & Huppmann, O. (2005). Konzept zur Abschätzung der morphodynamischen Entwicklungen in Fließgewässern und auf ihren Vorländern. *NNA-Berichte*, 153.

Dunne, T. & Leopold, L. B. (1978). *Water in environmental planning*. San Francisco, CA (USA): W. H. Freeman.

Dupuy, L., Fourcaud, T., & Stokes, A. (2005). A numerical investigation into the influence of soil type and root architecture on tree anchorage. *Plant and soil*, *278*(1-2), 119–134.

Edmaier, K, Burlando, P, & Perona, P. (2011). Mechanisms of vegetation uprooting by flow in alluvial non-cohesive sediment. *Hydrology and Earth System Sciences*, *15*(5), 1615–1627.

Edmaier, K, Crouzy, B, & Perona, P. (2014a). Flow-induced uprooting of young vegetation on river bedforms. In *River Flow 2014* (EPFL-CONF-205187, pp. 461–466). Crc Press-Taylor & Francis Group.

Edmaier, K, Crouzy, B, & Perona, P. (2015). Experimental characterization of vegetation uprooting by flow. *Journal of Geophysical Research: Biogeosciences*, *120*(9), 1812–1824.

Edmaier, K., Crouzy, B., Ennos, R., Burlando, P., & Perona, P. (2014b). Influence of root characteristics and soil variables on the uprooting mechanics of Avena sativa and Medicago sativa seedlings. *Earth Surface Processes and Landforms*, *39*(10), 1354–1364.

Edwards, P., Kollmann, J, Gurnell, A., Petts, G., Tockner, K, & Ward, J. (1999). A conceptual model of vegetation dynamics on gravel bars of a large Alpine river. *Wetlands Ecology and Management*, *7*(3), 141–153.

Einstein, H. A. (1950). The bed-load function for sediment transportation in open channel flows. *Technical Report*, *No. 1026*, United States Department of Agriculture, Soil Conservation Service: Washington, DC.

Elliott, J. G. & Anders, S. P. (2004). *Summary of sediment data from the Yampa River and Upper Green River basins, Colorado and Utah, 1993-2002*. US Department of the Interior, US Geological Survey.

Enescu, C., Durrant, T. H., de Rigo, D, & Caudullo, G. (2016). *Salix caprea* in Europe: distribution, habitat, usage and threats. In *European atlas of forest tree species*. Luxembourg (L): Publications Office of the European Union.

Ennos, A. R. (1989). The mechanics of anchorage in seedlings of sunflower, *Helianthus annuus L. New Phytologist*, *113*(2), 185–192.

Ennos, A. R. (1990). The anchorage of leek seedlings: the effect of root length and soil strength. *Annals of Botany*, *65*(4), 409–416.

Ennos, A. (1993). The scaling of root anchorage. *Journal of Theoretical Biology*, *161*(1), 61–75.

Ennos, A. & Pellerin, S. (2000). Plant anchorage. In *Root Methods* (Chap. 16, pp. 545–565). Springer.

Fakih, M., Delenne, J. Y., Radjai, F., & Fourcaud, T. (2017). Modeling root growth in granular soils: effects of root stiffness and packing fraction. In *EPJ Web of Conferences* (Vol. 140, p. 14013). EDP Sciences.

Fan, C.-C. & Chen, Y.-W. (2010). The effect of root architecture on the shearing resistance of root-permeated soils. *Ecological Engineering*, *36*(6), 813–826.

Fathi-Maghadam, M & Kouwen, N. (1997). Nonrigid, nonsubmerged, vegetative roughness on floodplains. *Journal of Hydraulic Engineering*, *123*(1), 51–57.

Fitter, A. (1987). An architectural approach to the comparative ecology of plant root systems. *New phytologist*, *106*, 61–77.

FLO Engineering, I. (1994). *Little Snake River channel monitoring project* (tech. rep. No. 1994 fall channel monitoring trip). US Fish, Wildlife Service, National Park Service, and Colorado State University.

Follett, E. M. & Nepf, H. M. (2012). Sediment patterns near a model patch of reedy emergent vegetation. *Geomorphology*, *179*, 141–151.

Fredlund, D., Morgenstern, N. R., & Widger, R. (1978). The shear strength of unsaturated soils. *Canadian geotechnical journal*, *15*(3), 313–321.

Freeman, G. E., Rahmeyer, W. H., & Copeland, R. R. (2000). *Determination of resistance due to shrubs and woody vegetation* (tech. rep. No. ERDC/CHL TR-00-25). U.S. Army Engineer Research and Development Center, Viscksburb, MS (USA).

Galema, A. (2009). *Vegetation resistance; evaluation of vegetation resistance descriptors for flood management* (masters' thesis, University of Twente, Twente (NL)).

Ghisalberti, M. & Nepf, H. (2006). The structure of the shear layer in flows over rigid and flexible canopies. *Environmental Fluid Mechanics*, *6*(3), 277–301.

Ghisalberti, M. & Nepf, H. M. (2002). Mixing layers and coherent structures in vegetated aquatic flows. *Journal of Geophysical Research: Oceans*, *107*(C2).

Giadrossich, F, Schwarz, M, Cohen, D, Preti, F, & Or, D. (2013). Mechanical interactions between neighbouring roots during pullout tests. *Plant and soil*, *367*(1-2), 391–406.

Gibling, M. R. & Davies, N. S. (2012). Palaeozoic landscapes shaped by plant evolution. *Nature Geoscience*, *5*(2), 99.

Gilvear, D., Cecil, J, & Parsons, H. (2000). Channel change and vegetation diversity on a low-angle alluvial fan, River Feshie, Scotland. *Aquatic Conservation: Marine and Freshwater Ecosystems*, *10*(1), 53–71.

Gray, D. H. & Sotir, R. B. (1996). *Biotechnical and soil bioengineering slope stabilization: a practical guide for erosion control*. New York, NY (USA): John Wiley & Sons.

Gregory, P. J. (2008). *Plant roots: growth, activity and interactions with the soil*. New York, NY (USA): John Wiley & Sons.

Grime, J. P. (2006). *Plant strategies, vegetation processes, and ecosystem properties*. New York, NY (USA): John Wiley & Sons.

Gurnell, A. (2014). Plants as river system engineers. *Earth Surface Processes and Landforms*, *39*(1), 4–25.

Gurnell, A. & Petts, G. (2006). Trees as riparian engineers: the Tagliamento River, Italy. *Earth Surface Processes and Landforms*, *31*(12), 1558–1574.

Gyssels, G., Poesen, J., Bochet, E, & Li, Y. (2005). Impact of plant roots on the resistance of soils to erosion by water: a review. *Progress in physical geography*, *29*(2), 189–217.

Habersack, H. M. (2000). The river-scaling concept (RSC): a basis for ecological assessments. In *Assessing the Ecological Integrity of Running Waters* (pp. 49–60). Springer.

Heins, A., Simon, A., Farrugia, L., & Findeisen, M. (2004). *Bed-material characteristics of the San Juan River and selected tributaries, New Mexico: developing protools for stream-bottom deposits* (tech. rep. No. No. 47). USDA-ARS.

Hoag, J. C. (2005). Simple identification key to common willows, cottonwoods, alder, birch and dogwood of the Intermountain West. *Aberdeen (ID): USDA Natural Resources Conservation Service, Aberdeen Plant Materials Center. Riparian/Wetland Project Information Series*, *19*, 16.

Holnbeck, S. R. (2005). *Sediment-transport investigations of the Upper Yellowstone River, Montana, 1999 through 2001: data collection, analysis, and simulation of sediment transport*. US Department of the Interior, US Geological Survey.

Hongwu, T, Wang, H, Liang, D., Lv, S., & Yan, L. (2013). Incipient motion of sediment in the presence of emergent rigid vegetation. *Journal of Hydro-environment Research*, *7*(3), 202–208.

Hortobágyi, B., Corenblit, D., Steiger, J., & Peiry, J.-L. (2018). Niche construction within riparian corridors. Part I: Exploring biogeomorphic feedback windows of three pioneer riparian species (Allier River, France). *Geomorphology*, *305*, 94–111.

Hu, Y., Huai, W., & Han, J. (2013). Analytical solution for vertical profile of streamwise velocity in open-channel flow with submerged vegetation. *Environmental fluid mechanics*, *13*(4), 389–402.

Hupp, C. R. & Osterkamp, W. (1996). Riparian vegetation and fluvial geomorphic processes. *Geomorphology*, *14*(4), 277–295.

Huthoff, F., Augustijn, D., & Hulscher, S. J. (2007). Analytical solution of the depth-averaged flow velocity in case of submerged rigid cylindrical vegetation. *Water resources research*, *43*(6).

Hygelund, B. & Manga, M. (2003). Field measurements of drag coefficients for model large woody debris. *Geomorphology*, *51*(1-3), 175–185.

Ishikawa, Y., Sakamoto, T., & Mizuhara, K. (2003). Effect of density of riparian vegetation on effective tractive force. *Journal of Forest Research*, *8*(4), 235–246.

Järvelä, J. (2004). Determination of flow resistance caused by non-submerged woody vegetation. *International Journal of River Basin Management*, *2*(1), 61–70.

Johnson, W. C. (1997). Equilibrium response of riparian vegetation to flow regulation in the Platte River, Nebraska. *Regulated Rivers: Research & Management: An International Journal Devoted to River Research and Management*, *13*(5), 403–415.

Jordanova, A. A. & James, C. (2003). Experimental study of bed load transport through emergent vegetation. *Journal of Hydraulic Engineering*, *129*(6), 474–478.

Jud, D. (2009). *Eigendynamische Flussaufweitungen der Kander im Gebiet Heustrich Süd* (masters' thesis, EPFL, Losanne (CH)).

Karrenberg, S, Edwards, P., & Kollmann, J. (2002). The life history of Salicaceae living in the active zone of floodplains. *Freshwater Biology*, *47*(4), 733–748.

Karrenberg, S, Blaser, S, Kollmann, J, Speck, T, & Edwards, P. (2003). Root anchorage of saplings and cuttings of woody pioneer species in a riparian environment. *Functional ecology*, *17*(2), 170–177.

Kim, S. N., Toda, Y., & Tsujimoto, T. (2014). Effects of a Low-Head Dam Removal on River Morphology and Riparian Vegetation: A Case Study of Gongreung River. *Journal of Water Resource and Protection*, *6*(18), 1682.

Klopstra, D, Barneveld, H., Van Noortwijk, J., & Van Velzen, E. (1996). Analytical model for hydraulic roughness of submerged vegetation. In *Proceedings of the congress-international association for hydraulic research* (pp. 775–780).

Kothyari, U. C., Hashimoto, H., & Hayashi, K. (2009). Effect of tall vegetation on sediment transport by channel flows. *Journal of Hydraulic Research*, *47*(6), 700–710.

Kouwen, N. (1992). Modern approach to design of grassed channels. *Journal of irrigation and drainage engineering*, *118*(5), 733–743.

Kubrak, E., Kubrak, J., & Rowiński, P. M. (2008). Vertical velocity distributions through and above submerged, flexible vegetation. *Hydrological sciences journal*, *53*(4), 905–920.

Kui, L., Stella, J. C., Lightbody, A., & Wilcox, A. C. (2014). Ecogeomorphic feedbacks and flood loss of riparian tree seedlings in meandering channel experiments. *Water Resources Research*, *50*(12), 9366–9384.

Laio, F, Porporato, A, Ridolfi, L, & Rodriguez-Iturbe, I. (2001). Mean first passage times of processes driven by white shot noise. *Physical Review E*, *63*(3), 036105.

Lang, M, Ouarda, T., & Bobée, B. (1999). Towards operational guidelines for over-threshold modeling. *Journal of hydrology*, *225*(3-4), 103–117.

Leadbetter, M. R. (1991). On a basis for 'Peaks over Threshold' modeling. *Statistics & Probability Letters*, *12*(4), 357–362.

Leopold, L. B. & Wolman, M. G. (1957). *River channel patterns: braided, meandering, and straight*. US Government Printing Office.

Levins, R. (1969). Some demographic and genetic consequences of environmental heterogeneity for biological control. *American Entomologist*, *15*(3), 237–240.

Li, R. & Shen, H. W. (1973). Effect of tall vegetations on flow and sediment. *Journal of the hydraulics division*, *99*(5).

Little, E. L. & Viereck, L. A. (1971). *Atlas of United States trees*. Washington, DC: US Dept. of Agriculture, Forest Service.

Liu, Y., Gao, J., Lou, H., Zhang, J., & Cui, Q. (2011). The root anchorage ability of *Salix alba* var. tristis using a pull-out test. *African Journal of Biotechnology*, *10*(73), 16501–16507.

Luhar, M. & Nepf, H. M. (2011). Flow-induced reconfiguration of buoyant and flexible aquatic vegetation. *Limnology and Oceanography*, *56*(6), 2003–2017.

Mahoney, J. M. & Rood, S. B. (1998). Streamflow requirements for cottonwood seedling recruitment-an integrative model. *Wetlands*, *18*(4), 634–645.

Manners, R. B., Wilcox, A. C., Kui, L., Lightbody, A. F., Stella, J. C., & Sklar, L. S. (2015). When do plants modify fluvial processes? Plant-hydraulic interactions under variable flow and sediment supply rates. *Journal of Geophysical Research: Earth Surface*, *120*(2), 325–345.

Marani, M., D'Alpaos, A., Lanzoni, S., Carniello, L., & Rinaldo, A. (2010). The importance of being coupled: Stable states and catastrophic shifts in tidal biomorphodynamics. *Journal of Geophysical Research: Earth Surface*, *115*(F4).

Marani, M., Da Lio, C., & D'Alpaos, A. (2013). Vegetation engineers marsh morphology through multiple competing stable states. *Proceedings of the National Academy of Sciences*, *110*(9), 3259–3263.

Melville, B. & Sutherland, A. (1988). Design method for local scour at bridge piers. *Journal of Hydraulic Engineering*, *114*(10), 1210–1226.

Meyer-Peter, E. & Müller, R. (1948). Formulas for bed-load transport. In *IAHSR 2nd meeting, Stockholm, appendix 2* (pp. 39–64). IAHR.

Michael, L. (2015). *Statistical turbulence modelling for fluid dynamics-demystified: an introductory text for graduate engineering students*. World Scientific.

Mickovski, S., van Beek, L. P., & Salin, F. (2005). Uprooting of vetiver uprooting resistance of vetiver grass (*Vetiveria zizanioides*). *Plant and Soil*, *278*(1), 33–41.

Mickovski, S., Bengough, A., Bransby, M., Davies, M., Hallett, P., & Sonnenberg, R. (2007). Material stiffness, branching pattern and soil matric potential affect the pullout resistance of model root systems. *European Journal of Soil Science*, *58*(6), 1471–1481.

Mickovski, S. B. & Ennos, R. A. (2002). A morphological and mechanical study of the root systems of suppressed crown Scots pine *Pinus sylvestris*. *Trees*, *16*(4-5), 274–280.

Mickovski, S. B., Hallett, P. D., Bransby, M. F., Davies, M. C., Sonnenberg, R., & Bengough, A. G. (2009). Mechanical reinforcement of soil by willow roots: impacts of root properties and root failure mechanism. *Soil Science Society of America Journal*, *73*(4), 1276–1285.

Mitsch, W. J. & Gosselink, J. G. (2000). Wetlands. *Inc., New York, New York*.

Montgomery, D. R. (1997). River management: What's best on the banks? *Nature*, *388*(6640), 328.

Morgan, R. P. & Rickson, R. J. (2003). *Slope stabilization and erosion control: a bioengineering approach*. Taylor & Francis.

Mueller, E. R. & Pitlick, J. (2013). Sediment supply and channel morphology in mountain river systems: 1. Relative importance of lithology, topography, and climate. *Journal of Geophysical Research: Earth Surface*, *118*(4), 2325–2342.

Mueller, E. R., Pitlick, J., & Nelson, J. M. (2005). Variation in the reference Shields stress for bed load transport in gravel-bed streams and rivers. *Water Resources Research*, *41*(4).

Murray, A. B. & Paola, C. (2003). Modelling the effect of vegetation on channel pattern in bedload rivers. *Earth Surface Processes and Landforms*, *28*(2), 131–143.

Naiman, R. J., Decamps, H., & McClain, M. E. (2010). *Riparia: ecology, conservation, and management of streamside communities*. Elsevier.

National River Flow Archive. (2017). https://nrfa.ceh.ac.uk/. Wallingford (UK): Centre for ecology & hydrology.

Nepf, H. & Ghisalberti, M. (2008). Flow and transport in channels with submerged vegetation. *Acta Geophysica*, *56*(3), 753–777.

Nepf, H. M. (2012a). Flow and transport in regions with aquatic vegetation. *Annual review of fluid mechanics*, *44*, 123–142.

Nepf, H. M. (2012b). Hydrodynamics of vegetated channels. *Journal of Hydraulic Research*, *50*(3), 262–279.

Nepf, H. & Vivoni, E. (2000). Flow structure in depth-limited, vegetated flow. *Journal of Geophysical Research: Oceans*, *105*(C12), 28547–28557.

Nezu, I. & Sanjou, M. (2008). Turbulence structure and coherent motion in vegetated canopy open-channel flows. *Journal of hydro-environment research*, *2*(2), 62–90.

Nicholas, A. P. (2013). Modelling the continuum of river channel patterns. *Earth Surface Processes and Landforms*, *38*(10), 1187–1196.

Novak, S. Y. (2011). *Extreme value methods with applications to finance*. CRC Press.

Novak, S. J. (2006). *Hydraulic modelling analysis of the middle Rio Grande River from Cochiti Dam to Galisteo Creek, New Mexico* (masters' thesis, Colorado State University, Fort Collins, CO (USA)).

Okabe, T, Yuuki, T, & Kojima, M. (1997). Bed-load rate on movable beds covered by vegetation. In *Environmental and Coastal Hydraulics: Protecting the Aquatic Habitat* (pp. 1396–1401). ASCE.

Okamoto, T.-A. & Nezu, I. (2009). Turbulence structure and "Monami" phenomena in flexible vegetated open-channel flows. *Journal of Hydraulic Research*, *47*(6), 798–810.

Parker, G. (1990). Surface-based bedload transport relation for gravel rivers. *Journal of hydraulic research*, *28*(4), 417–436.

Parker, G., Wilcock, P. R., Paola, C., Dietrich, W. E., & Pitlick, J. (2007). Physical basis for quasi-universal relations describing bankfull hydraulic geometry of single-thread gravel bed rivers. *Journal of Geophysical Research: Earth Surface*, *112*(F4).

Pasquale, N, Perona, P., Schneider, P, Shrestha, J, Wombacher, A., & Burlando, P. (2011). Modern comprehensive approach to monitor the morphodynamic evolution of a restored river corridor. *Hydrology and Earth System Sciences*, *15*(4), 1197–1212.

Pasquale, N, Perona, P, Francis, R, & Burlando, P. (2012). Effects of streamflow variability on the vertical root density distribution of willow cutting experiments. *Ecological Engineering*, *40*, 167–172.

Pasquale, N, Perona, P, Francis, R, & Burlando, P. (2014). Above-ground and below-ground Salix dynamics in response to river processes. *Hydrological processes*, *28*(20), 5189–5203.

Pazzaglia, F. J., Gardner, T. W., & Merritts, D. J. (1998). Bedrock fluvial incision and longitudinal profile development over geologic time scales determined by fluvial terraces. In K. J. Tinkler & E. E. Wohl (Eds.), *Rivers Over Rock: Fluvial Processes in Bedrock Channels* (Vol. 107, pp. 207–235). American Geophysical Union.

Perona, P & Crouzy, B. (2018). Resilience of riverbed vegetation to uprooting by flow. *Proc. R. Soc. A*, *474*(2211).

Perona, P, Porporato, A, & Ridolfi, L. (2007). A stochastic process for the interannual snow storage and melting dynamics. *Journal of Geophysical Research: Atmospheres*, *112*(D8).

Perona, P., Molnar, P, Crouzy, B, Perucca, E., Jiang, Z, McLelland, S, ... Camporeale, C et al. (2012a). Biomass selection by floods and related timescales: Part 1. Experimental observations. *Advances in Water Resources*, *39*, 85–96.

Perona, P., Daly, E., Crouzy, B., & Porporato, A. (2012b). Stochastic dynamics of snow avalanche occurrence by superposition of Poisson processes. *Proc. R. Soc. A*, rspa20120396.

Perona, P., Crouzy, B., McLelland, S., Molnar, P., & Camporeale, C. (2014). Ecomorphodynamics of rivers with converging boundaries. *Earth Surface Processes and Landforms*, *39*(12), 1651–1662.

Perry, C. H., Miller, R. C., & Brooks, K. N. (2001). Impacts of short-rotation hybrid poplar plantations on regional water yield. *Forest Ecology and Management*, *143*(1-3), 143–151.

Perucca, E., Camporeale, C., & Ridolfi, L. (2007). Significance of the riparian vegetation dynamics on meandering river morphodynamics. *Water Resources Research*, *43*(3).

Petryk, S. & Bosmajian III, G. (1975). Analysis of flow through vegetation. *Journal of the Hydraulics Division*, *101*(ASCE# 114517 Proceeding).

Piedra, M. M. (2010). *Flume investigation of the effects of sub-threshold rising flows on the entrainment of gravel beds* (Doctoral dissertation, University of Glasgow, Glasgow (UK)).

Pollen, N. (2007). Temporal and spatial variability in root reinforcement of streambanks: accounting for soil shear strength and moisture. *Catena*, *69*(3), 197–205.

Pollen, N. & Simon, A. (2005). Estimating the mechanical effects of riparian vegetation on stream bank stability using a fiber bundle model. *Water Resources Research*, *41*(7).

Pope, S. B. (2001). *Turbulent flows*. IOP Publishing.

Potyondy, J. G. (1961). Skin friction between various soils and construction materials. *Geotechnique*, *11*(4), 339–353.

Prudnikov, A., Brychkov, Y. A., & Marichev, O. (1986). *Integrals and series: special functions*. New York, NY (USA): Gordon and Breach Science.

Reubens, B., Poesen, J., Danjon, F., Geudens, G., & Muys, B. (2007). The role of fine and coarse roots in shallow slope stability and soil erosion control with a focus on root system architecture: a review. *Trees*, *21*(4), 385–402.

Ridolfi, L., D'Odorico, P., & Laio, F. (2011). *Noise-induced phenomena in the environmental sciences*. Cambridge University Press.

Rivaes, R., Rodríguez-González, P. M., Albuquerque, A., Pinheiro, A. N., Egger, G., & Ferreira, M. T. (2013). Riparian vegetation responses to altered flow regimes driven by climate change in Mediterranean rivers. *Ecohydrology*, *6*(3), 413–424.

Rodriguez-Iturbe, I., Porporato, A, Ridolfi, L, Isham, V, & Coxi, D. (1999). Probabilistic modelling of water balance at a point: the role of climate, soil and vegetation. In *Proceedings of the Royal Society of London A: Mathematical, Physical and Engineering Sciences* (Vol. 455, *1990*, pp. 3789–3805). The Royal Society.

Rominger, J. T., Lightbody, A. F., & Nepf, H. M. (2010). Effects of added vegetation on sand bar stability and stream hydrodynamics. *Journal of Hydraulic Engineering*, *136*(12), 994–1002.

Sand-Jensen, K. (2008). Drag forces on common plant species in temperate streams: consequences of morphology, velocity and biomass. *Hydrobiologia*, *610*(1), 307–319.

Savenije, H. H. (2003). The width of a bankfull channel; Lacey's formula explained. *Journal of Hydrology*, *276*(1-4), 176–183.

Schaetzl, R. J., Johnson, D. L., Burns, S. F., & Small, T. W. (1989). Tree uprooting: review of terminology, process, and environmental implications. *Canadian Journal of Forest Research*, *19*(1), 1–11.

Schlichting, H. (1937). Experimental investigation of the problem of surface roughness.

Schnauder, I. & Moggridge, H. L. (2009). Vegetation and hydraulic - morphological interactions at the individual plant, patch and channel scale. *Aquatic Sciences*, *71*(3), 318.

Schwarz, M, Lehmann, P., & Or, D. (2010a). Quantifying lateral root reinforcement in steep slopes - from a bundle of roots to tree stands. *Earth Surface Processes and Landforms: The Journal of the British Geomorphological Research Group*, *35*(3), 354–367.

Schwarz, M, Preti, F, Giadrossich, F, Lehmann, P., & Or, D. (2010b). Quantifying the role of vegetation in slope stability: a case study in Tuscany (Italy). *Ecological Engineering*, *36*(3), 285–291.

Schwarz, M, Cohen, D, & Or, D. (2010c). Root-soil mechanical interactions during pullout and failure of root bundles. *Journal of Geophysical Research: Earth Surface*, *115*(F4).

Schwarz, M, Cohen, D, & Or, D. (2011). Pullout tests of root analogs and natural root bundles in soil: Experiments and modeling. *Journal of Geophysical Research: Earth Surface*, *116*(F2).

Serlet, A. J., Gurnell, A. M., Zolezzi, G., Wharton, G., Belleudy, P., & Jourdain, C. (2018). Biomorphodynamics of alternate bars in a channelized, regulated river: an integrated historical and modelling analysis. *Earth Surface Processes and Landforms*.

Shafroth, P. B., Friedman, J. M., Auble, G. T., Scott, M. L., & Braatne, J. H. (2002). Potential responses of riparian vegetation to dam removal: dam removal generally causes changes to aspects of the physical environment that influence the establishment and growth of riparian vegetation. *BioScience*, *52*(8), 703–712.

Sharma, M. & Parton, J. (2007). Height–diameter equations for boreal tree species in Ontario using a mixed-effects modeling approach. *Forest Ecology and Management*, *249*(3), 187–198.

Sharpe, R. & James, C. (2006). Deposition of sediment from suspension in emergent vegetation. *Water Sa*, *32*(2), 211–218.

Sher, A. A., Marshall, D. L., & Taylor, J. P. (2002). Establishment patterns of native Populus and Salix in the presence of invasive nonnative Tamarix. *Ecological applications*, *12*(3), 760–772.

Shimizu, Y. (1994). Numerical analysis of turbulent open-channel flow over a vegetation layer using a $\kappa - \varepsilon$ turbulence model. *Journal of Hydroscience and Hydraulic Engineering, JSCE*, *11*(2), 57–67.

Smith, H. Y. (1999). *Assessing longevity of ponderosa pine (Pinus ponderosa) snags in relation to age, diameter, wood density and pitch content* (masters' thesis, University of Montana, Missoula, MT (USA)).

Solari, L, Van Oorschot, M, Belletti, B, Hendriks, D, Rinaldi, M, & Vargas-Luna, A. (2016). Advances on modelling riparian vegetation-Hydromorphology interactions. *River Research and Applications*, *32*(2), 164–178.

Solari, S & Losada, M. (2012). A unified statistical model for hydrological variables including the selection of threshold for the peak over threshold method. *Water Resources Research*, *48*(10).

Specht, F.-J. (2002). *Einflußvon Gerinnebreite und Uferbewuchs auf die hy- draulisch-sedimentologischen Verhältnisse naturnaher Fließgewässer* (Doctoral dissertation, Technische Universität Braunschweig, Braunschweig (DE)).

Stewart, H. (2009). *Cedar: tree of life to the Northwest Coast Indians*. D & M Publishers.

Stoesser, T, Kim, S., & Diplas, P. (2010). Turbulent flow through idealized emergent vegetation. *Journal of Hydraulic Engineering*, *136*(12), 1003–1017.

Stokes, A, Ball, J, Fitter, A., Brain, P, & Coutts, M. (1996). An experimental investigation of the resistance of model root systems to uprooting. *Annals of Botany*, *78*(4), 415–421.

Stone, B. M. & Shen, H. T. (2002). Hydraulic resistance of flow in channels with cylindrical roughness. *Journal of hydraulic engineering*, *128*(5), 500–506.

Stone, M. C., Chen, L., Kyle McKay, S, Goreham, J., Acharya, K., Fischenich, C., & Stone, A. B. (2013). Bending of submerged woody riparian vegetation as a function of hydraulic flow conditions. *River Research and Applications*, *29*(2), 195–205.

Stromberg, J. C., Lite, S. J., Marler, R., Paradzick, C., Shafroth, P. B., Shorrock, D., ... White, M. S. (2007). Altered stream-flow regimes and invasive plant species: the Tamarix case. *Global Ecology and Biogeography*, *16*(3), 381–393.

Stromberg, J. C., Lite, S. J., & Dixon, M. (2010). Effects of stream flow patterns on riparian vegetation of a semiarid river: implications for a changing climate. *River Research and Applications*, *26*(6), 712–729.

Tal, M. & Paola, C. (2010). Effects of vegetation on channel morphodynamics: results and insights from laboratory experiments. *Earth Surface Processes and Landforms*, *35*(9), 1014–1028.

Tanaka, N. & Yagisawa, J. (2009). Effects of tree characteristics and substrate condition on critical breaking moment of trees due to heavy flooding. *Landscape and Ecological Engineering*, *5*(1), 59–70.

Thorne, C. (1990). Effects of vegetation on riverbank erosion and stability. *Vegetation and erosion*.

Todorovic, P. (1978). Stochastic models of floods. *Water Resources Research*, *14*(2), 345–356.

Todorovic, P. (1970). On some problems involving random number of random variables. *The Annals of Mathematical Statistics*, *41*(3), 1059–1063.

Tron, S., Perona, P., Gorla, L., Schwarz, M., Laio, F., & Ridolfi, L. (2015). The signature of randomness in riparian plant root distributions. *Geophysical Research Letters*, *42*(17), 7098–7106.

Tsujimoto, T. (1999). Fluvial processes in streams with vegetation. *Journal of hydraulic research*, *37*(6), 789–803.

Ulanova, N. G. (2000). The effects of windthrow on forests at different spatial scales: a review. *Forest ecology and management*, *135*(1-3), 155–167.

van Oorschot, M., Kleinhans, M., Geerling, G., & Middelkoop, H. (2016). Distinct patterns of interaction between vegetation and morphodynamics. *Earth Surface Processes and Landforms*, *41*(6), 791–808.

van Rijn, L. C. (1984). Sediment transport, part II: suspended load transport. *Journal of hydraulic engineering*, *110*(11), 1613–1641.

Vargas Luna, A. (2016). *Role of vegetation on river bank accretion* (Doctoral dissertation, Delft University of Technology, Delft (NL)).

Vargas-Luna, A., Crosato, A., & Uijttewaal, W. S. (2015). Effects of vegetation on flow and sediment transport: comparative analyses and validation of predicting models. *Earth Surface Processes and Landforms*, *40*(2), 157–176.

Vargas-Luna, A., Crosato, A., Calvani, G., & Uijttewaal, W. S. (2016). Representing plants as rigid cylinders in experiments and models. *Advances in Water Resources*, *93*, 205–222.

Västilä, K. & Järvelä, J. (2014). Modeling the flow resistance of woody vegetation using physically based properties of the foliage and stem. *Water Resources Research*, *50*(1), 229–245.

Västilä, K., Järvelä, J., & Aberle, J. (2013). Characteristic reference areas for estimating flow resistance of natural foliated vegetation. *Journal of hydrology*, *492*, 49–60.

Vetsch, D, Siviglia, A, Ehrbar, D, Facchini, M, Gerber, M, Kammerer, S, ... Volz, C et al. (2016). System manuals of BASEMENT. *Laboratory of Hydraulics, Glaciology and Hydrology (VAW), ETH Zurich*.

Vogel, S. (1996). *Life in moving fluids: the physical biology of flow*. Princeton University Press.

Ward, J., Tockner, K, Arscott, D., & Claret, C. (2002). Riverine landscape diversity. *Freshwater Biology*, *47*(4), 517–539.

Warner, R. & Hendrix, K. (1984). *California riparian systems: ecology, conservation, and productive management*. Berkeley, CA (USA): University of California Press.

Watanabe, K, Nagy, H., & Noguchi, H. (2002). Flow structure and bed-load transport in vegetation flow. In *Advances in Hydraulics and Water Engineering: Volumes I & II* (pp. 214–218). World Scientific.

Water Data for the Nation. (2017). https://waterdata.usgs.gov/nwis. Reston, VA (USA): US Geological Survey.

Wilcock, P. R. & Southard, J. B. (1988). Experimental study of incipient motion in mixed-size sediment. *Water Resources Research*, *24*(7), 1137–1151.

Wilkerson, G. V. & Parker, G. (2010). Physical basis for quasi-universal relationships describing bankfull hydraulic geometry of sand-bed rivers. *Journal of Hydraulic Engineering*, *137*(7), 739–753.

Wohl, E., Lane, S. N., & Wilcox, A. C. (2015). The science and practice of river restoration. *Water Resources Research*, *51*(8), 5974–5997.

Wong, M. & Parker, G. (2006). Reanalysis and correction of bed-load relation of Meyer-Peter and Müller using their own database. *Journal of Hydraulic Engineering*, *132*(11), 1159–1168.

Wu, T. H., McOmber, R. M., Erb, R. T., & Beal, P. E. (1988). Study of soil-root interaction. *Journal of Geotechnical Engineering*, *114*(12), 1351–1375.

Wu, W & He, Z. (2009). Effects of vegetation on flow conveyance and sediment transport capacity. *International Journal of Sediment Research*, *24*(3), 247–259.

Yager, E. & Schmeeckle, M. (2013). The influence of vegetation on turbulence and bed load transport. *Journal of Geophysical Research: Earth Surface*, *118*(3), 1585–1601.

Yang, W. & Choi, S.-U. (2010). A two-layer approach for depth-limited open-channel flows with submerged vegetation. *Journal of Hydraulic Research*, *48*(4), 466–475.

Ye, Q. (2012). *An approach towards generic coastal geomorphological modelling with applications* (Doctoral dissertation).

Yen, C. (1987). Tree root patterns and erosion control. In *International workshop on soil erosion and its countermeasures. Soil and Water Conservation Society of Thailand, Bangkok* (pp. 92–111).

Yoshioka, H., Shimizu, E., Fukuoka, N., Fujiwara, T., & Sato, F. (1998). Evaluation of rooting ability in cabbage plug seedlings by drag resistance (resistance to uprooting). *Journal of the Japanese Society for Horticultural Science*, *67*(4), 589–594.

Zelenhasic, E. F. (1970). Theoretical probability distributions for flood peaks. *Hydrology papers (Colorado State University); no. 42*.

Zen, S., Zolezzi, G., Toffolon, M., & Gurnell, A. M. (2016). Biomorphodynamic modelling of inner bank advance in migrating meander bends. *Advances in water resources*, *93*, 166–181.

Zen, S., Mueller, E., Hadden, R., & Perona, P. (2018). Effects of stochasticity on rate of spread and fire front evolution statistics. (Abstract [EP31B-02] at *2018 Fall Meeting, AGU, Washington, D.C., 10-14 Dec.*).

Zong, L. & Nepf, H. (2010). Flow and deposition in and around a finite patch of vegetation. *Geomorphology*, *116*(3), 363–372.

Zong, L. & Nepf, H. (2012). Vortex development behind a finite porous obstruction in a channel. *Journal of Fluid Mechanics*, *691*, 368–391.

Acknowledgements

The present PhD research has been conducted thanks to a PhD scholarship given by the University of Florence (Italy) which is greatly acknowledged.

I would like to express my deep gratitude to Prof. Dr. Eng. Luca Solari for allowing me to carry out the PhD research at the Department of Civil and Environmental Engineering (DICEA) of the University Florence, Italy, and for the guidance and support during the whole Doctoral program.

I thank Prof. Dr. rer. nat. Hans Matthias Schöniger for accepting me as a PhD student at the Leichtweiß-Institute for Hydraulic Engineering and Water Resources (LWI) of the Technical University of Braunschweig, Germany.

I am truly grateful to Prof. Dr. Eng. Paolo Perona, for accepting me as a visiting PhD student at the Institute for Infrastructure and Environment (IIE) at The University of Edinburgh, United Kingdom, and for his valuable suggestions, comments and teachings. The support of the University of Edinburgh during the visiting periods is deeply acknowledged.

Dr. Eng. Simona Francalanci is acknowledged for her comments and exchanges about my research activity. A big thanks to all the trainees for their help during experiments and field measurements.

A special thank to my friends and colleagues. A particular mention goes to Dr. Eng. Costanza Carbonari, for her passion in our research field and the time and experiences shared throughout the PhD program, and to Eng. Valentina Bau' for her friendship and support during my stays in Edinburgh.